The ACUS Project: development of propulsion technologies for RPAS weaponry

Abstract

RPAS (Remotely Piloted Aircraft Systems) are, nowadays, a key asset for military and civil operations. Recent military conflicts, particularly in Ukraine, have highlighted the importance of such technologies on the battlefield. These platforms have been extensively used as loitering munitions, or for air strikes, employing micro-missiles and non-conventional weaponry.

Nowadays, the Spanish Air Force does not operate RPAS with strike capabilities, as they are limited to surveillance and reconnaissance purposes. It has been considered fundamental to start a series of developments that enhance and expand these capabilities, by designing and testing technologies that can be adapted to the existing platforms. This Master Thesis addresses this engineering challenge with the design, development, and testing of the propulsion plant of a micro-missile: the ”ACUS Project”, which is expected to operate in small platforms for counter-RPAS or traditional strike operations. This new technological proposal is based on a dual stage propulsion system which uses, firstly, a pressurized stage and, secondly, a solid propulsion motor, and is being developed at the Optoelectronics and Rocketry Department of the Spanish National Institute of Aerospace Technology (INTA).

This manuscript tackles a preliminary design from a propulsion point of view. After a review of the state of the art, and a thorough analysis of the underlying theory, a design for both stages is proposed, designed, and tested. After the experimental campaign, it has been demonstrated that, upon further design stages and qualification milestones, the proposed technology can be successfully employed for the deployment of weaponry onboard RPAS platforms.

Key words: RPAS, propulsion, projectile, rocket.

This page intentionally left blank

Contents

This page intentionally left blank

List of Figures

This page intentionally left blank

List of Tables

This page intentionally left blank

Nomenclature

AM Additive Manufacturing

AP Ammonium Perchlorate

DB Double base propellants

HALE High Altitude Long Endurance

HALE Medium Altitude Long Endurance

ICAO International Civil Aviation Organization

INTA *Instituto Nacional de Técnica Aeroespacial* (National Institute of Aerospace Technology)

JDAM Joint Direct Attack Munition

LEO Lethality Enhanced Ordnance

NATO North Atlantic Treaty Organization

NME Norma Militar Española

NSAA National Safety Approving Authority

OSCE Organization for Security and Co-operation in Europe

RPAS Remotely Piloted Aircraft Systems

SLAM Surgical Loitering Airbone Munition

SRM Solid Rocket Motor

STANAG Standardization Agreement

UAS Unmanned Aircraft System

UAV Unmanned Aerial Vehicle

UC3M Universidad Carlos III de Madrid

UCAS Unmanned Combat Aerial System

UCAV Unmanned Combat Air Vehicle

USAF United States Air Force

1

Introduction & State of the Art

A general introduction to the Master Thesis is presented, together with the thesis objectives, after a review of the State of the Art and previous works on the topic. The regulatory framework is presented.

Contents

1.1 Introduction

UAVs stand for Unmanned Aerial Vehicles, commonly known as drones[i]. They are the main component of Unmanned Aircraft Systems (UAS), which includes the remote

[i] Which was the word used for male honeybees, coming from Old English *dran*.

pilot station, the command, control, and communication links [1]. This denomination highlights the existance of other elements apart from the vehicle, for a proper operation. Remotely Piloted Aircraft (RPAS) is typically considered as a subset of UAVs. In that case, the UAV is operated remotely from a ground control station. We will generally avoid the use of the term UAV or drone, which are considered legacy denominations. The term RPAS was officially introduced in ICAO (International Civil Aviation Organization) in 2011, by Circular 328 [1].

RPAS are crucial, since decades ago, for military and civil[ii] purposes. By 2017, drone manufacturers sales in the US were close to 3800 million dollars, from which 96% corresponded to military contracts [2][3]. Departing from the first UAS used by the US Military in Vietnam, the AQM-34 Firebee, as of October 2008, almost 500,000 flight hours in support of Operations Enduring Freedom and Iraqi Freedom were flown by UAS [4]. On the other hand, they are also used for a wide variety of purposes, including agriculture, aerial photography, science, leisure, or multirobot systems [5]. UAV networks can be also designed for envisioned civil applications from a communications point of view [6]. Only in Europe, it was estimated that in 2017, there were between 1 and 1.5 million drones for civilian use [3].

Despite the fact that RPAS technologies are being increasingly used for civil purposes, recent military events (i.e., Ukraine-Russia War) have increased their importance from a military perspective. Combat RPAS are extensively used in today's modern battlefield, performing a variety of missions: from surveillance to loitering munition. Many of these systems typically require assisted deployment methods, which accelerate the RPAS until they have sufficient speed for self-sustained flight.

In the Ukraine-Russia conflict, the latter has extensively used Iranian drones with embedded warheads, as loitering munition, to target a variety of objectives. Moreover, the

[ii] Although the military industry has been the main driver of this development during the last century.

operational characteristics of such drones, which are employed in waves and groups[iii] of dozens of units, have compromised the aerial safety of Ukrainian cities, since current anti-aircraft defences are focused on aircraft and missile interception, a legacy concept in the new conflicts. Consequently, Ukraine is spending hundreds of thousands of dollars On missiles to shoot down drones with an approximate cost of tens of thousands of dollars. This is not acceptable, from a cost and tactic point of view, as Ukraine's anti-aircraft measures stockpile may be spent in an effortless battle against those drones, while Russia is reserving more expensive and effective weapons to attack, once Ukraine's aerial defence is exhausted. Therefore, it is fundamental to transition from anti-aircraft to counter-RPAS defence systems, to effectively tackle these threats. Such measures may be deployed from RPAS systems.

This issue, and the use of RPAS systems in today's battlefield, has attracted the attention of many NATO countries, which are actively researching, and investing important resources, in the field of RPAS. In the case of Spain, this effort is partially carried out by the National Institute of Aerospace Technology. The Spanish Army operates several RPAS systems, including advanced solutions such as the Predator, and is involved in the EuroDrone project. However, none of the platforms are currently designed to be deployed with weapons. Therefore, the Optoelectronics and Rocketry Department of the Institute has led, for years, projects that study technologies and advancements in the field of RPAS systems. In particular, the ACUS project is focused on the development of RPAS onboard weaponry, which may be used both for anti-drone activities and for 'traditional' battlefield operations. This project tackles the objective by developing a dual-stage platform. Specifically, this Master Thesis is focused on the design of a first pressurized stage, and the design of the chemical propulsion rocket of the second stage.

[iii] One may be tempted to use the word *swarm*, instead. However, *group* is a more general definition that comprises several isolated individuals, without the need of collaboration between them, while in a *swarm* all units are typically operated to perform a single task [7].

Consequently, this work is an engineering and research document that describes all the stages that were followed in order to design and test the propulsion module of a missile that can carry different types of payloads, and that can be easily implemented over existing platforms. From operational requirements, a preliminary design that solely focuses on the propulsion needs of the system is presented. Different subsystems are to be validated, including the electronics, igniter, and the propulsion modules.

Chapter 1 introduces RPAS, classification, and history. Based on the problems associated to its use on the battlefield, a State of the Art review is presented, together with a description of the thesis objectives, and the regulatory framework. Chapter 2 focuses on the design and manufacturing of the first stage. Chapter 3 starts with the development of a numerical performance model for solid rocket motors, validated with reputed codes and experimental literature data. It continues with a parametric analysis of the rocket performance using the developed model, and with the second stage design, a rocket motor, based on that analysis. Chapter 4 details the experimental campaign of both stages. Lastly, Chapter 5 finishes the thesis with the work conclusions, future works analysis, project budget, and socio-economic impact.

1.1.1 RPAS classification

The basic classification of RPAS is based on the system architecture. From a general perspective, they may be classified into four major types [8]:

- Fixed - Wing: greater endurance and speed. Complex operation.
- Fixed - Wing Hybrid: VTOL applications, and long endurance.
- Single Rotor: VTOL and Hover applications.
- Multirotor: For VTOL and Hover applications, but short endurance capabilities.

This classification applies indistinctly to military and civil platforms. However, military vehicles are also classified according to their operational characteristics and architecture (takeoff weight, speed, endurance, etc). This classification is briefly explored in the next section.

1.1.1.1 Military RPAS Classification

Military RPAS can be classified, typically, according to their operational characteristics (i.e., speed, flight altitude, and takeoff weight). Table 1.1 shows the current classification of UAS systems in the United States [2]. If a given system shares its characteristics between different groups, it was classified to the higher one.

Table 1.1: UAS Classification in the U.S, as a function of TO weight, operating altitude, and airspeed.

UAS category	Max Gross takeoff weight (lbs)	Operating altitude (ft)	airspeed (kts)
1	<20	<1200 (AGL)	<100
2	21-55	<3500 (AGL)	250
3	<1320	<18000 (MSL)	
4	>1320		Any
5		>18000 (MSL)	

This classification is in accordance with the DoD 2009-2034 Unmanned Systems Integrated Roadmap [2][4]. In Spain, the classification follows NATO guidelines, as is shown in Table 1.2 [9]. It classifies UAS depending on the takeoff weight, the use, or the operating range and altitude.

1.1.2 UAVs history at a glance

Although, from a general perspective, drones are part of human's daily live since, relatively, very little ago, the development of UAVs is deeply rooted with General Aviation Development, starting by the end of the XIX century. However, the first ideas

Table 1.2: NATO UAS classification as a function of TO weight, operating altitude, and mission radius.

Class	Category	Typical Use	Operating altitude (ft)	Normal mission radius
Class I (<150 kg)	Micro <2 kg.	Tactical PI, Individual	Up to 200 ft AGL	5 km
	Mini 2 - 20 kg.	Tactical Sub-unit (Manual Launch)	Up to 3 kft AGL	25 km
	Small >20 kg.	Tactical Unit (employs launch system)	Up to 5 kft AGL	50 km
Class II (150 kg. - 600 kg.)	Tactical	Tactical Formation	Up to 10000 ft AGL	200 km
Class III (>600 kg.)	Strike / Combat	Strategic / National	Up to 65000 ft MSL	Unlimited
	HALE	Strategic / National	Up to 65000 ft MSL	Unlimited
	MALE	Operational / Theathre	Up to 45000 ft MSL	Unlimited

about autonomous movement were already studied in the past. For example, the concept of autonomous vertical flight was explored by Leonardo da Vinci in 1483, Mikhail Lomonosov in 1754 [10], or Launoy and Bienvenu in 1784 [11][10].

Some years before the first manned airplane flight in 1903, UAVs (or at least precursors) were already used, employing balloons and surveillance kites. In 1849, Franz von Uchatius suggested the use of balloons loaded with bombs against Venice, with poor results [12]. However, it paved the way for a military use of 'autonomous' vehicles. It is with the start of manned flight when the development of UAVs is accelerated. Table 1.3 details and highlights some important milestones in the history of UAV development (adapted from [13] and [14]).

As the reader may notice, the development of UAV technology is closely related to military conflicts. These systems are now a fundamental asset in military scenario. For example, in the Ukraine-Russia war, which started in 2022, both parties are extensively using drone technology for a variety of purposes: targeting artillery objectives,

Table 1.3: Main highlights of UAV development

Year	Event
1783	The Montgolfier Brothers invent the hot-air balloon
1849	Austria uses balloon bombs against Venice
1898	Nikola Tesla shows a radio-controlled boat for the first time
1917	First UAV Torpedo, the Kettering Bug
1935	First Modern Drone developed by the UK
1944	Germany develops V1 and V2 guided missiles
1973	Israel develops UAVs for surveillance and scouting
1991	UAVs are extensively used during the Gulf War
1996	The Predator Drone is developed
2006	UAVs Permitted in US Civilian Airspace
2010	Extensive use of drones in various industries

recording enemy positions, or surveillance purposes. Other options such as kamikaze drones (i.e., loitering munitions), which are loaded with an explosive charge, are also being used.

1.1.3 Short review of military UAVs in Spain

Spain is actively involved in the design, operation, and development of many UAV alternatives. Although not at the same level as the United States or Israel, the Spanish Ministry of Defence (MoD) has integrated the use of UAVs in its daily operations and duties. The following list details some of the UAVs which are in operation (or being developed) in Spain.

- **EuroMALE**: schedule for 2028, it is a Medium Altitude Long Endurance UAV (26 m. span) designed by *Airbus*, *Dassault* and *Leonardo*. It aims to be the reference UCAV (i.e., Unmanned Combat Air Vehicle) in Europe.
- **Q-SLAM-40**: designed by *Arquimea*, it is a Surgical Loitering Airbone Munition System, an hybrid between an UAV and a guided munition device. This type

of *kamikaze* drones are being used in the Ukraine War[iv]. It is suitable for short-range missions, can be deployed in less than 5 minutes, and can be carried by two soldiers [15]. The main disadvantage of this system is the little endurance that it presents (approx. 12 minutes), and the complexity in the certification process. Moreover, it is intended for one use (i.e., a single-shot device) [15]. The launcher is 800 mm long, 250 mm wide and 400 mm high, with a weight of 14.5 kg [16]. The maximum height over ground that can be achieved is 600 meters, with a limit speed of 110 km/h [16].

- **Geodrone**: fixed-wing drone used for cartography purposes [17].
- **RAVEN RQ11B**: Spain has in operation 81 UAVs of this type. Used for surveillance and ground forces support [17]. It can be deployed by hand from ground.
- **Predator B**: manufactured by *General Atomics Aeronautical Systems, INC*, and also known as MQ-9A, it serves in the 23th Wing since 2019. Very flexible from an operational point of view, it features a maximum endurance of over 27 hours, being able to operate up to 50 kft. See Figure 1.2 (retrieved from [18]).
- **Searcher MK III**: multi-mission tactical RPAS, manufactured by *Israel Aerospace Industries*, has a service ceiling of 23000 ft, a maximum endurance of 20 hours, and maximum range of 350 km. See Figure 1.1 (retrieved from [19]).

However, none of these platforms, as explained in the introduction, are actually configured to operate weapons. The solution of this limitation is the main objective of this technical project.

[iv] First concepts on loitering munition were explored in the US with the AGM-136 Tacit Rainbow, or the Harpy, manufactured by *Israel Aerospace Industries*

Figure 1.1: Searcher MK III.

Figure 1.2: Predator B.

1.2 State of the Art of Onboard Weaponry

Weapons onboard RPAS systems are part of the vehicle payload. Nevertheless, the payload can include any other equipment that may be needed for the mission completion. There may be disposable or non-disposable payloads. Weapons clearly fall within the first category, while other equipments such as infrared sensors, navigation, communication and surveillance modules are non-disposable.

We focus our attention on onboard weaponry. It is highly dependent on the platform characteristics. Firstly, there are obvious limitations in terms of weight. In the case of the Predator, the maximum payload is typically close to 1800 kg (although it depends on the particular configuration). The interfaces with the vehicle are also very dependent on the platform, and the reaction torques and forces exerted by the weapon on the vehicle are also affected by the inertia and mass characteristics of the UAS.

Traditionally, weapons onboard UAS have been designed to target ground objectives. In the current context, and by the development of new and cheap UAS systems, more effective counter-UAS weapons are being already developed. The main complexity in these type of weapons is the guidance and architecture of the weapon itself. The target (the enemy UAS) is a flexible platform able to perform complex maneuvering,

of very small size, and reduced infrared and radar footprint. The designed counter-UAS solution needs to be adapted to these new requirements. On the other hand, the onboard weapon needs to be deployed rapidly, and the response time needs to be minimized.

1.2.1 Traditional Weaponry

It seems reasonable to think that the first uses of modern military UAS were directed to air-ground strikes. However, in the case of the US Military (leading-edge endeavour in the field of UAS), until the Afghanistan War of 2001, most of the missions were surveillance and intelligence-based. The reasons after this decision were the little maturity of the technology, and concerns due to the high cost of the program. The Firebee, for example, was intended to be used in Vietnam with early laser-guided bombs, early maverick missiles, early cluster bombs or TV guided weapons. However, it ended up using mostly leaflet bombs [20]. Figure 1.3 shows the Firebee BQM-34 series with the original weapons kit. After the end of the Vietnam War, defence fundings were severely reduced in US. However, the implementation of missiles and weapons on UAS continued as an important research and technical issue, which was definitely tackled with the development of more advanced vehicles, as the Predator. It is with the beginning of the 21th century when the strike capabilities of these vehicles gained importance. The Predator, for example, was outfitted in 2001 to extend its capabilities, carrying two Hellfire missiles [21][22]. The Hellfire is an anti-tank missile, firstly introduced in 1982, but developed in the 1970s, with an effective range of around 4 miles [22].

The payload capacity of UAS rapidly increased after the first successful strike missions: Predators were armed with AIM-92 Stingers (air-to-air), and were capable of air-to-air engagement against Iraqi fighters.

Figure 1.3: BQM-34 Firebee series with the ammunition kit. The white missile located at the center of the picture is an AGM-65 Maverick, successfully launched in tests in the early 1970s. Picture by Bud Wolford, retrieved from [20].

The second version of the Predator, the Reaper, extended its predecessor capabilities by carrying 700 kg of weapons in the inboard hardpoints, and 340 kg in the outboard positions [20]. AGM-114 Hellfire air to ground missiles, GBU-12 Paveway II laser-guided bombs, and GBU-38 Joint Direct Attack Munition (JDAM), or AIM-9 Sidewinder are available at this platform. See Figure 1.4 and Figure 1.5 for more details.

1.2.2 Surgical Weapons

The weapons described in the previous paragraphs are very efficient against building or underground facilities, in the context of counter-terrorism, or conventional operations. However, its use against individuals or precised and limited objectives may be inefficient. Hellfire, for example, presents a fragmentation radius of around 20 m [20].

Figure 1.4: This MQ-9 Reaper model carries two GBU-12 Paveway II laser guided bombs in the inboard stations, and 4 Hellfire missiles in the outboard stations, while taxiing in an Afghanistan Runway. U.S. Air Force photo/Staff Sgt. Brian Ferguson.

As a consequence, the collateral damage of such weapons is excessive, and limits its applications. Their capabilities in UAS, on swarm formation, are also limited, given their weight and expensive manufacturing. Therefore, in order to realize precise and surgical attacks, it is mandatory to use smaller platforms that carry smaller and lighter weapons, offering also limited radar firm. Table 1.4 shows details of some weapons of recent development, that can be carried in miniaturized UAS.

Table 1.4: Selected Surgical Weapons, adapted from [20].

Name	Company	Weight	Range	Guidance
AGM-176 Griffin	Raytheon	20 kg.	20.1 km	GPS / INS / Laser
Scorpion	Lock. Martin	15.9 kg.	19 km	GPS / INS / Laser
Martlet	Thales	13 kg.	8 km	Laser / IR
LAHAT	IAI	13 kg.	13 km	Semi-act. laser homing
Hatchet	Nort. Grumann	2.72 kg.	-	GPS / Laser

Figure 1.5: Closer view to the inboard and outboard hardpoints of the Reaper, carrying the before mentioned GBU-12 Paveway II laser guided bombs of 295 kg. Developed in the 1970s, it carries a general purpose warhead.

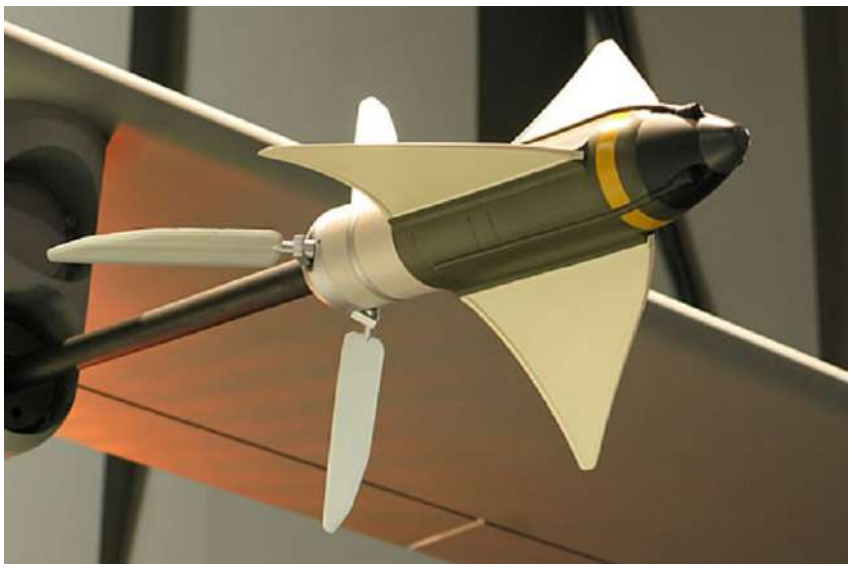

Figure 1.6: Hatchet missile, with deployed fins and flight configuration.

A good representative of this category is the Hatchet missile, manufactured by Northrop Grumman. It is a Miniature Precision Guided Weapon with three laser detectors. It

features tail fins that are used to target the objective with high precision [23]. It also presents a LEO (Lethality Enhanced Ordnance) warhead that limits collateral damage, improving target precision to 1 m, thanks to the advanced onboard guidance systems [24]. In the Predator, for example, the two Hellfire missiles that it can carry could be substituted by up to 24 of these weapons. In the case of the Reaper, this number scales up to 72 [23], and various weapons would be loaded in a single ejector.

Table 1.5 shows details on the warheads of the missiles and munitions listed in Table 1.4. Notice that, in the case of the Hatchet, most of the weapon mass is the warhead. The type of warhead depends on the target characteristics, as well as on the desired operational capabilities.

Table 1.5: Warheads of selected weapons, adapted from [20].

Name	Other characteristics
AGM-176 Griffin	5.9 kg. Blast Fragmentation warhead
Small Smart Weapon, Scorpion	BattleAxe warhead
Lightweight Multirole Missile, Martlet	3 kg. HE blast fragmentation warhead
Laser Homing Anti- Tank, LAHAT	Tandem-charge high-explosive anti-tank
Hatchet	1.8 kg. Lethality Enhanced Ordnance warhead

For example, the Small Smart Weapon, Scorpion, by *Lockheed Martin*, features a BattleAxe Warhead that employs reactive materials [25] (i.e., energetic materials that ignite upon impact), due to shock-induced chemical reactions [26][27].

1.2.3 Other Weapons

Apart from traditional, and surgical options, there are recently developed weapons, which are used in the context of UAS. Many of these are anti-personnel oriented, while

others are oriented towards anti-material or anti-UAS objectives. This section briefly details those which are onboard UAS, and oriented against other UAS.

One of the most extended options to engage UAS is the use of Directed Energy or Electromagnetic Pulses [20]. The highly intense power pulse produced by the source causes a short surge of thousands of volts that can disable or destroy electronic devices onboard a vehicle that does not present effective protection. Furthermore, these weapons can affect the flight Control Systems, navigation and communication functions, or the weapons modules. In general, any electronic module without electromagnetic protection. Moreover, they are highly effective against swarms, an advantage when a global countermeasure is required. Therefore, the electromagnetic pulses can be tuned to cover wide areas. Other weapons rely on restraining mechanisms (i.e., nets thrown from a UAS can be used to capture an enemy drone).

1.3 ACUS Project Framework

The ACUS Project is developed within the effort of the Optoelectronics and Rocketry Department of INTA to develop, design, and test, different solutions that enhance RPAS capabilities. This project, in particular, is in charge of validating and assessing the feasibility of a propulsion architecture that aims to constitute the central core of a future dual-stage missile.

The ACUS Project starts with this Master Thesis. Consequently, this work is the leading edge endeavour, and there are no previous works on this specific topic. All modules, electronics, and designs are developed from the scratch. The only information available is related to the employed propellants (i.e., information about performance, composition, and possible uses is available from previous technical reports and research articles [28][29]).

1.4 Objectives of the Thesis

The main objective of this Master Thesis is the design, development, and testing of a proposal for the propulsive architecture of a dual-stage missile, to be launched from RPAS platforms. The study will focus on the individual feasibility of both stages. A first stage is based on a gas pressurized system that ejects the missile from the canister, while the second stage is a conventional solid rocket motor (or boost motor [30]), that propels the missile. See Figure 1.7 for more details. The testing of the two platforms will be carried on laboratory (in the case of the electronic or ignition modules, to check response times and correct functioning), and on experimental tests on ground (for the launch of the complete system). The project focuses on the individual validation of each of the modules, while their integration is left for future works.

Different operational requirements need to be met:

- Short response time: the missile must be deployed in less than 40 ms after the launch command is issued from the operator.
- Manufacturing: the missile manufacturing must be based on a cost-effective solution, such as additive manufacturing, with limited cost (< 100 €), as the target is low-cost RPAS.
- Payload: the missile must be able to carry > 100 g. payload, for its intended use.
- Design and performance: the second stage, a rocket motor, should try to enhance erosive burning to obtain high thrust profiles in a small platform.

Moreover, this technical project is also intended to serve as an introduction text to any engineer interested in designing, building, and testing a propulsion solution as the one proposed, providing a strong theoretical foundation that drives every design step.

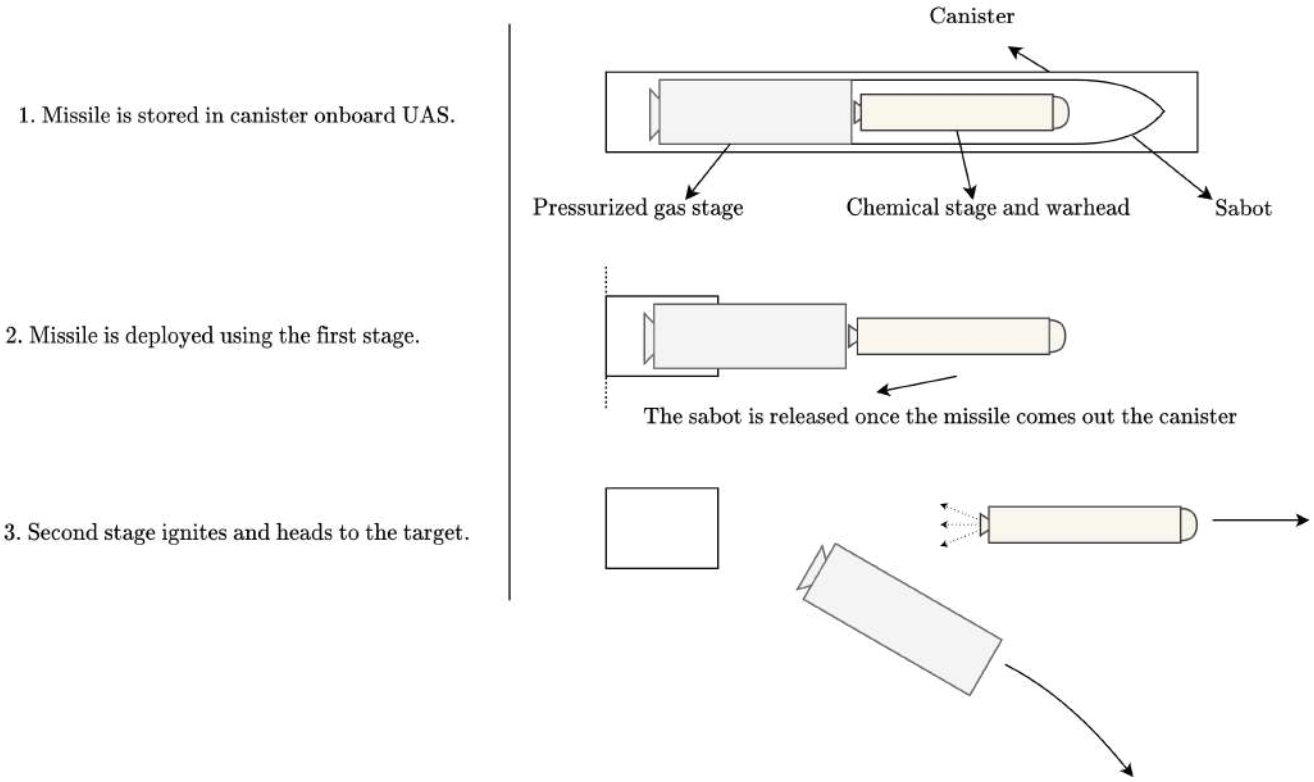

Figure 1.7: ACUS missile operation schematics.

1.5 Regulatory Framework

The work with explosives, propellants, or ammunition is severely regulated by different standards and normatives, at national and international levels. Similarly, standards that apply to the design of certain components are also issued by the appropiate authorities. At Spanish National Level, the military normatives that apply to this project are the *Norma Militar Española*, 'NME'. At international level, the normative that applies is given by the Standardization Agreements of NATO, STANAGs.

In particular, the reception of propellant samples used for *ACUS* First Stage are regulated by the following directives (in Spanish):

- *NM-I-2264 EA, Instrucciones básicas para la recepción de pólvoras, exposivos, artificios y material pirotécnico* [31].
- *NM-P-2442 EMAG 1ª Eda, Pólvoras. Condiciones técnicas de carácter general para la definición, inspección y recepción de cualquier tipo de pólvora y de las cargas confeccionadas con ellas* [32].
- *NM-C-2443 EMA, Cargas propulsoras para cohetes y misiles. Condiciones técnicas de carácter general para su definición, inspección y recepción* [33]

For the storage of those propellant samples, the reference is The *Spanish Military Normative NME 2379* [34]. More guidelines on such storage are given by *NATO's Manual of Safety Principles for the Storage of Military Ammunition and Explosives* [35][36], and by *Best Practice Guide on National Procedures for Stockpile Management and Security* [37], by OSCE (Organization for Security and Co-operation in Europe).

For the design and safety characterization of the rocket ignition system, guidance is provided by STANAG 4368 (Ed. 3), *Ignition Systems for Rockets and Guided Missile Motors - Safety Design Requirements* [38]. Ignition and pyrotechnic train of the first stage is excluded from this agreement since, from section EXCLUSIONS of [38], it complies with the following;

- Devices containing thrusters and gas generators which the NSAA (i.e., National Safety Approving Authority) agrees do not present sufficient hazard.
- Rocket-assisted projectiles and rocket-propelled grenades which the NSAA agrees do not present sufficient hazard
- Pyrotechnic countermeasure devices which the NSAA agrees do not present sufficient hazard.

This page intentionally left blank

2

Design of the First Stage Propulsion

This chapter details the design process of the missile first stage, based on a pressurized gas solution. Different alternatives are studied, and a final configuration is reached. Extensive prototyping using Additive Manufacturing is employed to iterate rapidly during this design phase.

Contents

2.1 Introduction

The duty of the first stage propulsion is to rapidly deploy the missile once the launch command is issued from the operator, or from the onboard computer (to automatically deploy a countermeasure, for example). There are a variety of solutions that have been employed in the past to solve this issue. The general requirements that a missile deployment technology needs to satisfied are the following [39]:

- Reaction time: it needs to be sufficiently fast to be effective.
- Safety: it must ensure that the missile deployment is able to function without posing a significant hazard to other equipment or personnel.
- Reliability: the deployment method must be capable of ejecting the missile from the canister with a low failure rate.
- Operation: it must deploy the second stage with the adequate velocity. Thus, the total impulse must be superior than an specific threshold, that depends on the object mass and final velocity.

Typically, to deploy missiles or torpedoes from their storage tubes or canisters, Gravity Launching Systems, Impulse Launchers, and Reaction Launchers [39] are used. The first category, as its denomination suggests, relies on gravity to deploy the missile or

weapon. The second relies on a force external to the vehicle to clear the weapon from the launching vehicle (i.e., a cannon is an example of an Impulse Launcher). Finally, on the third category, the force that drives the weapon out of the launcher is originated from the weapon itself; this force is typically provided by the propulsion module of the missile, acting during the very first stages of the weapon flight [39][i].

The system, which is best suited for the ACUS project purposes, is the Reaction Launcher. This deployment architecture is applied in most of the missiles. Note that, in this category, the system is fully embedded within the missile body, and does not required any external equipment. In contrast, other architectures such as Impulse Launchers, if used with compressed air, required an external pressurized air supply and piping. Therefore, there would be an associated increase in weight and complexity which is not desired for a small platform, such as an RPAS.

That reaction (i.e., thrust) given to the weapon can be provided by different means. In general, small missiles such as the Stinger (Low Altitude Air Defense missile) employ a launch (or ejection) rocket motor that ejects the weapon around 9 meters from the tube, until the flight motor is ignited [40]. That main stage motor fires after a short delay, to ensure that there is sufficient distance between the launcher and the missile. The launch motor falls off once the missile is clear from the canister. Figure 2.1 shows the firing of a Stinger. The launch motor is already separated from the missile body, at the canister exit. The missile Mistral, developed by *MBDA*, is another example that uses a disposable launch motor. In general, both the launch and the cruise missile employ solid rocket propellants, due to their safer storage, robustness and easier handling.

[i] A cruise motor should start afterwards to provide propulsion during the flight phase.

Figure 2.1: U.S. Marines assigned to Alpha Battery, 2nd Low Altitude Air Defense Battalion firing an FIM-92 Stinger missile during exercise Arctic Edge on Fort Greely, Alaska, March 15, 2018. Image: U.S. Marine Corps photo by Lance Cpl. Cody J. Ohira/Released.

Figure 2.2: Harpoon missile launched from the USS Shiloh, September 15, 2014. The missile is deployed from one of the tubes of the multiple-tube launcher system, with the ignition of the launch motor. Please notice the important rocket plume, blast, and exhaust gases that the launch motor produces. Image: US Navy/Mass Communication Specialist 3rd Class Kevin V. Cunningham.

Larger weapons, such as the Harpoon Anti-Ship missile, also employ a similar architec-

ture, in the sense that an initial motor deploys the weapon from the canister. However, in this case, the launch motor is not disposable, but part of the missile body. It is located at the rear part of the missile, and provides the initial thrust. Figure 2.2 shows the launch of a Harpoon from a combat cruiser. The initial launch motor propels the missile out of the launchpad.

Due to the operational characteristics of the micro-missile under study, which is to be fired from a small RPAS platform, the solution that is proposed for the deployment is the use of a gas generator, employing a pressurized gas reservoir embedded within the first stage, that pushes the second stage of the missile out of the canister. Therefore, it is a similar solution to a classic launch motor (recall Figure 1.7 for a better understanding of the missile architecture), but employing a *cold gas* thruster, in similarity with those employed in satellites for attitude control, for example. This option can prevent damage of ground equipment or peripheral missiles and other UAS modules [41], as the blast and exit gases are not as detrimental as those coming from a solid rocket motor. Moreover, this first stage (i.e., launch motor) falls off once the missile is cleared from the canister, with the aim that the total weight of the missile is lower during the flight phase, allowing additional warhead content. Therefore, it is needed to design a gas generator, to later build around it the body of the first stage itself.

2.2 Gas Generator

The Gas Generator is in charge of producing a given gas mass flow rate, at a sufficiently high pressure, capable of producing the required thrust for missile deployment. This thrust is produced by expelling the pressurized gas through a nozzle.

2.2.1 Design Concept

The proposal design is based on proved architectures commonly employed in parachute deployment of amateur rocketry: a firing pin perforates the seal of a cartridge containing a pressurized gas, which expands towards the exit. This gas release is used for the missile initial propulsion, based on the well-known Equation 2.1.

$$F = \dot{m} \cdot V_e + (P_e - P_{amb}) \cdot A_e \tag{2.1}$$

where $\dot{m}$ is the mass flow rate of gas exiting the nozzle, V_e is the exit velocity, P_e is the gas exit pressure, and P_{amb} and A_e are the ambient pressure and the nozzle exit area, respectively.

Recalling Equation 2.1, it seems reasonable to increase the mass flow rate and the exit velocity as much as possible, in order to increase the thrust provided by the gas expansion. The pressure term, instead, should be minimized in full measure. When it is null, the nozzle is said to be *matched*.

There is a series of design decisions which need to be tackled through out the iterative design process of the gas generator. Once a general solution for each problem is found, and the integration among them is discussed, the manufacturing and testing of components can be initiated. The main design steps are listed next:

1. Design the method to extract, in a simple and reliable way, the gas from the reservoir. The response time of such method, after the missile launch command, must be lower than 20 ms.

2. Design a method to drive the gas towards a nozzle for thrust production.

3. Integrate the whole system.

The first design problem was the development of the firing pin mechanism. It needs to be sufficiently strong to perforate the sealing of the pressurized cartridge, but it also needs to be fast enough to overcome the response time limitations. The first explored

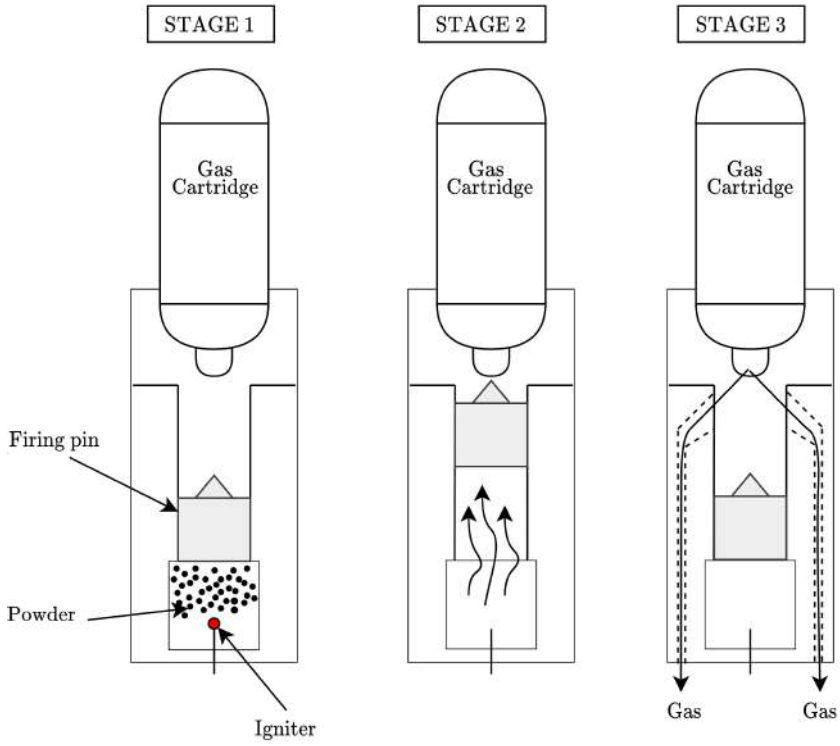

Figure 2.3: Schematic of operation of the gas generator. In the first stage, left side, the system is off. Once the launch is triggered (stage 2) the igniter receives current and ignites the powder surrounding it. The gas created by the powder combustion pushes the firing pin upwards, perforating the pressurized gas cartridge. In stage 3, the gas is released and travels through specific channels to the outside, generating thrust.

concepts were based on a mechanical system with a needle restrained with a spring. When the system is activated, the spring releases the needle, perforating the cartridge seal. However, the mechanical complexity of such system, that would increase significantly its preparation time, was a major handicap. Rapidly, the iterative design moved towards a system that uses the gas created by the combustion of a powder charge to push a lubricated firing pin through a channel, until it impacts the cartridge seal.

The schematics of operation are shown in Figure 2.3. No mechanical connections are

needed for the release of the gas, which is generated by the powder charge, and that provides enough internal pressure to move the firing pin and perforate the seal.

Once the firing pin concept was developed, the second design problem that needed to be tackled was the guidance of the released gas towards the outside (stage 3). The first issue that was encountered was the fact that the natural path of the released gas is blocked by the firing pin mechanism. Therefore, the firing pin needs to be retracted, after the seal perforation, to its original position. This is done by means of a spring, that keeps the firing pin blocked at its position, unless a superior force (i.e., pressure force exerted from the powder combustion gases) pushes it upwards. Once the firing pin has perforated the cartridge seal, it is driven back to its original position by the spring, leaving free the path for the pressurized gas. In addition, the spring also ensures that the firing pin is centered, guaranteeing a precise impact at the cartridge seal.

The second issue in the gas guidance is the need to machine specific ducts that collect and drive the released gas towards the exit, generating thrust. Those channels are also used to collect the gas from the powder combustion, so that the internal cavity is free of combustion gases that would be compressed as the firing pin is driven back by the spring. Figure 2.5 shows the cross-sectional view of the chosen design, in its deactivated configuration. The firing pin is compressed by the spring against the propellant capsule, guiding the firing pin towards the seal and driving it back once it has perforated the seal.

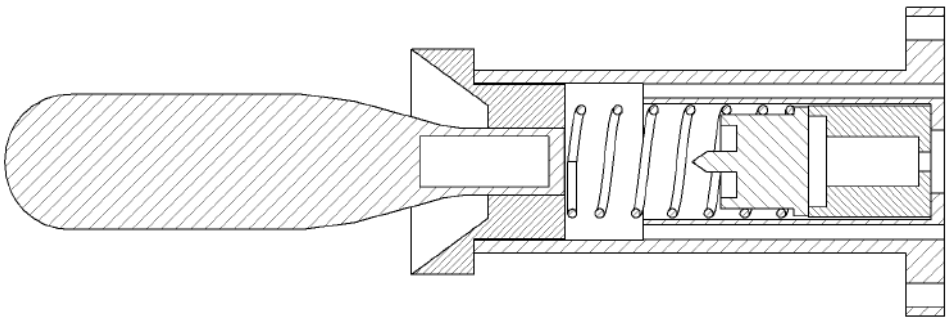

Figure 2.4: Schematics of the gas generator architecture.

2.2.2 Gas Generator Components

2.2.2.1 Pressurized Gas cartridges

Dioxide Carbon, CO_2, was selected as pressurized gas, because it is a very stable gas, with well known expansion characteristics, non-reactive and non-toxic. It is widely available in the form of pressurized cartridges, of various sizes, which eases the design process. In particular, it is decided to start with cartridges containing 16 or 25 g. CO_2, compressed at 66 bar. If the mass flow provided by such cartridge is not enough, the design could easily adapt bigger cartridges, up to 200 g.

Moreover, in case of a gas leakage, there is little hazard of explosion, or accidental ignition, as it does not react with fire, or spark remnants after powder combustion. CO_2 pressurization is also significantly cheaper, when compared to other gases, constituting an advantage for mass production. Cartridges are commercially available, although custom designs could be introduced in the future for better adaptation of need. For the current objectives, such commercial cartridges are completely appropiate.

2.2.2.2 Electric igniters

An electric igniter (i.e., match) is a device that ignites when a predefined electrical current is applied. Consequently, it is commonly employed to ignite propellant grains or powder charges. Additionally, electric matches are commonly employed in fireworks shows or displays. The brand denominator of the igniters employed used for ACUS are prototypes ZX8308-1. Their main characteristics have been listed in Table 2.1.

Table 2.1: Characteristics of electric matches

Characteristic	Description
Net explosive material weight	0.04 g
Minimum Working Current	0.75 A
Nominal working current	1 A
Maximum working temperature	40 °C
Resistance (1 meter cable)	0.85 $\Omega \pm$ 0.3 Ω
Response time	3 - 30 ms

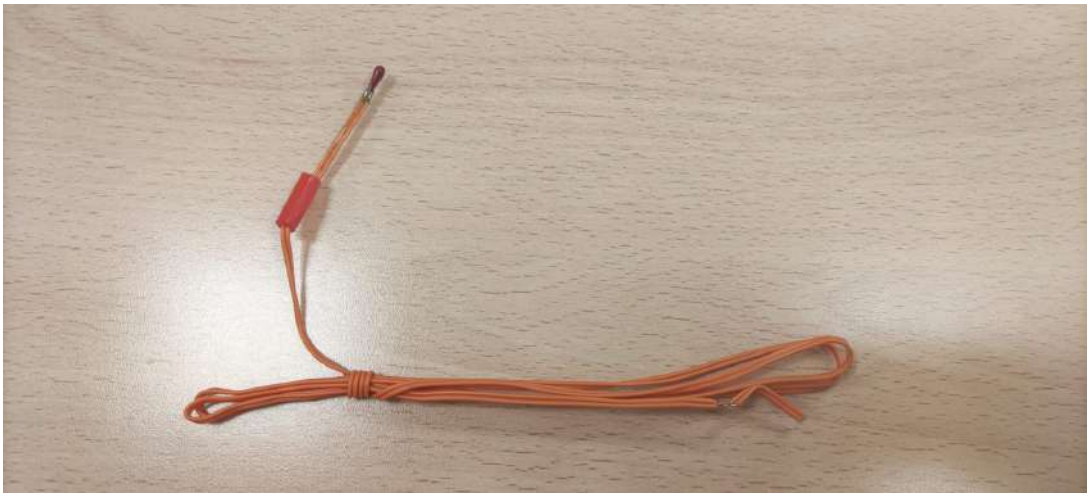

Figure 2.5: Electric Match ZX8308-1. The picture shows the electric connection, the electric match head, and its cover, used to concentrate the flame created by the match ignition.

One of the main concerns related to the use of this system is its response time. In the studied application (i.e., military field, for weapon and countermeasure deployment) such variable is critical. It is measured from the triggering of the launch signal by the operator, until the electric match is ignited. Ten ignitions were conducted in an experimental campaign with a high-velocity camera, to verify that the response time and the ignition characteristics are the desired ones. Six different time-stamps of an electric match during one of the ignitions are presented in Figure 2.6a - Figure 2.6f

The complete match ignition takes place in approximately 0.5 s. The extinguishing flame is appreciated in Figure 2.6f. The highest flame extension is reached after 170 ms, approximately (see Figure 2.6d). This experimental campaign verified that the

electric match igniter presents appropiate response time, on average, nearly 4 ms. That means that the complete system response time (i.e., time it takes to ignite the match, ignite the powder charge, and extract the gas from the cartridge) will be likely limited by the combustion of the propellant charge and the movement of the firing pin, and not by the ignition of the electric match.

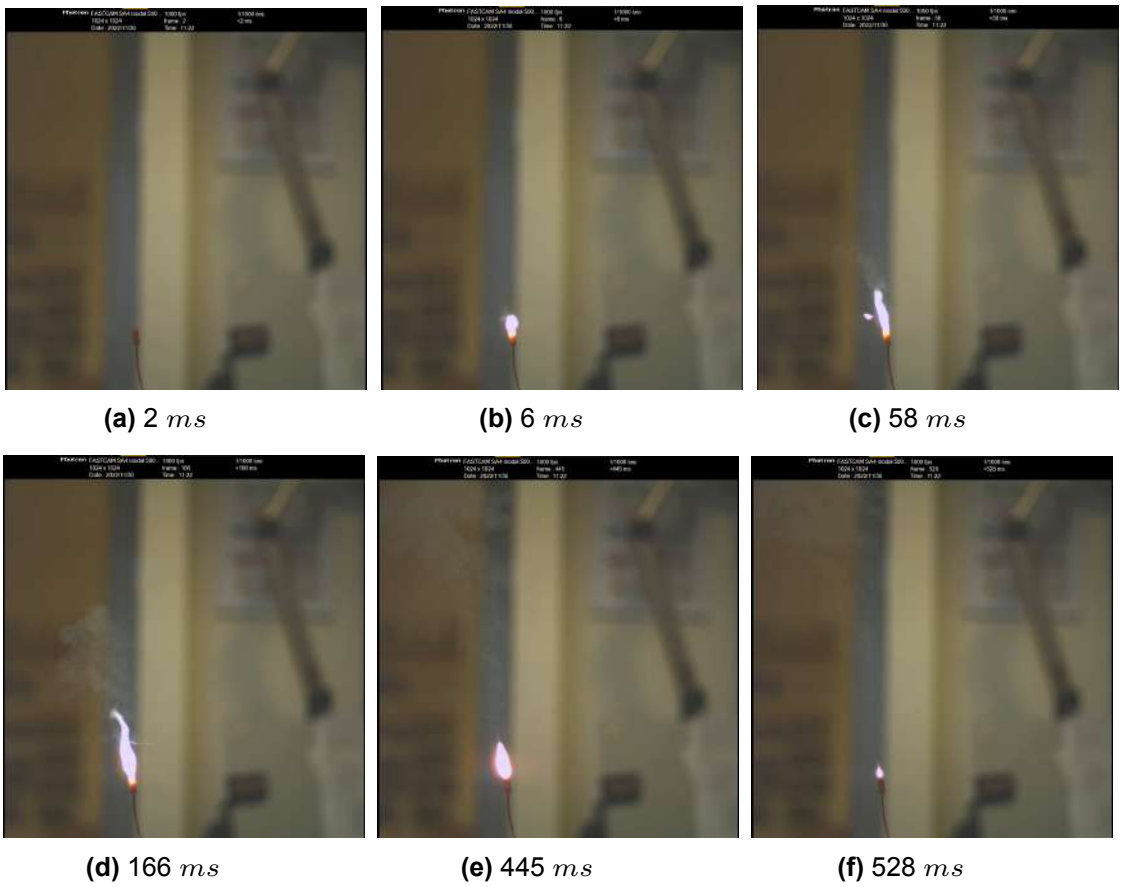

(a) 2 ms **(b)** 6 ms **(c)** 58 ms

(d) 166 ms **(e)** 445 ms **(f)** 528 ms

Figure 2.6: Phases of electric match ignition after triggering. Stage (b) shows an already ignited match. At stage (d), the flame created by the electric match reaches its full extension. The response time, after the triggering of the launch signal, and before ignition, is around 4 ms.

2.2.2.3 Propellant

The powder selected to push the firing pin upwards with its combustion gases is a well-characterized nitrocellulose double base propellant [29][28]. Its constituents are

listed in Table 2.2. In good conditions, it is a NC powder that can be easily manipulated without high ignition hazard. Its combustion characteristics are also suitable for this use, and it is in granulated form.

Table 2.2: Constituents of the propellant employed as powder

Constituent	% mass
Nitrocellulose	89.18
Nitroglycerine	8.5
Akardite II	1.21
Ethanol	0.54
Diethyleter	<0.01
Potassium Sulfate	0.6
Moisture	0.61

Figure 2.7: Propellant used for the gas generator

This powder is a double base rocket propellant, which is used for tactical rockets, artillery, or short and long gun ammunition [28][42]. The main component of such propellants is nitrocellulose, combined with nitroglycerine. The oxidizer and fuel are in the same molecular structure, Hence, these propellants are also called *homogeneous propellants*. Moreover, different additives are added to these compositions to improve

certain operational characteristics: up to 10%wt of a double base propellant may be due to additives [43].

In the propellant used for this project, one of the main additives is Akardite II. It is a stabilizer that improves the propellant chemical stability over time (i.e., degradation and stability are main concerns in the storage of nitrocellulose propellants).

2.2.2.4 External cylinder

The external cylinder is in charge of holding all the components of the gas generator, and is intended to be used as the interface between such system and the external body of the first stage. Therefore, its design needs to consider both requirements.

First of all, it needs to feature a hole at the bottom of the inner channel, to allow the igniter cables to pass through. Secondly, it needs to present some machined channels that collect the gas from the cartridge, towards the exit, where the nozzle will be placed: 5 channels are machined. Figure 2.11 shows the external cylinder final design.

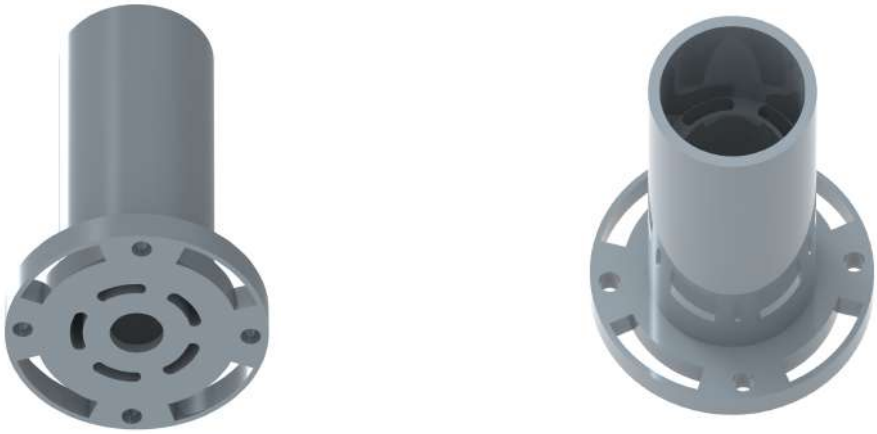

Figure 2.8: External Cylinder.

At the bottom face of the cylinder, near to the gas exit, there is an edge protrusion. This part of the cylinder features 4 holes, that will be used to thread the gas generator to

the stage body. Additional machining is included near those holes to reduce the total weight of the system.

2.2.2.5 Cartridge adaptor

The cartridge adaptor is threaded to the internal face of the external cylinder, at its upper part, and serves as interface between the cylinder and the gas cartridge. There are no specific constraints or design requirements for this piece, so that a simple design is followed. Figure 2.11 shows the final design.

Figure 2.9: Cartridge adaptor. The thread is not shown in this picture.

2.2.2.6 Firing Pin

The firing pin is the responsible of the gas release. In its initial configuration, it is kept at the bottom of the cylinder inner channel due to the spring force. However, once the propellant charge is ignited, its combustion gases exert a force in the lower face of the firing pin, greater than that of the spring. As a consequence, the firing pin is moved upwards through the internal channel of the system, until it perforates the cartridge. Afterwards, the combustion gases vanish through out the machined ducts, the spring pushes back the firing pin to its original position, and pressurized gas exits the system through the channels.

The design of this component is based on a cylinder with an embedded iron spike, with a sharp edge. Such spike needs to be sufficiently wide so that the cartridge perforation is big enough to allow a fast exit of the pressurized gas.

Figure 2.10: Firing Pin

2.2.2.7 Propellant Capsule

The propellant capsule stores the charge that will be ignited by the electric match, which is also located there, surrounded by the powder. Its combustion gases will push the firing pin. It features a cylindrical shape, with an inner compartment where that electric match is placed. The available space is filled up with a propellant charge of 2-3 g.

Figure 2.11: Propellant Capsule. The inner compartment holds the electric match.

There is a machined hole in the bottom part of the capsule to allow the connection of the electric match with the electronics in charge of triggering the firing.

2.2.3 Assembled Gas Generator

The design of the completed, and assembled, system, is shown in Figure 2.12. The external cylinder is the blue external piece, the firing pin is the pink component, the propellant capsule is the green part, and the cartridge adaptor is the black piece.

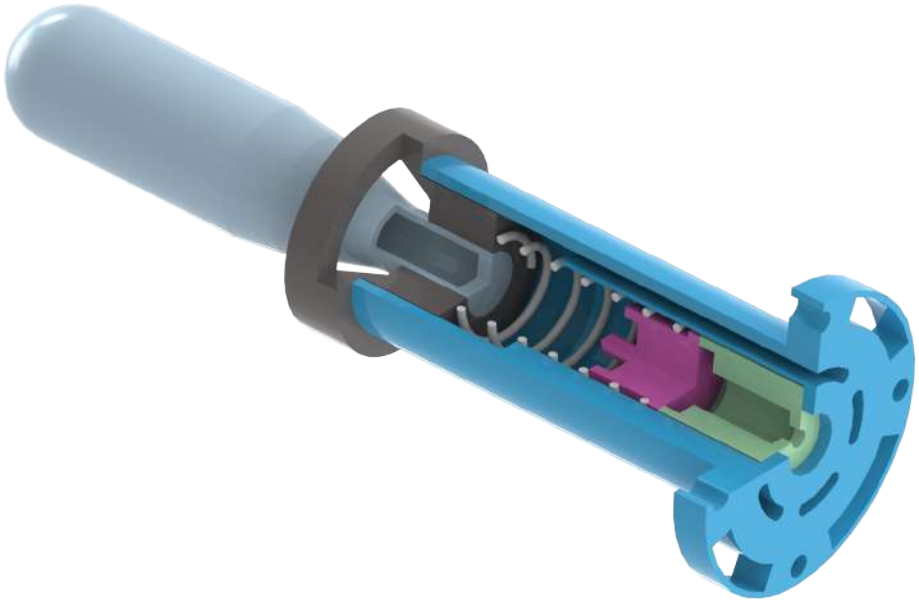

Figure 2.12: Complete Gas Generator Design

The next design step in the development of the first stage is the design of its external components (i.e., nozzle and body). The nozzle's main duty is collecting gas coming from the internal ducts to form a uniform stream that expands, accelerates, and creates thrust. The body's duty is to hold all the system components and provide an adequate structural integrity.

2.3 Nozzle

The nozzle is a fundamental component in any propulsion system. It modifies important characteristics of the flow that passes through it, like the pressure and velocity. Their primary purpose is the generation of thrust by expanding a high-pressure, low-velocity gas coming from a combustion chamber. Consequently, the first term of Equation 2.1 increases, and thrust is produced. In this case, the gas is coming from a pressurized reservoir, travels through a set of channels to the nozzle, and exits the system.

For this propulsion system, the main purpose of the nozzle is to prove that propulsion is feasible, with the studied configuration. A classic convergent-divergent nozzle is proposed, without specific focus on performance objectives, which are left for future works. Subsequent design stages or project phases could focus on an specific nozzle design. The prototyping is performed using additive PLA and photopolymer manufacturing. Therefore, there are not strict manufacturing constraints.

A nozzle prototype, and a manufactured version, are shown in Figure 2.13. They present external holes used to thread the nozzle to the external cylinder and the body.

Figure 2.13: Nozzle design, and manufactured version with resin.

Note that there is an open section on the nozzle lateral. This section holds an electric module that connects the igniter cables to the external electronic modules. That connection section must be completely sealed, to avoid leakage of gas through the walls. Consequently, the nozzle is not only the main responsible of thrust production, but it is also the interface between the external electronic modules and the gas generator. An early version of the nozzle, connected with the gas generator through the electronic module, is shown in Figure 2.14.

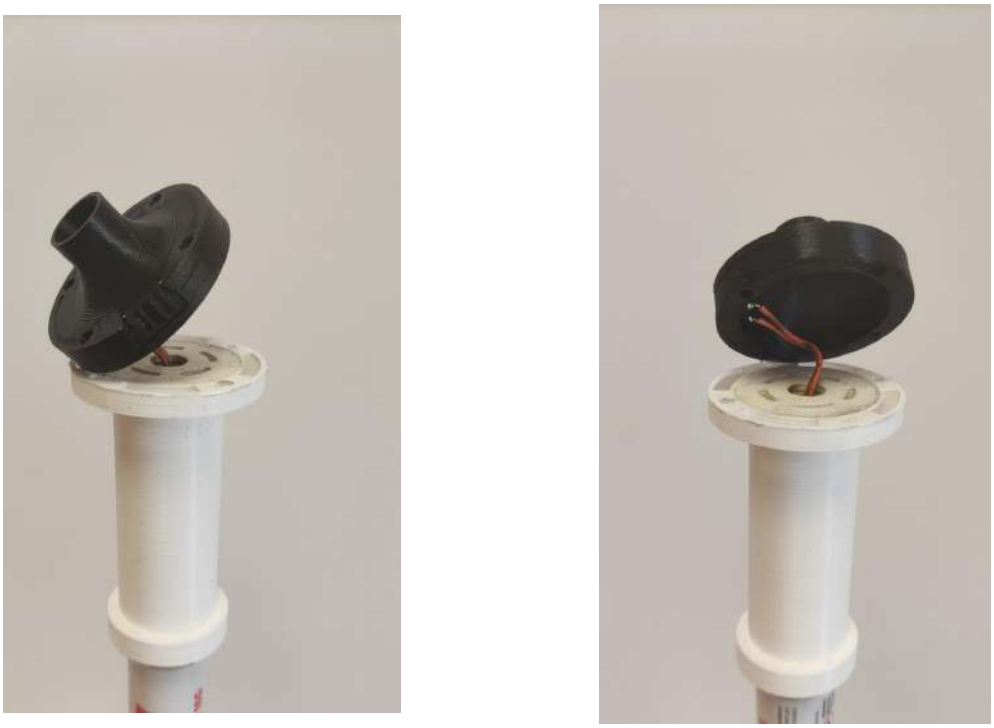

Figure 2.14: Nozzle early version and gas generator connected through the electronic module.

2.4 Body

The external structure must provide structural integrity to the whole system, and it features inside the gas generator. It pushes the second stage of the missile out of the canister before it ignites. Despite those duties, it does not need to have an specific

aerodynamic shape, as its flying time is limited, and not critical for the mission objectives. Figure 2.15 shows two views of the external body design.

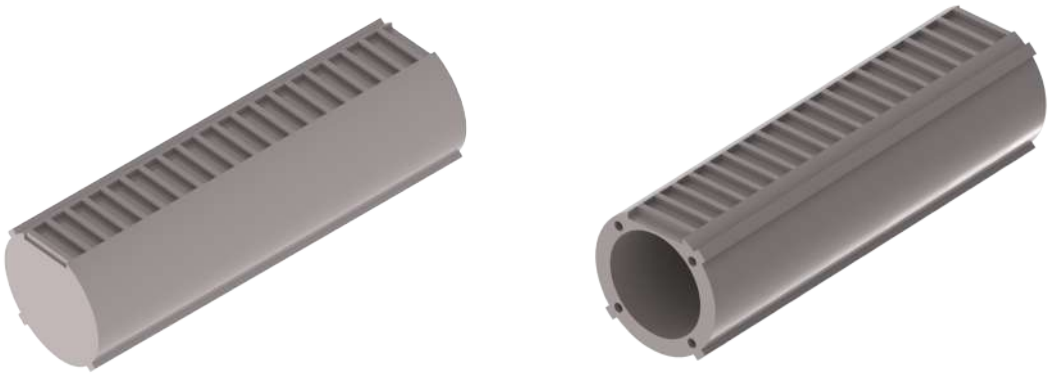

Figure 2.15: First stage body design.

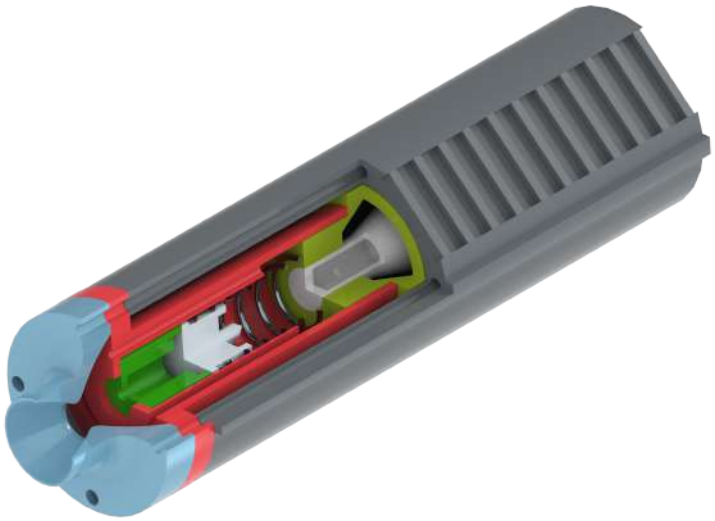

Figure 2.16: Assembled first stage design. Threads and screws are not shown.

The proposed design is a simple cylinder that can hold inside the complete gas generator. It is connected to the gas generator and the nozzle through threaded bolts. Moreover, a calibrated pattern is included in one of the laterals. Such pattern will be used as a calibrated reference to measure the flight speed of the first stage during the experimental campaign, with high velocity cameras. Lastly, it includes three rails,

which are used to guide the stage inside the canister, and to ensure a correct placement inside of it.

Figure 2.17 shows the complete assembly of the missile first stage. The stage body holds, inside, the complete gas generator system. The later is connected to the nozzle and the body through threaded connections and screws.

Figure 2.17: View of the external and internal components of a manufactured first stage.

3

Design of the Second Stage Propulsion

This chapter develops a numerical model that describes the second stage performance. Afterwards, it details its manufacturing based on a design point fixed by a performance-oriented parametric analysis.

Contents

3.1 Introduction

In the field of rocketry, multi-stage vehicles are widely used for a variety of reasons. Perhaps, the most important one is the fact that a rocket with disposable stages (i.e.,

which fall off the vehicle once they have been used) is more efficient: it can carry the same final payload (e.g., warhead, satellite, etc) with less propellant mass. While this is the principal reason why space rockets and intercontinental missiles are *staged*, for small missiles the operational requirements are the main driver behind this architecture selection.

Missiles such as Stinger, Mistral, or ACUS, require a first launch motor to deploy the missile from the canister. Afterwards, a rocket motor is ignited, propelling the missile during the mission flight. This rocket motor is in charge of satisfying the propulsion needs of the vehicle, and it ignites once the first stage has fulfilled its duty. Typically, this second stage is ignited once an specific event is detected: a given threshold in acceleration is surpassed, or after an specific time delay following first stage ignition, for example.

Table 3.1: Specific Impulse of various propulsion technologies. Adapted from [44][45].

Propulsion Technology	Specific Impulse [s]
Chemical - Solid	200 - 310
Chemical - Liquid	300 - 460
Chemical - Hybrid	300 - 500
Electrical (arc heating)	400 - 2000
Electrical (ion thruster)	2500 - 10000

Consequently, the propulsion of this stage is critical for mission accomplishment. It must provide enough thrust for the weapon to reach the selected objective in time and position, and sufficient impulse to provide it with the adequate velocity. For ACUS, a solid rocket motor (SRM) is proposed. This type of rocket motors serves as the propulsion back-bone and work horse for missiles and space launchers [28][46], where restart or throttling is not required. It is a well-known technology, that offers simplicity and robust operation. In principle, its specific impulse is not high, but modest compared to other alternatives such as liquid or electric propulsion [44][45]. Table 3.1 shows the Specific Impulse of various propulsion technologies. The specific impulse, I_{sp}, is

usually expressed as given in Equation 3.1.

$$I_{sp} = \frac{F}{g_0 \cdot \dot{m}} \tag{3.1}$$

where $\dot{m}$ is the propellant mass flow rate, F is the thrust, and g_0 is the gravity constant at the Earth's surface. A modest I_{sp} means that higher propellant mass flow rate, and, hence, higher propellant mass, is required to achieve a given thrust. However, the relation between impulse and density of such propellants is very interesting [47], making it the preferable choice for applications in which simplicity is desired, and low volume is available. Hence, it is the optimal choice for ACUS second stage propulsion.

This chapter describes the development of an in-house performance code that predicts the behaviour of a solid rocket motor (SRM) with internal cylindrical geometry, given the propellant and motor geometric characteristics. This performance model includes an erosive burning module. After validation of such model, using reputed codes and available data from literature, a performance-oriented parametric analysis is studied. Baesd on such analysis, a design point is fixed, and a SRM of the desired dimensions is manufactured.

3.2 Fundamentals of Solid Rocket Propulsion

Rocket Propulsion is the science that studies the movement of vehicles propelled by rocket motors. Solid propulsion is a sub-field[i] of rocket propulsion in which a fuel and oxidizer, in solid state, are burned. The combustion reaction between those components creates hot gases which are accelerated through out a nozzle, leaving the rocket with high speed. From Newton's Third Law, the motion of the expelled gases leads to

[i] Other propulsion alternatives are liquid propulsion (based on the burning of fuel and oxidizer in liquid state) and electric propulsion, for example.

an opposite reaction from the medium, pushing the rocket forward. This force moving the rocket is called the thrust of the rocket, Equation 2.1. Figure 3.1 shows the main components of a classical solid rocket motor.

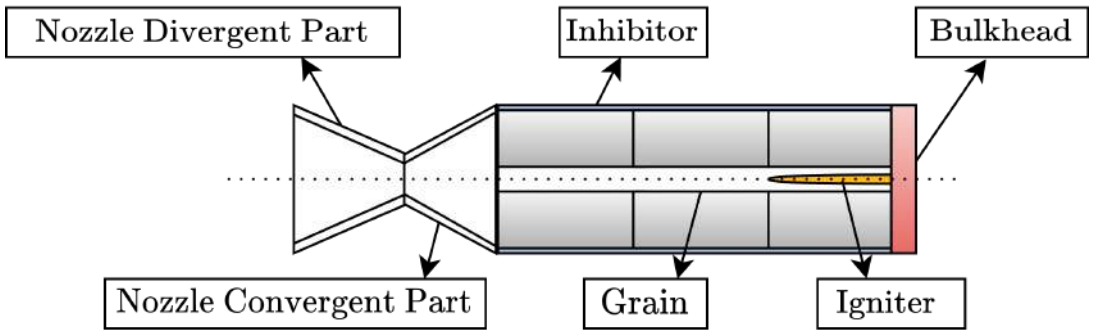

Figure 3.1: Solid Propellant Rocket Motor schematics. Adapted from [28].

In Figure 3.1, the grains are energetic materials[ii] that are burned during the rocket motor operation. These are manufactured with various internal shapes, which will affect the motor performance. The thrust curve will be decisively affected by the internal configuration of the grain, and, therefore, by the burning area evolution. These grains are placed inside a casing, which is typically manufactured with advanced metal alloys. Between the casing and the grain, an inhibitor is placed, to protect the casing from the burning grain, and ensure its structural integrity. These often consist of relatively thin sheets of flexible thermal insulator materials [48]. These materials may be also designed to operate at particular regions of the grain, to modify the burning area, by blocking the combustion at certain locations [49].

The rocket motor operation starts with the igniter, responsible of starting motor ignition, by heating up the propellant surface, until temperature is high enough to initiate combustion (i.e., temperature must be above autoignition temperature). The igniter must also raise motor pressure above the critical pressure required for self-sustained and

[ii] These materials store chemical energy that can be released through different methods.

stable combustion. The ignition system usually consists on an initiator, typically an energetic material, which is ignited by an electrical, chemical, or mechanical stimulus [50]. The energy released upon initiator combustion provides the necessary energy for propellant ignition. This is a critical phase of the operation characterized by transient and unsteady phenomena that may induce pressure oscillations resulting on mechanical stresses over the motor structure [51][52]. The design of a correct igniter, that ensures complete ignition, is a complex task, that will involve an important amount of work for ACUS.

Lastly, the nozzle is placed at the exit, and it usually features a convergent-divergent shape. As it will be detailed later, the nozzle transforms the internal energy of the gases coming from the combustion chamber into kinetic energy, increasing their velocity, and generating thrust, following Equation 2.1. This fundamental component is the ultimate responsible of rocket propulsion, and its design involves certain complexities which need to be tackled carefully.

3.3 Design Methodology

The design from scratch of a rocket motor is a highly complex task. Several open questions need to be answered. For example:

- *What propellant should be used?*
- *What dimensions and internal design should the propellant present?*
- *What shape should the nozzle present?*
- *What performance parameters should be optimized?*

These are just a few questions from the complete set of decisions that a rocket engineer must answer along the design of a rocket motor, and they will be tackled in the following pages. The number of design choices is that high, that in a first approach, a

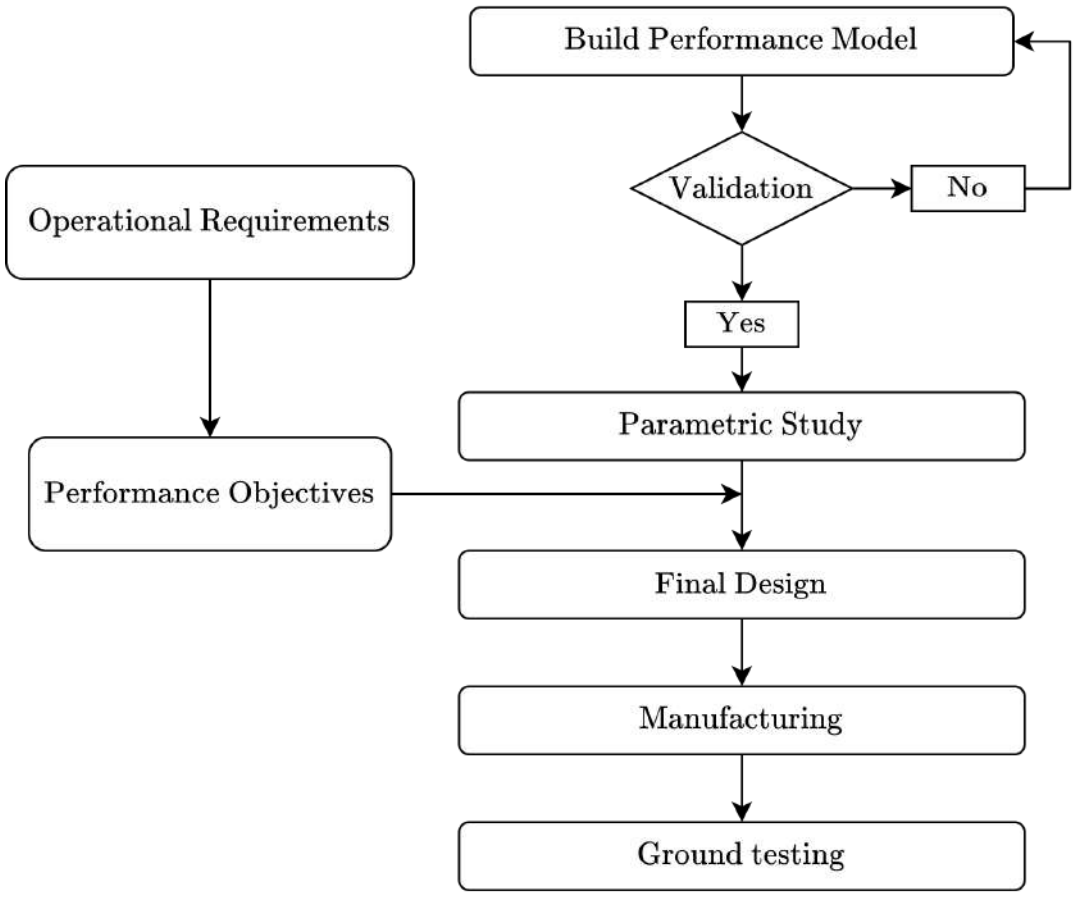

Figure 3.2: Rocket motor design flowchart

performance-based design following a parametric study is the most suitable option. In this parametric study, however, a few variables have been fixed, exiting the parametric space, due to manufacturing constraints, designer decisions, or simplicity.

Therefore, the design approach that is to be followed in this project is rooted on a performance-based analysis: a model for the rocket motor with certain simplifications is proposed. Once the performance model is validated, a parametric study using the design choices is developed. Finally, a design solution is selected based on performance variables, such as the thrust, or the specific impulse. A flow chart depicting this design methodology is shown in Figure 3.2. Evidently, the performance objectives that affect the final design are based on the operational requirements set on the missile by

the customer: desired speed, payload (and consequently, required thrust), etc.

The validation of the performance model will confront the developed program against existing reputed codes.

3.4 Performance Model

This section develops a performance model of the rocket motor whose ultimate objective is the development of the thrust and pressure curves. Before entering into the theory underlying the model, it seems useful to list all the design variables that affect the motor performance. Table 3.2 shows the complete list of variables that conform the design parametric space. Some of these will be later fixed, so that they will not be degrees of freedom. Note that the first 5 variables are propellant-dependant. They are listed here since they appear independently in the model equations, but once the propellant is chosen, they are fixed by its chemical composition and the operating conditions.

3.4.1 List of assumptions

The model that is proposed for this project is simple, although it still presents certain complexities. A complete, and strict, analysis would require a gargantuan amount of work, outside the scope of this project[iii]: internal ballistics analysis, CFD simulations of the internal combustion, structural analysis of both the grain and the casing, thermodynamic studies of the combustion, etc. The list of assumptions presented here [53] are typically used in preliminary rocket motor design, and they may be corrected in

[iii] This does not mean that the presented model is not rigorous. For the current application (a miniaturized rocket), the posed equations and the theory used are completely valid.

Table 3.2: List of model variables.

Variable name	Abbreviation
Ratio of specific heats	γ
Average specific heat of combustion gases	C_p
Combustion temperature	T_0
Burning rate pre-exponential constant	a
Burning rate exponential constant	n
Number of grains	m
Length of grains	l
Total propellant length	L
External grain diameter	D
Internal grain diameter (if cylindric)	d_0
Thickness of inhibitor	t_i
Thickness of casing	t_c
Nozzle throat area	A_t
Nozzle exit area	A_e
Nozzle entry area	A_1
Initial grain temperature	T_{amb}
Initial pressure	P_{amb}
Casing material yield stress	σ_y

future works and iterations. Still, the presented model must characterize with enough accuracy physics and performance of the rocket motor, as the validation will show:

1. The chemical reaction products are homogeneous.
2. All species through the motor are in gaseous state. There are no other phases present (i.e liquid, solid).
3. Gases follow the perfect gas law.
4. Flow is adiabatic: heat transfer to the rocket walls is negligible.
5. Boundary Layer and friction in the motor walls are not considered.
6. There are no discontinuities in the flow through the nozzle.
7. Transient effects during ignition, pressure instabilities, and vibrations are not considered. The flow of propellant is steady and constant.
8. All gases leaving the rocket do not have transverse components in velocity, they are all axially directed.

9. Across any given section normal to the motor axis, thermodynamic variables and velocities are uniform.
10. There is chemical equilibrium in the rocket chamber, and once the gas enters the nozzle, its composition does not change.
11. The burning rate is uniform in any given section normal to the motor axis.
12. The nozzle throat erosion is negligible.

Some of these assumptions will be recalled in the following sections. The justification of assumptions 1-10 is developed in reference [53]. The reader is encouraged to revise it for further clarification. The justification of assumption 11 is derived from assumption 9: the burning rate is directly dependant on pressure and the propellant composition, variables assumed to be homogeneous through out the cross section. Finally, assumption 12 justification is based on the very short combustion times expected in ACUS prototypes, and the operating characteristics of the motor. Nozzle erosion is an important threat to performance, mostly in hybrid rockets, due to the high content of oxidizing agents in the gas [54][55] (i.e., hybrid rocket motors may present up to 3 times more erosion in the throat area than similar SRM [56]). Due to the very short combustion time, and the propellant used, little decrease in performance is expected by means of this issue.

3.4.2 Building the Model

Model definition starts by recalling the equation for the thrust, Equation 2.1. Exit variables (i.e., velocity and pressure) are quite affected by the nozzle, located at the exit of the rocket motor. It seems useful to study how the flow behaves through it, being the nozzle the key component (apart from the grain) of a rocket motor. A good understanding of the physics underlying it is necessary.

The flow through the nozzle is compressible, ideal, and one-dimensional (i.e., directed along the nozzle axis). Isentropic flow condition is imposed: it is frictionless (negligible wall friction, boundary layer effects, etc), and adiabatic (no heat losses). This strict condition means that the properties of the flow only change as the nozzle cross sectional area changes. Note, however, that any flow disturbance, manufacturing defect, or frictional conditions will perturb the flow, leaving the isentropic condition. Those effects are considered to be negligible.

As the flow is adiabatic, there is conservation of energy. The energy equation between two points 1 and 2 of the nozzle stands as Equation 3.2,

$$h_1 - h_2 = C_p \left(T_1 - T_2\right) = \frac{v_2^2 - v_1^2}{2} \tag{3.2}$$

where h is the enthalpy of the gas, C_p is the effective heat capacity of the gas, T_i is the temperature at location i, and v_i is the gas velocity at that location. The equality at the right hand side shows how the change in internal energy (temperature change) is reflected as an increase in kinetic energy.

On the other hand, it is useful to relate important thermodynamic variables, such as the pressure P and the density ρ, over referenced values. Those referenced values are the stagnation states of such variables, being reached when the fluid were decelerated to absolute zero velocity (i.e., isentropically). It is well-known [53], that one can relate the pressure and the density with their stagnation values, through Equation 3.3 and Equation 3.4:

$$\frac{P_0}{P} = \left(1 + \frac{\gamma - 1}{2} M^2\right)^{\frac{\gamma}{\gamma - 1}} \tag{3.3}$$

$$\frac{\rho_0}{\rho} = \left(1 + \frac{\gamma - 1}{2} M^2\right)^{\frac{\gamma}{\gamma - 1}} \tag{3.4}$$

where *M* is the Mach Number (i.e., $M = v/a$), γ is the ratio of specific heats, $\gamma = C_p/C_v$. P and ρ are the pressure and density at any location of the flow, and P_0 and ρ_0 are the

stagnation values of such variables. As it is assumed that the flow velocity immediately upstream the nozzle (combustion chamber) is zero, T_0 is the combustion temperature, and P_0 is the combustion chamber pressure, P_c.

The second equation of interest in any compressible flow analysis is the continuity equation. Let us write it as

$$\rho A v = \rho^* A^* v^* \tag{3.5}$$

where *A* is the cross sectional area at a given nozzle location. The asterisk of the right-hand side variables means that the location is 'critical'; the Mach number there is equal to unity. It can be shown that a relation between A and A^*, that only depends on the Mach number M, exists:

$$\frac{A}{A^*} = \frac{1}{M}\left(\frac{1+\frac{\gamma-1}{2}M^2}{1+\frac{\gamma-1}{2}}\right)^{\frac{\gamma+1}{2(\gamma-1)}} \tag{3.6}$$

This equation shows that, for the flow to become supersonic through a nozzle, there must be a section of minimum area, and consequently, a converging-diverging shape. At the section of minimum area (the throat), the flow is sonic, $M = 1$.

On the other hand, the exit velocity can be derived recalling that the stagnation enthalpy (and all stagnation properties) is constant,

$$h_0 = h + \frac{v^2}{2} \tag{3.7}$$

Thus,

$$v_e = \sqrt{2\left(h_1 - h_e\right) + v_1^2} \tag{3.8}$$

where the subscript 1 refers to the nozzle entry, and the subscript e to the nozzle exit. Using general thermodynamic relations and the energy and continuity equations, and

after some manipulation, Equation 3.9 for the exit velocity can be reached.

$$V_e = \sqrt{2T_0 \left(\frac{R}{M}\right) \left(\frac{\gamma}{\gamma - 1}\right) \left[1 - \left(\frac{P_e}{P_0}\right)^{\frac{\gamma-1}{\gamma}}\right]} \tag{3.9}$$

where R is the universal gas constant, and M is the molecular weight of the combustion products. If P_e is assumed to be equal to the ambient pressure (P_{amb}), the nozzle is said to be matched (optimal thrust condition). In general, this condition is only achieved during an specific operating point, for non-variable geometry nozzles.

Coming back to Equation 2.1, one may employ continuity through the nozzle to evaluate the mass flow rate $\dot{m}$ at the nozzle throat (i.e., critical section, $M = 1$), and write

$$F = \rho^* A^* v^* V_e + (P_e - P_a) A_e \tag{3.10}$$

Using the properties at the throat, and employing Equation 3.9, one can transform Equation 3.10 into Equation 3.11,

$$F = A^* P_0 \sqrt{\frac{2\gamma^2}{\gamma - 1} \left(\frac{2}{\gamma + 1}\right)^{\frac{\gamma+1}{\gamma-1}} \left[1 - \left(\frac{P_e}{P_0}\right)^{\frac{\gamma-1}{\gamma}}\right]} + (P_e - P_a) A_e \tag{3.11}$$

Equation 3.11 is a fundamental result: it shows that the thrust that a rocket motor can provide is a function of the exit pressure, the nozzle throat area, and the combustion chamber pressure. The exit pressure, P_e, can be inferred from an expression for the ratio A^*/A_e (i.e., expansion ratio), that it can be shown to be:

$$\frac{A^*}{A_e} = \left(\frac{\gamma + 1}{2}\right)^{\frac{1}{\gamma-1}} \left(\frac{P_e}{P_0}\right)^{\frac{1}{\gamma}} \sqrt{\left(\frac{\gamma + 1}{\gamma - 1}\right) \left[1 - \left(\frac{P_e}{P_0}\right)^{\frac{\gamma-1}{\gamma}}\right]} \tag{3.12}$$

where the nozzle exit pressure P_e is obtained from the chamber pressure P_0, given the nozzle area expansion ratio A^*/A_e. If P_e = P_0, the expansion is optimal. One may find the optimal expansion ratio A^*/A_e, for that condition. However, the exit pressure varies

along the motor operation, as it is a function of the chamber pressure. Assuming that the ratio A^*/A_e is constant (constant nozzle geometry), the nozzle can be optimized only for an specific operating point.

Based on this analysis, it is found that the combustion chamber pressure, P_c, is the key term in Equation 3.11 driving a change in thrust (as P_e is ultimately dependant on it). For that reason, a law that governs the pressure evolution needs to be found, to complete the performance model. Such analysis starts by noting that the mass flow rate of gas through the nozzle must be equal to the rate at which the solid propellant consumes itself:

$$\dot{m}_g = A_b \rho_p r \tag{3.13}$$

where A_b is the burning area (a function of time), ρ_p is the propellant density, and r is the burning rate, or the rate at which the flame front consumes the propellant. From continuity, the propellant mass burned must be equal to the sum of, the change in gas mass in the combustion chamber, and the mass flowing out through the nozzle (per unit time) [57]. This conclusion is expressed as:

$$\underbrace{\dot{m}_g}_{\text{Propellant mass burned}} = \underbrace{\frac{dM_g}{dt}}_{\text{Change in gas mass in chamber}} + \underbrace{\dot{m}_n}_{\text{mass flow rate through nozzle}} \tag{3.14}$$

The term $\dot{m}_n$, evaluated at the **choked** (i.e., critical) nozzle throat, can be written as

$$\dot{m}_n = \rho_t v_t A_t \tag{3.15}$$

Recalling Equation 3.4, with $\rho_0 = P_0/RT_0$, and that the gas velocity at the throat is equal to the sonic speed,

$$v_t = \sqrt{\frac{2\gamma}{\gamma+1} RT_0} \tag{3.16}$$

Equation 3.15 can be, therefore, rewritten as

$$\dot{m_n} = P_0 A_t \sqrt{\frac{\gamma}{RT_0}\left(\frac{2}{\gamma+1}\right)^{\frac{\gamma+1}{\gamma-1}}} \tag{3.17}$$

On the other hand, the term $\frac{dM_g}{dt}$ is simply

$$\frac{dM_g}{dt} = \frac{d(\rho_0 v_0)}{dt} = \rho_0 A_b r + v_0 \frac{d\rho_0}{dt} \tag{3.18}$$

where v_0 is the instantaneous gas volume in the combustion chamber. Writing all these results in Equation 3.14 yields,

$$\dot{m_g} = A_b \rho_p r = \rho_0 A_b r + v_0 \frac{d\rho_0}{dt} + P_0 A_t \sqrt{\frac{\gamma}{RT_0}\left(\frac{2}{\gamma+1}\right)^{\frac{\gamma+1}{\gamma-1}}} \tag{3.19}$$

Using the ideal gas law,

$$A_b \rho_p r = \frac{P_0}{RT_0} A_b r + v_0 \frac{1}{RT_0}\frac{dP_0}{dt} + P_0 A_t \sqrt{\frac{\gamma}{RT_0}\left(\frac{2}{\gamma+1}\right)^{\frac{\gamma+1}{\gamma-1}}} \tag{3.20}$$

Note that we are approaching what seems to be a differential equation for the pressure at the combustion chamber, P_0. Once this law is found, the model is closed, as it can be coupled with Equation 3.11, to obtain both the pressure and thrust curves. Still, there are two terms in Equation 3.20 which are not developed yet: The burning rate r, and the burning area, A_b. In this model, in which only grains with a central cylindrical port are considered, the instantaneous burning area is, simply, the inner face of the grain, as Figure 3.3 shows. Regarding the burning rate, this variable requires a more in deep analysis, which is presented in the next section.

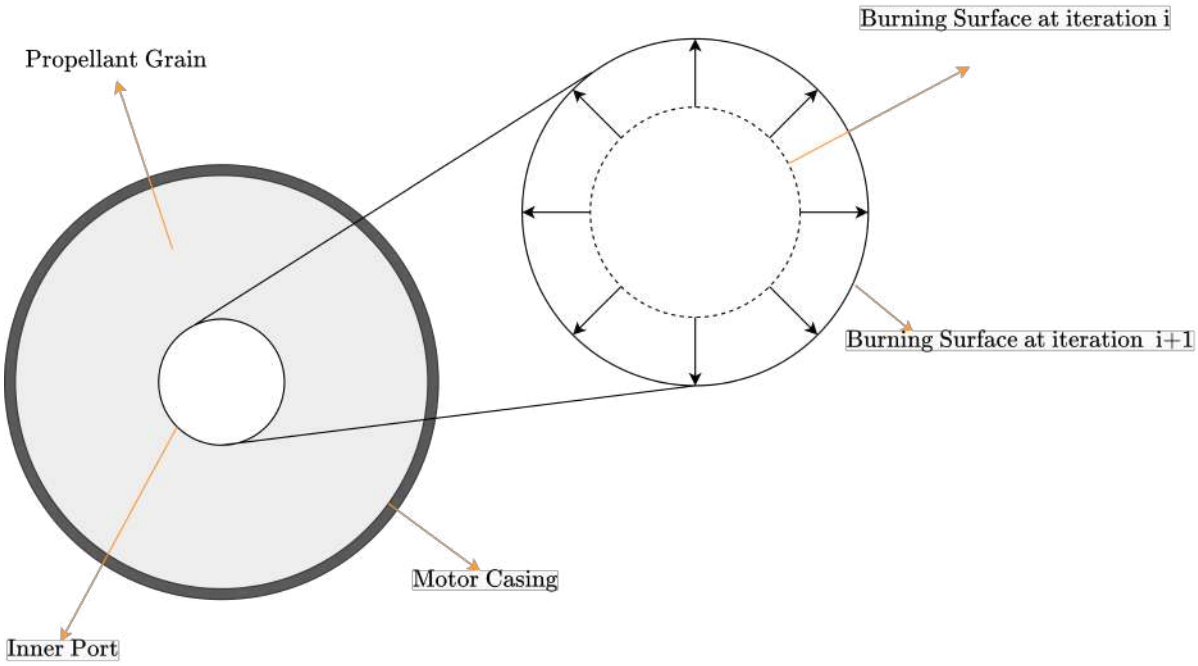

Figure 3.3: Cross sectional area of the grain. The figure shows the burning surface regression between two instants of time, i and $i+1$.

3.4.3 Burning Rate

The Burning Rate of a propellant, denoted by *r*, is a measure of how fast a given propellant is being consumed. As previously seen, it is a variable that posses a significant impact on the performance of a rocket motor, due to the dependency in Equation 3.20. A proper modeling of this variable is fundamental for a proper prediction of rocket motor performance. It is generally accepted that a simplified, or nominal version of the burning rate, is given by Vielle's[iv] Law, or Saint Robert's Law,

$$r_0 = r_{00} + aP_0^n \tag{3.21}$$

[iv] Vieille, among other works, also discovered the nitrocellulose-based smokeless gunpowder in 1884.

where r_0 is the *nominal* burning rate (typically expressed in mm/s), a is the burn rate coefficient, n is pressure exponential factor, r_{00} is a constant, that usually takes null value, and P_0 is the chamber pressure, typically expressed in MPa. Constants a and n do not follow any analytical law and need to be empirically determined, by testing the propellant in strand burners. In the case of the exponential factor n, it takes a value smaller than 1 for all operative propellants. Otherwise, small pressure fluctuations may lead to uncontrol pressure rise [28]. The term r_0 is clearly dominated by pressure, but it is independent of any other gas thermodynamic variable.

This expression, however, is only *approximately* met by many propellants [57]. As the reader may intuitively suspect, the burning rate is affected by other phenomena, that are hereafter considered. The two main effects that will be added to Equation 3.21 are the sensitivity to ambient temperature, and the erosive burning influence.

Temperature sensitivity is a parameter of relevance in solid propellant rockets [58]. The lower this sensitivity, the more stable and predictable is the rocket performance. However, it is often not studied as much as the control of the pressure exponent n [58].

This sensitivity analysis begins by studying how is the burning rate affected by the combustion characteristics of a double base propellant. It is widely accepted [59][58][60] that the combustion wave of such propellants is divided in two main phases: the Condensed Phase and the Gas Phase. These are shown in Figure 3.4 (adapted from [58]). At the condensed phase, two reactions are important: the subsurface, and the surface reactions. On the other hand, the Gas Phase presents three regions: the Fizz, Dark, and Luminous Flame zones.

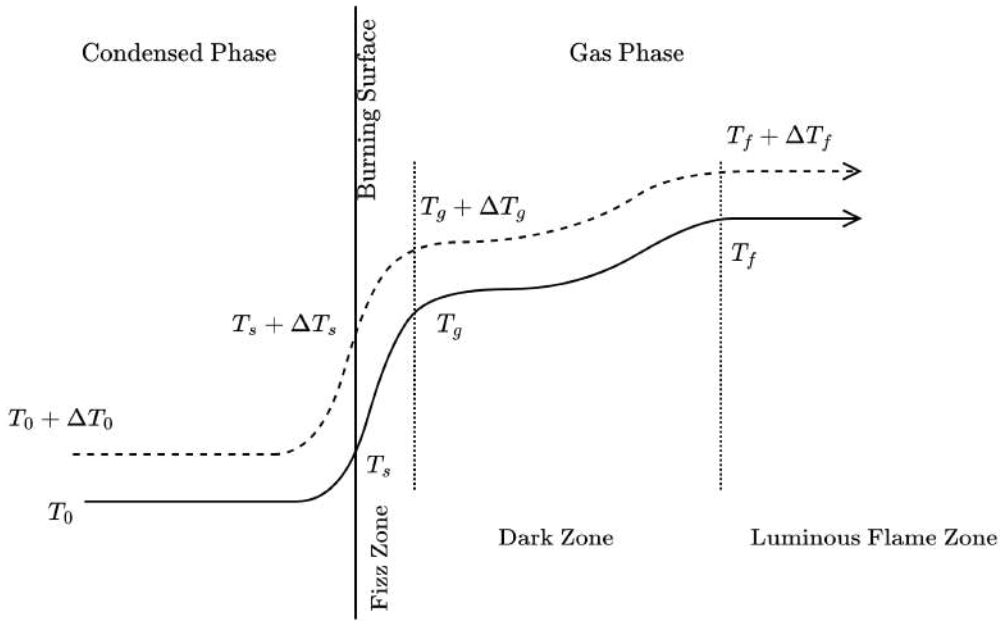

Figure 3.4: Schematic of combustion zones for a double base propellant. Three distinct zones are observed: A small layer close to the Burning surface (Fizz Zone), an Induction Zone (Dark Zone), and a Secondary Flame (Luminous). At each layer, different combustion products and components are being created, leading to complex interactions between them. ΔT_0 represents an initial temperature variation.

The fizz zone is also known as primary flame [60], while the luminous flame is also named as secondary. The Burning Rate r is controlled by the heat feedback mechanism between the burning surface and the fizz zone [58]. In contrast, both, the dark and luminous zones, are not important in determining the burning rate [61][60][v]. Consequently, that heat feedback mechanism is the key to determine the temperature sensitivity of the burning rate.

The temperature sensitivity can be defined, on a first approach [62], as the change of

[v] In the pressure range up to 100 atm, the secondary flame (luminous) does not even affect the temperature gradient in the fizz zone [60]

the burning rate with the initial temperature variation at constant pressure:

$$\sigma_p = \frac{r_1 - r_0}{r(T_1 - T_0)} \tag{3.22}$$

where σ_p is the temperature sensitivity, and r_1 and r_0 are burning rates at T_1 and T_0 respectively. This equation is expressed, in a more rigorous way, by writing it in differential form [62].

$$\sigma_p = \left(\frac{\partial lnr}{\partial T_0}\right)_p \tag{3.23}$$

Alternatively, the temperature sensitivity can be also derived using the heat feedback from the gas, to the condensed phase of the propellant. The result expresses σ_p as a function of the activation energy of the reaction in the fizz zone. The interested reader may refer to reference [58] for a complete derivation of this equation.

Typically, the burning rate is measured in Strand Burners, and Microthermocouples and other thermally sensitive sensors are used to measure temperature profiles. In particular, surface temperature is typically analyzed using optical and thermocouple techniques [63][64]. The propellant is subjected to different ambient conditions, the burning rate measured, and the difference with respect to nominal conditions determined.

The second effect that may affect the nominal Burning Rate is the erosive burning effect. Erosive burning is a phenomenon that enhances the burning, due to the high velocity flow of combustion products over the burning propellant. Those high velocity gases, together with the effect of turbulent boundary layer mixing, enhance the heat transfer mechanisms to the burning surface, increasing the rate at which the flame front consumes the propellant. The burning rate at those areas is increased [65], leading to pressure and thrust enhancement; such pressure rise is quite significant [66], and needs to be studied. Otherwise, it may result in fatal failure due to an overpressure, or in an incorrect and unexpected performance.

The effect of erosive burning is more critical in rocket motors where the port area is small, or when the length to diameter ratio is higher (as this leads to higher port velocity, at the end of the grain [65]). In these situations, SRM performance prediction becomes difficult, and it is fundamental to include such effect in the performance model. Due to the complexity of the processes involved in erosive burning (with influence of pressure, port mass flux, nature of binder and oxidizer, motor geometry, etc [67]), most of the models employed to predict it are based on empirical laws. Two of the most important ones are reviewed here.

The Mukunda - Paul model, developed in 1997 [67], presented a correlation between η (ratio of the actual to non-erosive burn rate) and g, which is a product of a quantity g_0 (the ratio of the free stream mass flux, to the mass flux from the surface, for the non-erosive condition), and $Re_0^{-0.125}$, where Re_0 is the Reynolds number based on the propellant non-erosive mass flux, and on the port diameter. This correlation was developed considering available data, using a simple non-dimensional relationship. Apart from the excellent correlation with existing data, which allows to use this model for practically all used propellants, it is expressed in non-dimensional form, unlikely other models, such as the Lenoir-Robillard [68]. The Mukunda - Paul universal expression for the erosive burning ratio is expressed as

$$\eta = \frac{r_e}{r_{ne}} = 1 + 0.023 \left[g^{0.8} - g_{th}^{0.8} \right] \mathcal{H} \left(g - g_{th} \right) \tag{3.24}$$

where r_e is the erosive burning rate, r_{ne} is the non-erosive burning rate, $g_{th} = 35$, $\mathcal{H}$ is the Heaviside unit step function, and $g_0 = G/\rho_p r_{ne}$, with G being the mass flux through the port, and ρ_p the propellant density. Moreover,

$$g = g_0 \left[(Re_0/1000)^{-0.125} \right] \tag{3.25}$$

$$Re_0 = \frac{\rho_p r_{ne} D_h}{\mu_g} \tag{3.26}$$

where μ_0 is the gas phase viscosity, and D_h is the hydraulic diameter. This expression was reached after fitting the model with burning data of double-base, composites, and varying energy level propellants [67]. The accuracy of such fitting is within $\pm 10\%$.

The second model of interest is the Lenoir and Robillard Model [69], developed in 1956, and widely used in rocket motor performance predictions, due to its relative simplicity. Based on the postulate that the erosive component of the burning rate is proportional to the heat-transfer rate from the core of the combustion gases stream to the propellant walls [69], this model states that the actual burning rate of a propellant (i.e., with the erosive burning effect) r_e, is equal to the addition of the 'nominal' burning rate r_{ne}, and a new factor r_{new}:

$$r_e = r_0 + r_{new} = aP^n + \alpha G^{0.8} D_h^{-0.2} \exp\left(-\beta r_e \rho_b / G\right) \tag{3.27}$$

Here, the constants α and β are empirically determined. β is found to be independent of the propellant formulation, taking a value of 53, while α is found from

$$\alpha = \frac{0.0288 c_p \mu^{0.2} \mathrm{Pr}^{-2/3}}{\rho_b c_s} \cdot \frac{T_f - T_s}{T_s - T_p} \tag{3.28}$$

where T_f is the flame temperature, T_p is the ambient temperature, T_s is the burning surface temperature, μ is the gas phase viscosity, Pr is the gas phase Prandtl Number, ρ_p is the density of the solid propellant, and c_s is the specific heat of the solid propellant.

The model that is selected for the motor simulator is the Mukunda - Paul one, a decision based on its excellent correlation with a wide variety of experimental measurements, from different propellant types, and due to its easier numerical implementation in the simulator scheme.

3.4.4 Solving the model

The complete model is now closed. One can write:

$$A_b \rho_p r_e = \frac{P_0}{RT_0} A_b r_e + v_0 \frac{1}{RT_0} \frac{dP_0}{dt} + P_0 A_t \sqrt{\frac{\gamma}{RT_0} \left(\frac{2}{\gamma+1} \right)^{\frac{\gamma+1}{\gamma-1}}} \tag{3.29}$$

with

$$r_e = r_{ne} \cdot \eta \cdot \sigma_p \cdot \Delta_T \tag{3.30}$$

where r_{ne} is given by Equation 3.21, η is given by Equation 3.24, σ_p is the temperature sensitivity, and Δ_T is the initial temperature variation (with respect to the nominal one).

Every iteration, the burning area increases due to the burn rate r_e. Consequently, in every computation step i, the burning area is updated considering the burning rate from step $i-1$, which is computed using Equation 3.30. Once A_b is updated through a simple geometric analysis[vi], P_0 at step i can be computed using Equation 3.29. P_e is computed using Equation 3.12. Lastly, the thrust at each iteration can be computed recalling Equation 3.11.

This iterative procedure is valid until the propellant is consumed. At that moment, there is a tail-down phase, which is modelled by setting $A_b = 0$ in Equation 3.29. The differential equation for the Pressure is now independent of the burning rate (there is no propellant to be burned, ideally), and one can write

$$\frac{v_0}{RT_0} \frac{dP_0}{dt} = -\frac{\mathrm{P}_0 A_t}{\mathrm{c}^*} \tag{3.31}$$

[vi] taking into account that this work is restricted to cylindrical internal geometries. A more complex geometry would required in-deep burnback analysis.

with

$$c^* = \sqrt{\frac{RT_0}{\gamma\left(\frac{2}{\gamma+1}\right)^{\frac{\gamma+1}{\gamma-1}}}} \tag{3.32}$$

Solving it, the evolution of the pressure is easily determined:

$$P_c = P_{max}\exp\left(\frac{-RT_0A_t}{v_0c^*}t\right) \tag{3.33}$$

where P_{max} is the maximum pressure experienced during the combustion, at the moment where the propellant is completely depleted, and t is the time measured from that burn-out.

3.4.5 Model Validation

Before this quasi steady one-dimensional model is accepted for rocket motor design, it must be validated against literature or other, available, internal ballistics models. Despite the simplicity of the present model, it should be able to represent, in a reliable way, the general and most important characteristics of the motor performance.

The validation is divided in two parts. The first deals with the model without the erosive contribution, using internal ballistics numerical models from Stekhareh et.al [70] and Irisarri [71]. The second validation checks the model with the erosive contribution, on the one hand, with experimental data from NAWC (US Naval Air Warfare Center) tactical motor nº 13 [72][73][74], and the SPINBALL analytical model from Cavallini [75], and on the other hand, with an internal ballistics model from Greatrix [76].

The first validation, as remarked before, confronts the model without the erosive contribution. For that purpose, a motor with dimensions described in Table 3.3 [70][71] is simulated using the developed code. A simple cylindrical internal geometry is employed. Propellant characteristics are listed in Table 3.4.

Table 3.3: Motor geometrical features, first validation

Characteristic	Value
Motor length	0.7080 m
Inner port diameter	0.0254 m
Casing diameter	0.0635 m
Nozzle diameter	0.0235 m

Table 3.4: Propellant Characteristics, first validation

Characteristic	Value
Gas heat capacity ratio	1.21
Propellant density	1742 kg/m^3
Adiabatic flame temperature	3056 K
Vieille's law *a* coefficient	$4.092 \cdot 10^{-5} m/s$
Vieille's law *n* coefficient	0.36
Propellant gas phase viscosity	$8.19 \cdot 10^{-5} kg/m \cdot K$

Figure 3.5 shows the numerical results from the model developed in this work, excluding the erosive contribution, compared with results from Stekhareh [70] and Irisarri [71] (2P2-ODIB Model), using the motor and propellants described in Table 3.3 and Table 3.4.

These results show that the developed model (i.e., black line in Figure 3.5) is able to describe the most important features of the motor performance, such as the pressure peak after ignition and burn-out. It seems, however, that the model slightly underestimates such peak, when compared to literature models. Nevertheless, the burning time and the slope of the pressure curve are in agreement. In particular, the closest agreement is with the quasi-steady one-dimensional 2P2-ODIB Model, which includes, among other features, nozzle erosion.

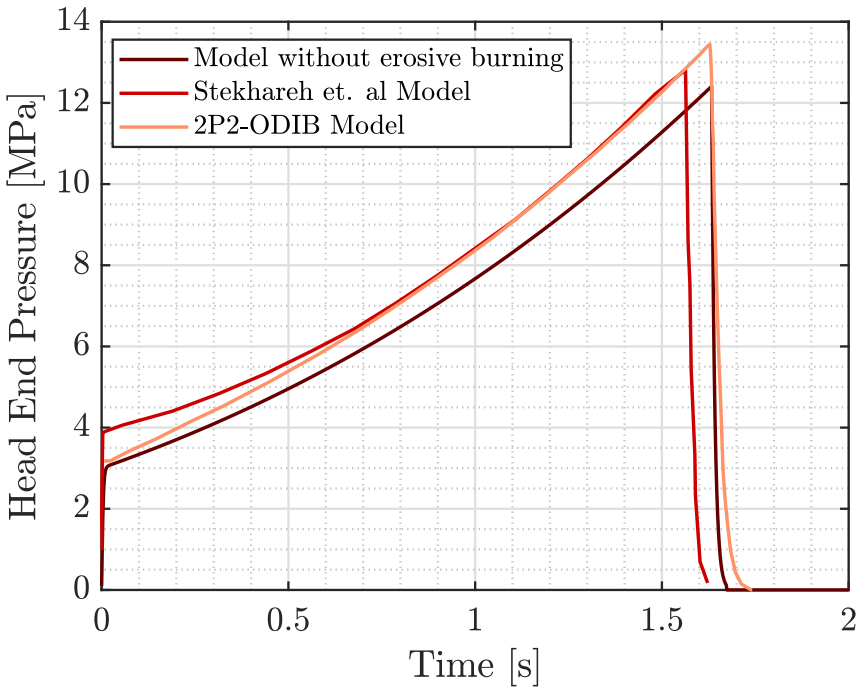

Figure 3.5: Validation of the non-erosive model with results from Stekhareh [70] and Irisarri [71].

The second validation aims to confirm the capacity of the proposed model, coupled with the erosive burning contribution, to predict, with robustness, the motor performance. This validation is of the outmost importance as these effects are of interest in rocket motors of high L/d_0 ratio, which are specially suitable for the application under study (weaponry onboard RPAS).

Table 3.5: Motor geometrical features, second validation

Characteristic	Value
Motor length	84 cm
Inner port diameter	2.1 cm
Casing diameter	6.35 cm
Nozzle diameter	2.03 cm

For that purpose, two different analysis are to be done. Firstly, the model is compared

with results by Greatrix [76]. The dimensions of the motor, and the propellant characteristics, are listed in Table 3.7 and Table 3.8. The internal grain geometry is, again, cylindrical. Due to the design L/d_0, erosive effects are expected to be important (in the form of accelerated burning and important pressure peaks, mainly at the initial moments of operation). Figure 3.6 shows the comparison between the model and the results by Greatrix.

Table 3.6: Propellant Characteristics, second validation

Characteristic	Value
Gas heat capacity ratio	1.21
Propellant density	1740 kg/m^3
Adiabatic flame temperature	3060 K
Vieille's law *a* coefficient	$0.05\ cm/s\ (kPa)^n$
Vieille's law *n* coefficient	0.33
Propellant gas phase viscosity	$8.8 \cdot 10^{-5}\ kg/m \cdot K$

This model describes, with certain accuracy, general performance characteristics, including the pressure curve slope during the non-erosive burning regime. The initial erosive burning pressure peak is correctly modelled, as well as the burn-out moment. On the other hand, initial, and maximum pressure peaks, are overestimated. This is, in principle, a conservative approach, as the motors will be always designed to stand up against a pressure greater than the nominal one. The simplified model also fails to model the tail-off of the pressure curve, leading to reduced burning times, with differences with respect to Greatrix of almost 0.5 seconds. This overestimation was expected, considering that this model does not include losses related to friction, nozzle erosion, or other aspects.

The second validation of the model with the erosive contribution is done using experimental data of NAWC (US Naval Air Warfare Center) tactical motor nº 13 [72][73][74],

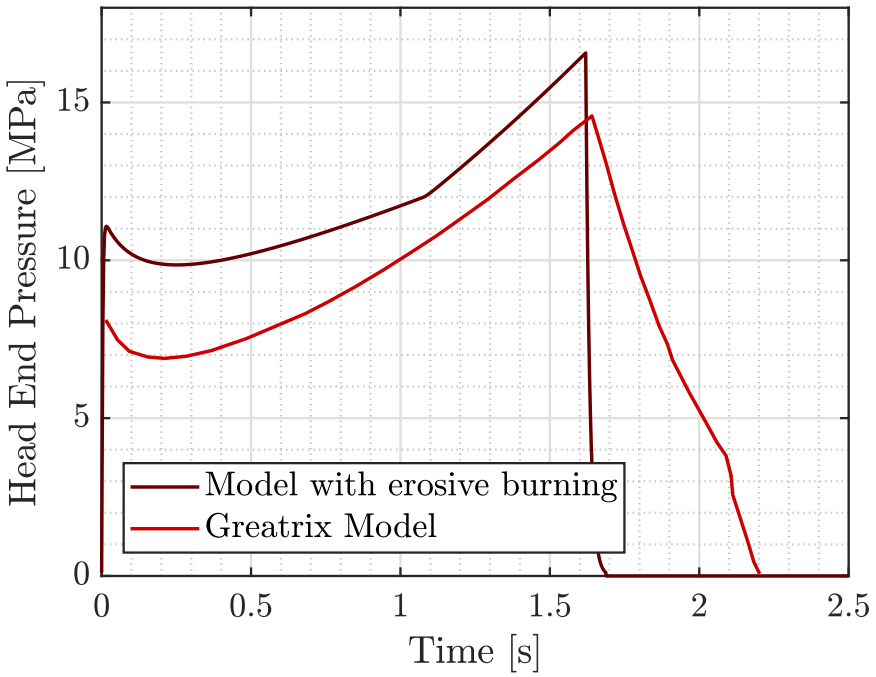

Figure 3.6: Validation of the erosive model with results from Greatrix [76].

and the SPINBALL analytical model from Cavallini [75]. Motor and Propellant Characteristics are defined in the next tables. The propellant is the NWR11b, a composite propellant with 11.9% HTPB, 83% AP, 5% Oxamide, and 0.1% carbon black.

Table 3.7: Motor geometrical features, third validation

Characteristic	Value
Motor length	86 cm
Inner port diameter	7.62 cm
Casing diameter	12.192 cm
Nozzle diameter	2.641 cm

Table 3.8: Propellant Characteristics, third validation

Characteristic	Value
Gas heat capacity ratio	1.2144
Propellant density	1702 kg/m^3
Adiabatic flame temperature	2653 K
Vieille's law *a* coefficient	$0.0796\ cm/s\ (kPa)^n$
Vieille's law *n* coefficient	0.461
Propellant gas phase viscosity	$8.8 \cdot 10^{-5}\ kg/mK$

Figure 3.7 shows the comparison of results. The model successfully represents the first pressure peak in magnitude, but overestimating the second peak, again due to the absence of losses estimation in the code. It fails to represent the ignition transient and the tail-off. While propellant burn-out is, again, well modelled, total burning time is underestimated due to the simplified tail-off implementation. A translation of the numerical simulation should be done in order to account for that ignition transient. The global behaviour of the motor is well captured, despite the fact the the pressure rise slope is overestimated (leading to reduced burning times).

An interesting comment can be done on the pressure spike appearing at the end of the ignition transient. As remarked by Cavallini [75], that pressure spike may be due two effects: The so-called bulk-mode instability (combination of pressure oscillations with dynamic burning effects) [77][78], or the erosive burning of the grain propellant due to the igniter, combined with the igniter tail-off [73][79]. A correct modelling of this phenomena would involve a dynamic burning model, together with ignition transient modelling, features completely outside the scope of this work. Consequently, the matching in the pressure experienced in that first peak between the experimental results and the model is not because of a correct modelling by the model, but due to an overestimation.

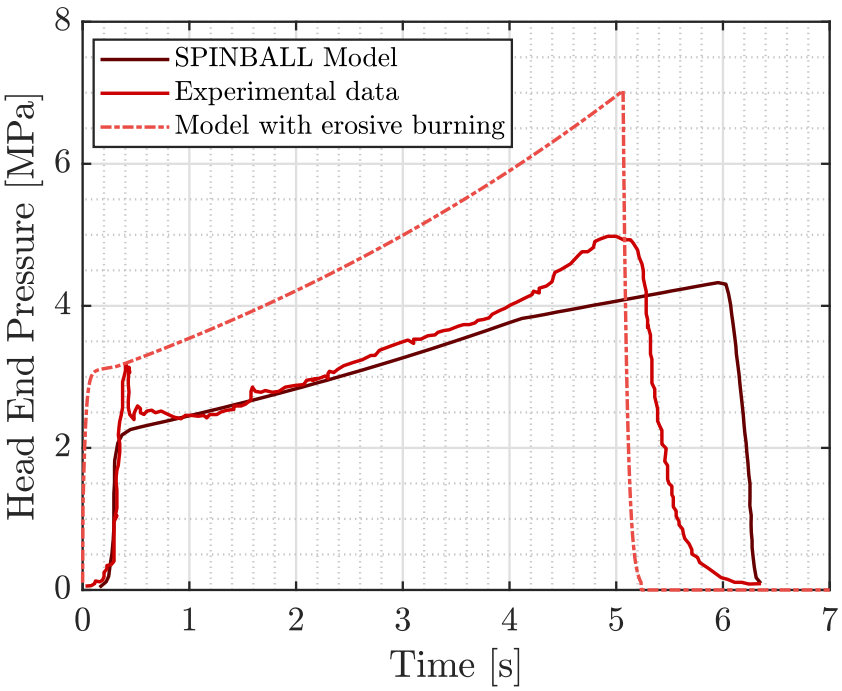

Figure 3.7: Validation of the erosive model with results from Spinball Model, and NAWC Data[76].

These validations show that the model is capable of predicting with enough accuracy the principal performance figures of a solid rocket motor, and that it is a tool that can be used for preliminary motor design.

3.5 Design Constraints

There is a series of constraints that affect this stage design. Some of them are due to manufacturing limits, while others are based on operational requirements. These are listed next.

- **Operational constraints.**
  - Total burning time must be lower than 1 second.

  - Total impulse of the stage must be superior to 100 $N \cdot s$, considering an initial stage velocity of 5 m/s, a final one of 150 m/s and a total missile mass of 0.5 kg.

  - The maximum thrust of the stage must be superior to 150 N.

- **Manufacturing Constraints.**

  - The minimum throat area is 4 mm, from manufacturing limits on the graphite.

  - The inner geometry of the propellant grain is limited to cylindrical shapes, with minimum diameter of 5 mm.

  - The maximum external diameter of the propellant grain is 20 mm.

  - The maximum length of the propellant grain is 150 mm.

That means that certain degrees of freedom of the performance model developed in the previous section have lower or upper bounds, described in Table 3.9, together with their numerical values.

Table 3.9: Constraints on degrees of freedom.

Variable	Value [mm]
Max. external grain diameter (D)	20
Min. internal grain diameter (d_0)	5
Max. grain length (L)	150
Min. nozzle throat diameter (d_t)	4

Apart from these constraints, the number of grains is set to 1 (i.e., $m = 1$), for simplicity.

3.6 Parametric Analysis

Motor performance is now explored through a parametric analysis, using as variables the degrees of freedom which are free. In particular, this section focuses in an analysis of a motor configuration which provides the stage with sufficient thrust and total impulse, and with a sufficient safety factor.

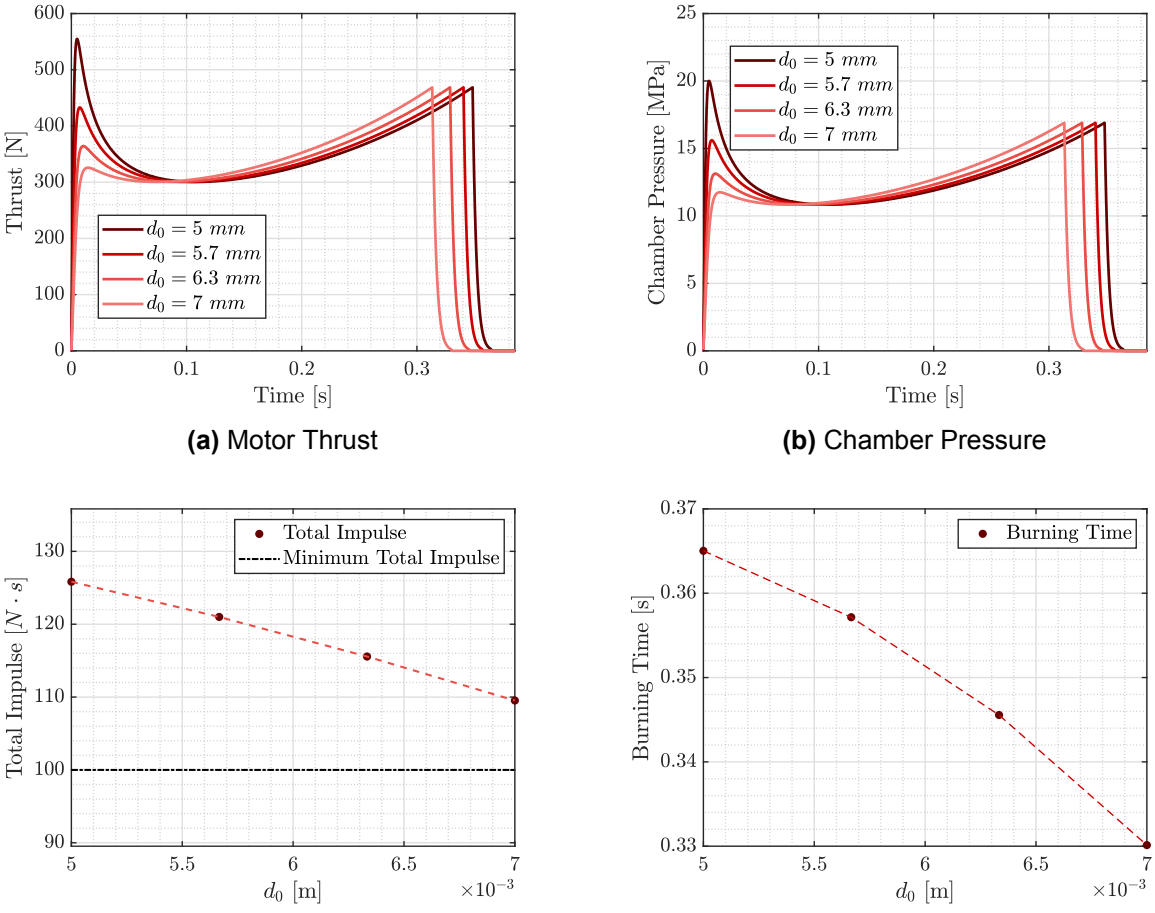

(a) Motor Thrust

(b) Chamber Pressure

(c) Total Impulse

(d) Burning Time

Figure 3.8: Parametric analysis for fixed L and nozzle expansion ratio, for various d_0.

Figure 3.8 shows the parametric analysis that studies the influence of d_0 on the motor performance, for L=150 mm, d_t=4 mm, d_e=12 mm (i.e., exit nozzle diameter), and

D=14.5 mm.

Figure 3.8a depicts that the maximum thrust is not remarkably affected by such port variation. Instead, the thrust curve is displaced towards the right for decreasing port diameters, as there is more propellant web to be burned. Moreover, the erosive burning effect is greater for smaller diameters, as the ratio L/d_0 is more important. Such effect is depicted as an initial thrust and pressure peak, that reduce as d_0 increases. Similarly, the maximum pressure reached within the motor suffers little variation, but the curve itself is displaced towards the right for decreasing port diameters.

That increase of the burning time is shown in Figure 3.8d. The burning time varies, and reduces for higher port diameters, due to the reduction in propellant web. Regarding the Total Impulse, I_T, it is reasonable to predict that the lower the port diameter, the higher that performance variable, as there is more propellant to be burned, during more time, while the maximum thrust developed is the same. That assumption is confirmed by Figure 3.8c, where I_T decreases as d_0 increases. I_T is computed according to

$$I_t = \int_0^{t_t} \mathrm{F(t)}dt \tag{3.34}$$

where F is the thrust as a function of time, and t_t is the final burning time.

Following with the parametric analysis, the influence of the grain length L is now studied, for d_0=6 mm, d_t=4 mm, d_e=12 mm, and D=14.5 mm. Figure 3.9 displays this parametric study. In particular, Figure 3.9a and Figure 3.9b show the thrust and chamber pressure of the motor during operation, for various L.

It is worth noticing that, in contrast with the previous case, maximum thrust and pressure vary noticeably for increasing L/d_0 aspect ratios: while the shape of thrust and pressures curves are similar (due to the internal geometry, which is fixed), the two pressure and thrust peaks increase as L increases. In particular, the erosive burning peak

after ignition increases certainly: there is higher port velocity at the propellant section close to the nozzle, increasing such erosive effect. These results match with revised literature studies [80].

The burning time for each case reduces as L/d_0 increases: while the propellant web remains constant, the chamber pressure increases, together with the erosive effect. Following Equation 3.30, the burning rate increases accordingly. As a consequence, the propellant is consumed in less time. Lastly, I_T increases with L, due to the higher developed thrusts, despite the shorter combustion times.

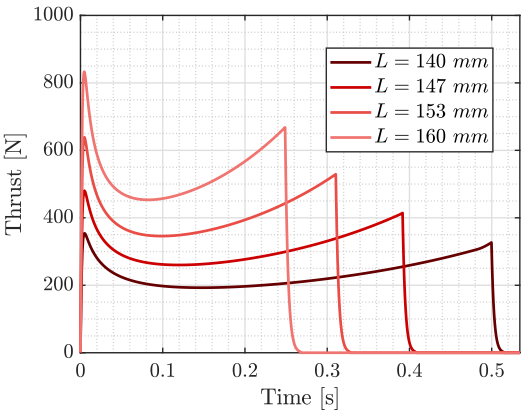

(a) Motor Thrust.

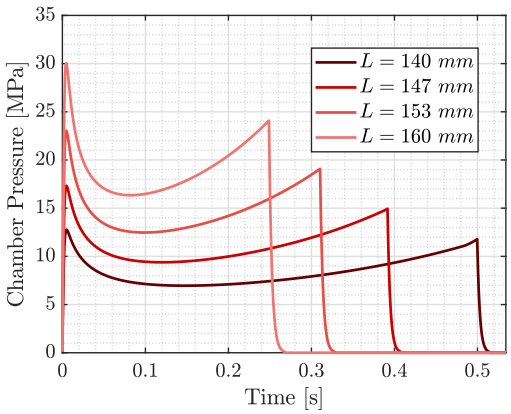

(b) Chamber Pressure.

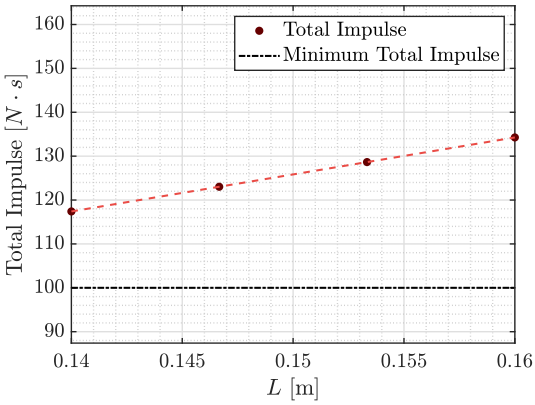

(c) Total Impulse.

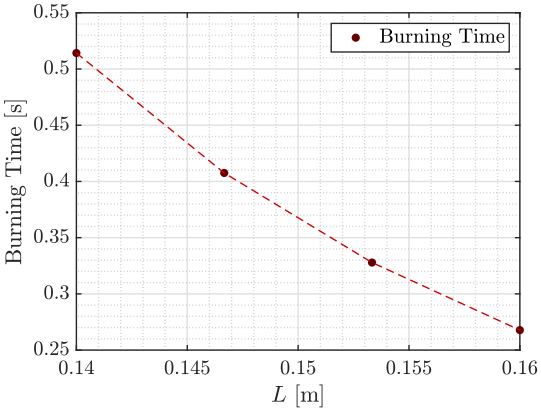

(d) Burning Time.

Figure 3.9: Parametric analysis for fixed d_0 and nozzle expansion ratio, for various L.

Next analysis studies the influence of the nozzle expansion ratio A_e/A_t. It was previously mentioned that there exists an optimal exit area (for a given throat area) for which the exit pressure equals the ambient pressure, leading to optimal performance. It is not possible to optimize the exit area for the whole operation, unless a variable geometry nozzle is employed.

This optimal nozzle expansion ratio increases with P_c. It increases with time, as the chamber pressure increases, and, from Equation 3.12, P_e increases accordingly. Consequently, as the combustion progresses, greater nozzle area ratio would be required to expand the flow until it completely matches the ambient pressure. As the nozzle geometry is fixed during operation, a perfectly matched nozzle will be only possible in a particular operation point. It is convenient to choose this point such that the remaining operation is as less detrimental as possible. In general, a ratio at a mid-operation point will be choose, or at a condition which represents sufficiently the rocket operation. For that reason, the influence of the throat area is analysed, for d_0=6 mm, L=150 mm, D=14.5 mm, and a fixed d_e=12 mm. Figure 3.10 shows this parametric study.

This study shows that A_t is one of the variables showing greatest influence on the rocket performance. As expected, from the performance equations analyzed in Chapter 3, increasing values of A_t lead to lower maximum thrusts and pressures. The erosive character remains similar among all simulations, due to the constant L/d_0, with modest initial peaks after ignitions. Burning times, as shown by Figure 3.10d, increase as A_t increases, due to the higher pressure and, hence, burning rate. The difference is quite notable, with 0.8 s of variation. Lastly, I_t is practically constant for all simulations: despite the variations in the maximum thrust between design options, burning times are also different, and the result of Equation 3.34 outputs very similar values.

The last parametric analysis of interest for the design purposes is the one involving D, the external grain diameter. This variable impacts also the external shape and size of the rocket motor. Given a reference motor (i.e., motor 1), with fixed d_0ref, nozzle

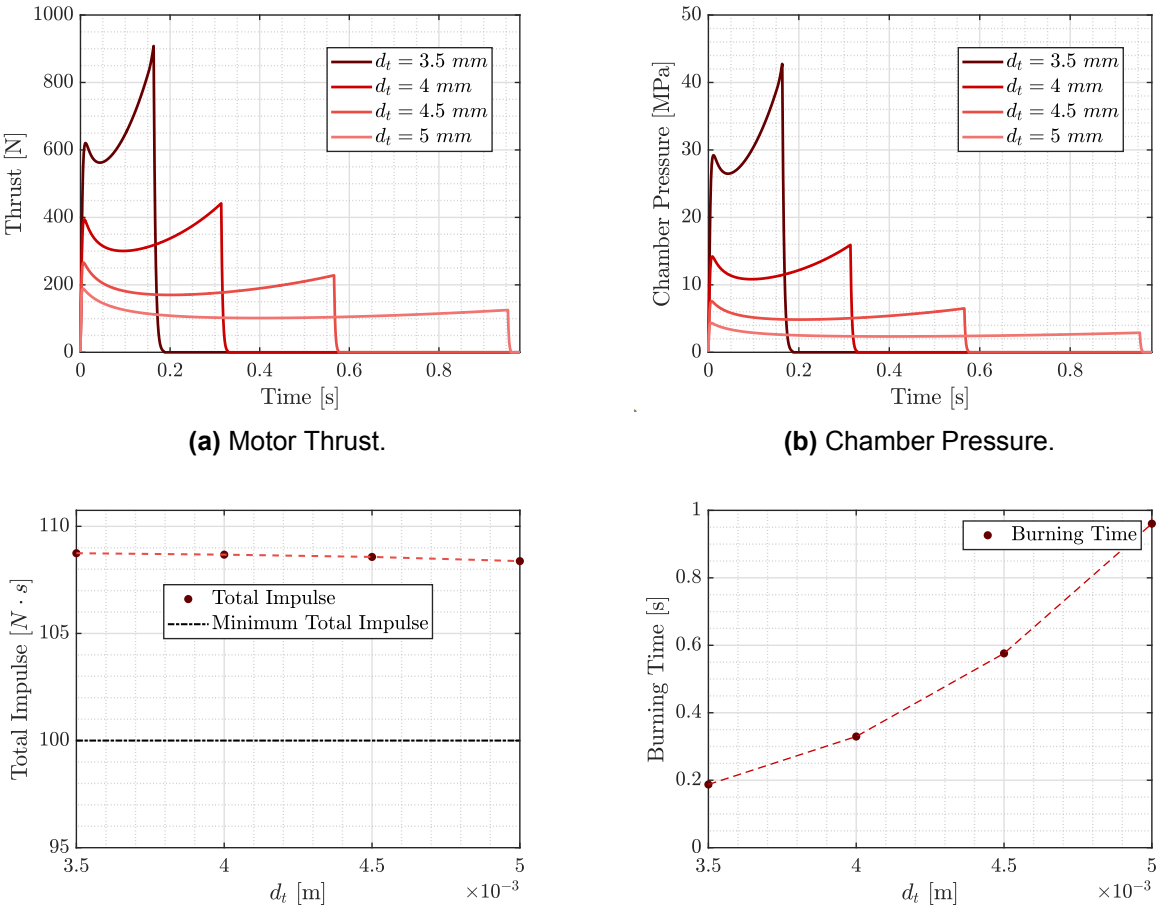

(a) Motor Thrust.

(b) Chamber Pressure.

(c) Total Impulse.

(d) Burning Time.

Figure 3.10: Parametric Analysis for fixed d_0 and L, for various expansion ratios.

geometry, L_{ref} and D_{ref}, if a motor (i.e., motor 2) presents the same geometry characteristics, but a different external grain diameter (e.g., $D > D_{ref}$), then the operation of motor 2 should be exactly as that of motor 1, until the time at which propellant of motor 1 is consumed. At that point, the operation of motor 2 continues towards higher pressures and thrusts. If $D < D_{ref}$, then the operation of motor 2 finishes earlier but, during the burning, the behaviour is equal to that of motor 1.

Figure 3.11 presents, and confirms, this hypothesis. As Figure 3.11a shows, the thrust developed by the motor is the same for all cases, until the smaller ones finish their burning. At that point, the bigger ones continue with the operation. Evidently, due

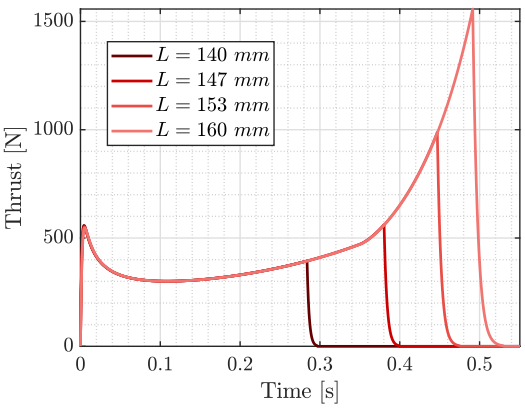

(a) Motor Thrust.

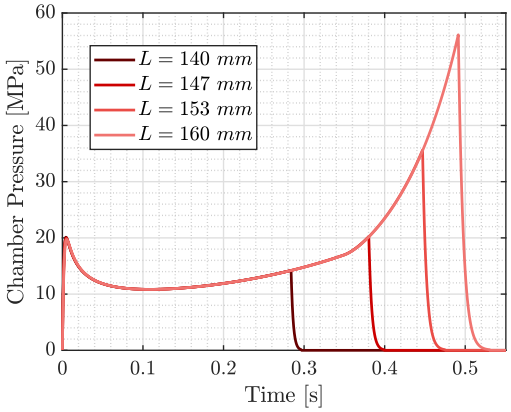

(b) Chamber Pressure.

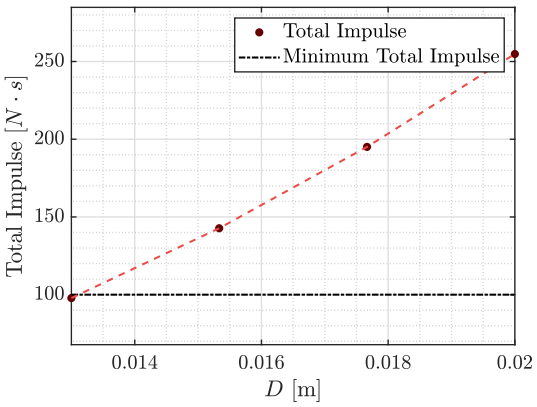

(c) Total Impulse.

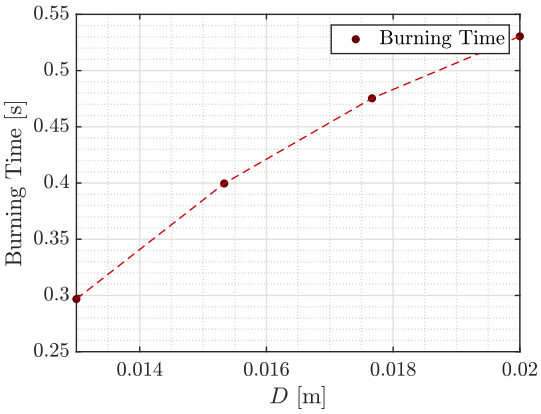

(d) Burning Time.

Figure 3.11: Parametric Analysis for fixed d_0 and L, for various D.

to the higher thrust developed, and the higher burning times (i.e., more propellant is available), higher specific impulses should be expected as D increases. This is confirm by the simulation shown in Figure 3.11c.

3.7 Design Point and expected performance

The parametric analysis highlights that, in general, increasing L, while reducing A_t and d_0, leads to increase performance, but more demanding structural requirements. Specifically, the throat area, A_t, influences, deeply, the motor performance. Regarding D, increasing it leads to important performance enhancement, but, again, structural requirements become restrictive. Increasing D also affect the external shape of the rocket, to be minimized. A compromise between all these aspects is considered to be the configuration shown in Table 3.10.

Table 3.10: Design Point

Variable	Value
External grain diameter	14 mm
Internal grain diameter	6 mm
Grain length	150 mm
Nozzle throat diameter	4 mm
Nozzle exit diameter	12 mm

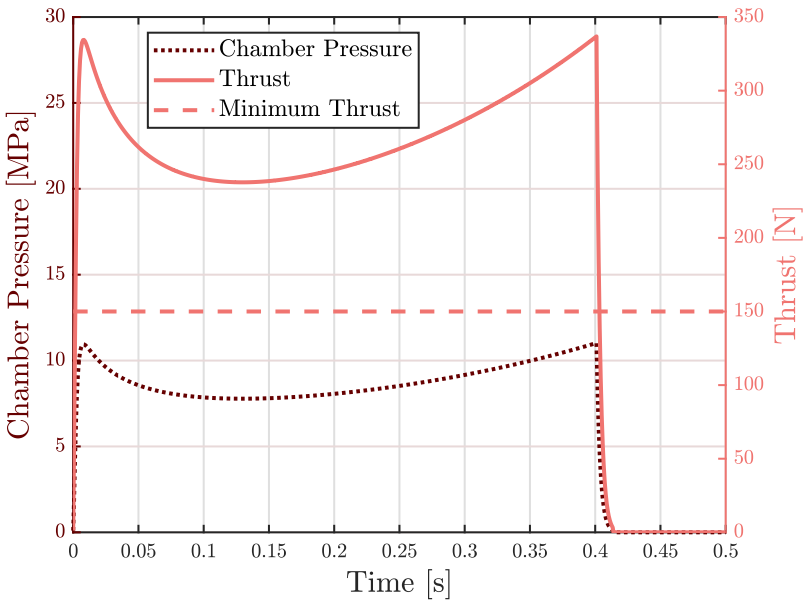

Figure 3.12: Design point operation.

The predicted performance is shown in Figure 3.12, together with the minimum thrust

requirement. The design total impulse is $\simeq 108\ N \cdot s$. Total burning time is close to 0.4 seconds. Erosive burning influence is significant, due to $L/d_0 = 25$. This erosive burning effect is desired in this platform, as it can be used to obtain higher at initial instants. Such behaviour is appreciated by the initial pressure and thrust peak, which is very close in magnitude to that of the burn-out. This motor configuration exceeds well the lower thrust limit (i.e., the maximum developed thrust is $\sim$ 337 N, while the minimum thrust set from requirements is 150 N).

3.8 Design and Manufacturing

A rocket motor is composed of, basically, four structural components: the nozzle and bulkhead ends, the motor casing, and the propellant grain. There are additional components, such as spacers, washers, ignition system, etc. This section details the design and manufacturing of a solid rocket motor, based on the geometry defined in the previous section.

3.8.1 Propellant Grain

The propellant grain is manufactured from a bigger rocket motor. Cylinders of propellant of the desired length and external diameter are machined, employing standard milling tools. Once the grains are already machined, the internal grain port is manufactured using acetone and drilled to the desired length and diameter. Acetone is used in this step because it dissolves nitrocellulose, the main constituent of the propellant used. Special care is required in this step to

Figure 3.13: Propellant grain.

avoid structural threats to the grain. Moreover, due to manufacturing constraints, only cylindrical ports can be manufactured. Figure 3.13 shows a manufactured propellant grain.

From various sources [81][58], it is found that temperature sensitivity of double base propellants typically oscilate between 0.003/$^{\circ}C$ and 0.006/$^{\circ}C$, depending on propellant composition. For the propellant in use, it is estimated to be $\sigma_p \sim$ 0.0035/$^{\circ}C$.

3.8.2 Motor Casing

The motor casing has two basic purposes: hold all structural components, such as the propellant grain, and contain and resist the combustion taking place inside. Therefore, it must be designed to withstand the tremendous pressures developed during operation. The stresses developed in the cylinder walls by an internal pressure can be expressed through by the well-known Barlow's Formula,

$$\sigma = \frac{P \cdot r}{t} \tag{3.35}$$

where σ are the stresses developed in the walls, P is the internal pressure, r is the cylinder internal radius, and t is the wall thickness. σ must be lower than the tensile yield strength of the material, σ_y, to avoid plastic deformations and structural failure. For aluminum 6061-T4, $\sigma_y = 170\ MPa$. With an internal radius of $14\ mm$ ($13.5\ mm$ of propellant + $0.5\ mm$ of inhibitor), a maximum pressure of operation of $11\ MPa$, and a safety factor of 2, the minimum thickness of the casing must be:

$$t_{min} \simeq 0.91mm. \tag{3.36}$$

Final thickness is set to 1.5 mm, for manufacturing reasons. This is a conservative approach that complies with the minimum value required. On the other hand, the casing

features threaded ends to allow the assembly with the bulkhead and the nozzle support. The manufacturing of the casing involves a simple machining process. A cylinder of the desired external diameter of Aluminum 6061-T4 is employed. Facing machining operations are used to reduced the original cylinder length, and a drilling operation machines the internal diameter.

3.8.3 Nozzle

The nozzle is, perhaps, the most important component in terms of performance influence. Its shape and geometry are critical in achieving the desired operation. In terms of design, given that the throat area and the expansion ratio are already fixed from the previous analysis, the only design choice left is the nozzle internal geometry. The determination of this geometry is typically based on a fluid-mechanic analysis, to produce the optimal nozzle shape that minimizes losses. This design is usually driven by the Method of Characteristics (MoC). Already included in commercial codes, it provides a technique for properly designing the contour of a supersonic nozzle for shock free, isentropic flow [82][83], and it is widely applied for nozzle design optimization [84]. The output of such technique is, usually, a curve that smoothly fits the throat and exit areas. For this project, however, there exists a limitation on the graphite machining capabilities, that makes impossible the manufacturing of that curved geometry. Therefore, a simple conical shape is proposed. Such shapes have been extensively used in the past and are well-known geometries. Figure 3.14 shows the nozzle design for the rocket motor, displaying the convergent and divergent sections, where the flow transitions from subsonic to su-

Figure 3.14: Rocket nozzle.

personic, following throat choking. Figure 3.15 depicts the convergent and divergent sections of the manufactured graphite nozzle.

Figure 3.15: Views of the manufactured graphite nozzle.

3.8.4 Ignition System

The ignition system is in charge of inducing grain combustion in a predictable and repeatable manner, which is, typically, a complex task, due to the different processes that appear simultaneously. It is as a combination of an energy contribution from an external source (the igniter) and from exothermic reactions generated near the propellant surface. All these chemical reactions may be reduced to a few reactions that dominate the total ignition rate. On a first approach, it may be intuitive to think that propellant ignition is solely influenced by propellant burning area, autoignition temperature, ignition characteristics of the propellant, etc. Therefore, it is coherent to study the heat fluxes to the propellant, and to understand the propellant response to such ignition. Based on that simple reasoning, the ignition charge needed to start the motor combustion [50]

may be estimated from

$$W = \frac{Q}{\Delta H} \tag{3.37}$$

where Q is the ignition energy requirement, and ΔH is the heat of explosion of the igniter. That energy required for satisfactory ignition, Q, can be estimated through different means. Studies from the U.S Naval Ordnance Laboratory, reference [50], provide an empirical relationship between various rocket parameters and such energy Q; the Bryan - Lawrence Equation [50][85];

$$Q = 38 \left[(A \cdot q_c) \left\{ \frac{\sqrt{L_g 4\pi A_p}}{A} \right\}^{0.59} \right]^{1.06} \tag{3.38}$$

where q_c is the ignitability of propellant, A_p is the port area, A is the area exposed to ignition products, and L_c is the grain length. The propellant in use is estimated to have $q_c \approx 0.24\ cal/cm^2$. Assuming A = A_p, the current motor configuration requires

$$Q = 523.5\ cal. \tag{3.39}$$

Using Equation 3.37, with $\Delta H \approx 1000\ cal/gr$ for the igniter constituent,

$$W = 0.5235\ g. \tag{3.40}$$

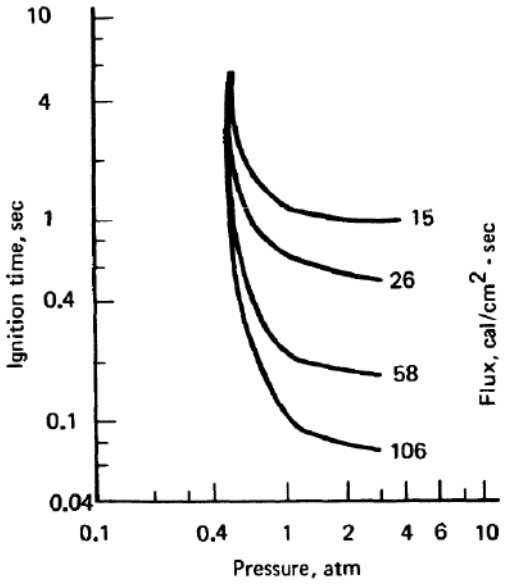

Figure 3.16: Influence of pressure on Ignition. Retrieved from [50]

However, there is a significant contribution to such ignition caused by gas pressure, which also affects the design of the ignition system. Rocket propellants present the so-called 'critical ignition pressure' [50], below which, even under the appropiate heat fluxes, ignition will not be stable. This condition

is depicted in Figure 3.16, showing ignition times vs pressure, for various ignition heat fluxes.

This conclusion highlights that propellants turn difficult to ignite in low pressure conditions. Moreover, if the ignition is completed, but the pressure is low, the burning rate of the propellant will be insufficient, and proper operation won't be reached. Therefore, an igniter must fulfill two objectives:

- Raise propellant temperature above autoignition.
- Raise pressure above the propellant critical threshold to ensure a stable and smooth combustion.

While the first condition may be fulfilled with the development described by Equation 3.37 and Equation 3.38, the second demand requires further validation. Typically, ignition pressure must be close to 60% of the motor working pressure [49], which is, for the current design, P_{crit} = 6.6 MPa. Pressure generated by ignition can be estimated through the equation of state of the ignition gases [50], based on the ideal gas law, and given by Equation 3.41:

$$P_{ignition} = \frac{\delta}{\delta - \Delta} \cdot \Delta \cdot \lambda \cdot G \cdot (1 - fs) + P_a \tag{3.41}$$

where P is the pressure in the combustion chamber, δ is the density of charge material, Δ is the loading density, $\lambda = R \cdot T/M$ is the effective force of igniter component (i.e., *R* is the universal gas constant, T is the ignition flame temperature, and M is the weighted mean molecular weight of gaseous products), Δ is the loading density (i.e., mass igniter / V, where V is the combustion chamber free volume), G is the fraction of original charge mass consumed in a given time, and P_a is the atmospheric pressure. The factor f_s indicates that, from the whole igniter charge (i.e., $mass_{ign}$), only $(1 - fs) \cdot mass_{ign}$ is in gas state [49]. This factor is typically $fs \sim 0.7$.

Assuming that the maximum pressure within ignition happens when all igniter charge is consumed, $G = 1$. For black powder, the effective force is close to 11800000 N/kg. Using Equation 3.40, and Equation 3.41,

$$P_{ignition} = 7.682MPa \tag{3.42}$$

This value is above P_{crit}. Therefore, the igniter design must fulfill the condition of having, as igniter charge, at least 0.523 g, for proper ignition.

With these two premises, an igniter design can be posed, conforming a pyrotechnic train of two components: an initiator, which transforms an energy input into heat energy, and a energy release system, which captures this heat flux, ignites, and outputs the energy that starts propellant ignition. An example of the system is shown in Figure 3.17.

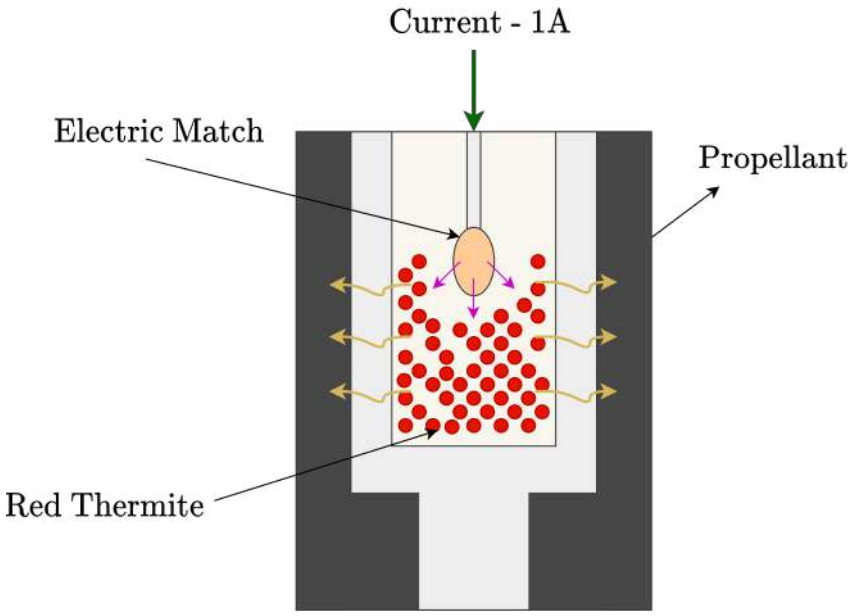

Figure 3.17: Pyrotechnic train used as ignition system.

The initiator is, in this case, an electric match (which is the same as the one described in Table 2.1). The electric match, once ignited by the electric current induced after

the launch trigger, deflagrates and transmits heat fluxes to the heat release system, constituted by an energetic material charge. The heat release system increases that thermal input, transferring it to the propellant walls. Figure 3.17 depicts the pyrotechnic train employed.

3.8.5 Additional Components

Apart from those critical components, there are additional parts which are required for a proper design. These are, basically, two threaded caps, at both motor ends, which support the nozzle and the ignition system. Embedded into these caps, o-rings are placed to avoid gas leakage and depressurization.

Figure 3.18: Complete rocket motor assembly.

Another component of importance is the inhibitor, which serves as interface between the propellant grain and the motor casing. This component must be a thin, heat resistant layer, bonded to the propellant grain, and to the walls. While, typically, inhibitors are also used to control the burning area, or to restrict burning to specific regions of the grain, in this case its solely purpose is the casing protection from the hot gases produced inside. It is made of carbon fiber, as it is a cost-effective solution that provides, as a first approximation, sufficient protection to the motor casing.

Figure 3.19: Rocket components components.

The manufactured components are shown in Figure 3.19. On the left side of the figure, there is the aluminum casing with the threaded ends. On the right side, may the reader observe the propellant grain, the electronics, the nozzle, and the separation rings. Figure 3.18 shows a rendered version of the design. The ignition system is placed near the bulkhead end, in red, embedded into the propellant grain. The separation rings are placed between the electronics, the nozzle, and the grain.

This page intentionally left blank

4

Experimental Campaign

This chapter presents the results obtained from the experimental campaign, for both stages. Results are analyzed, and post processed.

Contents

4.1 Propellant Strand Burner Test Campaign

The propellant used for the second stage, whose composition is described in Table 4.1, was not characterized in terms of combustion characteristics (Adiabatic Flame Temperature, Burning Rate, etc) when this project started. The determination of these parameters is, therefore, fundamental. In particular, it is found from various sources [86][87][88], that the Adiabatic Flame Temperature (which is assumed to be the chamber temperature in the model) typically oscillates between 2500 and 3600 K for double

base propellants. Given the particular composition of the propellant in use, the adiabatic flame temperature is assumed to be 3000 K.

Table 4.1: Propellant composition.

Component	%wt
Nitrocellulose	60
Nitroglycerine	35
Metal Content	3
Centrallite	2

On the other hand, the burning rate parameters, a and n, are completely necessary to estimate the performance of the rocket motor. An experimental campaign using a Strand Burner is conducted, by testing 28 samples (i.e., ”strands”).

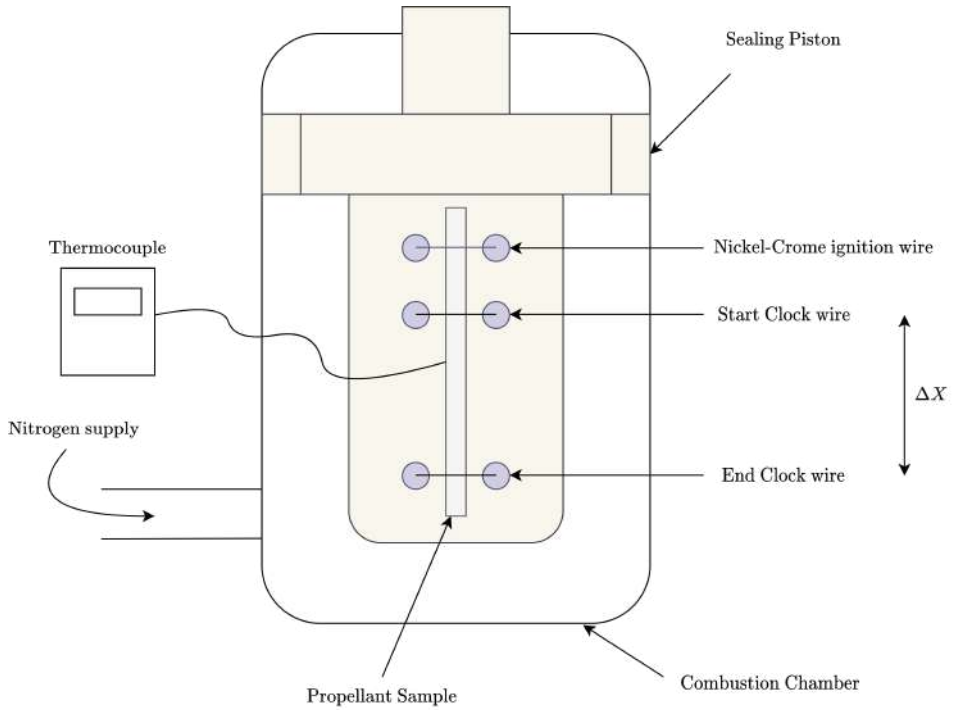

Figure 4.1: Strand burner schematics.

A Strand Burner, also known as Crawford Burner, is a device used to burn, at controlled pressures and temperatures, small inhibited samples of propellant. During the controlled burn, it is possible to obtain measurements on the velocity at which the propellant burns, for a given pressure and temperature, from

$$r = \frac{\Delta X}{\Delta T} \tag{4.1}$$

where ΔX is the length of the propellant sample between the Start Clock and End Clock wires of Figure 4.1, and ΔT is the time needed to burn it. Employing the well-known relation $r = aP_0^n$, the constants a and n can be empirically determined. Figure 4.2 shows the strands used for this experimental campaign.

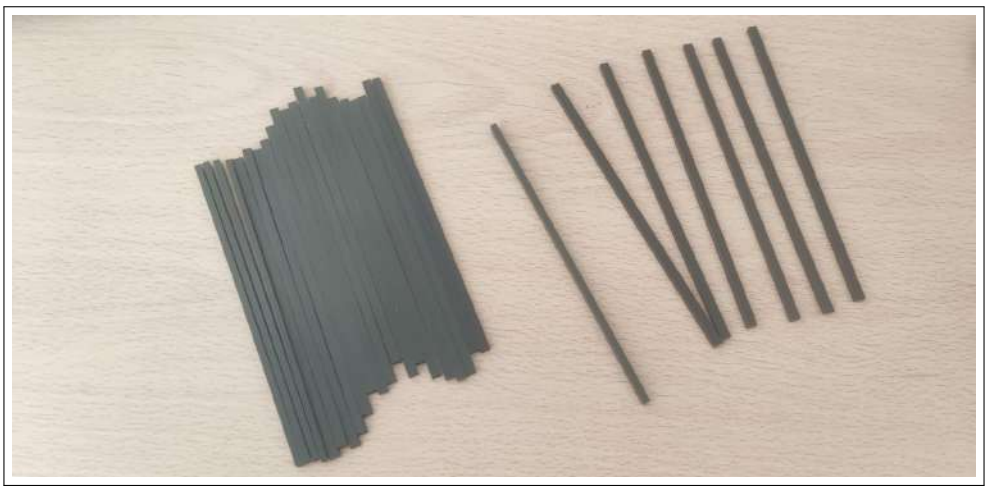

Figure 4.2: Strands used for Crawford burner testing.

The tests were conducted at the Chemical Propulsion Department of INTA, during the first two weeks of May, 2023. Results of the tests are plotted in Figure 4.3. The temperature set for all tests is 22$^{\circ}C$. Different pressures that the propellant will experience during operation are studied.

Experimental results manifest that this is a low-burning rate propellant, which presents

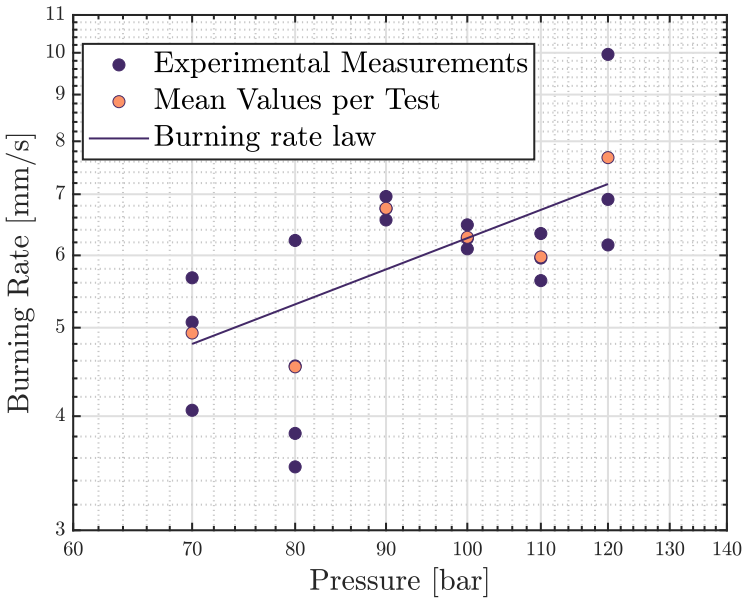

Figure 4.3: Burning rate measurements and burning rate law.

slow burning at low pressures (and high dispersion in the experimental data[i]). Once above 90 bar, obtained data is more clustered and presents a mesa behaviour, with the burning rate being reduced as pressure rises. This performance, although not usual (as it involves a negative n), is present in certain propellant compositions due to the use of additives. This is, probably, the operating pressure range for this propellant. Ideally, the burning rate law would be, therefore, a piecewise function whose parameters depend on the pressure under consideration. However, it is a common practice in these studies to simplify such burning rate estimation by using values at the limits and at an intermediate pressure [89]. Such procedure leads to the following burning rate law, which is plotted together with the data in Figure 4.3.

$$r = 0.2P^{0.8} \tag{4.2}$$

[i] As the propellant, probably, is not designed to work in this range.

4.2 Stage I Test Campaign

The Test Campaign of stage I is based on six experimental tests that obtain experimental measurements of the projectile displacement, employing Photron Fastcam Nova S12 High Speed Cameras. These results are processed to obtain velocities and accelerations, among other studied variables. Prior to each test, the gas generator is armed. The procedure is based on a strict series of instructions, shown in Figure 4.4. A fundamental guideline, not listed there, is related to the manipulation of the electric matches: to avoid accidental combustion and release of the firing pin, all manipulation prior to the test must be done without any power connection. All indications listed are based on a repetitive procedure, aiming for simplicity:

- **First Step:** the igniter is introduced in the propellant capsule. The connection cable passes through the hole at the bottom of the capsule. A plastic piece is introduced between the igniter and the capsule walls to ensure capsule integrity, and to concentrate the ignition.
- **Second Step:** the propellant is carefully loaded in the capsule, filling up all the available space. The whole propellant charge is 2-3 g. Special care needs to be taken in this step, to avoid ignition hazards.
- **Third Step:** an adhesive tape is placed on top of the propellant capsule to avoid spillage of propellant, when manipulating the capsule.
- **Fourth Step:** the propellant capsule is introduced in the cylinder, until it touches the bottom. The adhesive tape is placed to avoid propellant spillage in this step.
- **Fifth Step:** the firing pin is also introduced in the cylinder, immediately above the propellant capsule.
- **Sixth Step:** the spring is placed above the firing pin, between it and the cylinder walls. The spring must be straight and not bended, as one of the spring duties is

the guidance of the firing pin.

- **Seventh Step:** the cartridge adapter is threaded at the end of the cylinder, compressing the spring and the firing pin against the propellant capsule.
- **Eighth Step:** the gas cartridge is threaded to the cartridge adaptor.

After this process, the gas generator is a *hot* system. Adequate handling is needed now, following common military standards.

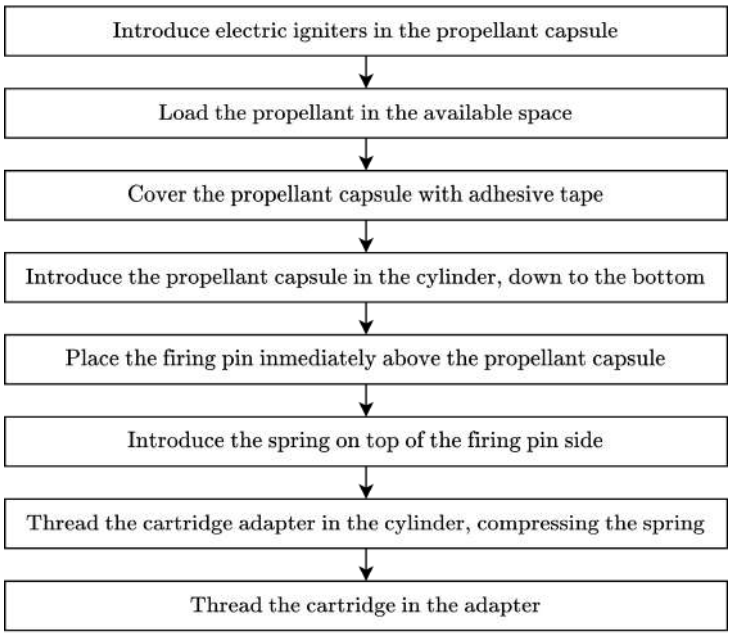

Figure 4.4: Arming procedure of the gas generator.

4.2.1 Test Setup

The body of the stage and the nozzle are then threaded around the gas generator, as indicated in Chapter 2. The electric igniter is connected to the electronic module embedded in the nozzle lateral, which is sealed using cyanoacrylate adhesive, to avoid leakage of gas from the nozzle. Once the complete system is ready, it is inserted in a canister (i.e., cannon), using the guiding rails, which ensure proper connection between

the electronic modules of the projectile and the canister. The canister is manufactured using additive PLA Manufacturing, and it features a muzzle brake at the exit, for redirecting the expelled gases. It reduces the recoil, and increases muzzle velocity. This canister is placed on top of a load cell of 100 kg, which is used to measure the recoil of the canister as the projectile is launched. This feature is fundamental to certify its used on aerial platforms, guaranteeing an operation within their flight envelope. Moreover, the canister also presents a lateral methacrylate window to analyze the internal ballistics of the projectile while it is moving inside the canister, after the launch trigger. Finally, an external LED is installed on a lateral wall. It is activated at the same moment the trigger is executed, and it is used to measure the response time of the system (time between trigger and ignition).

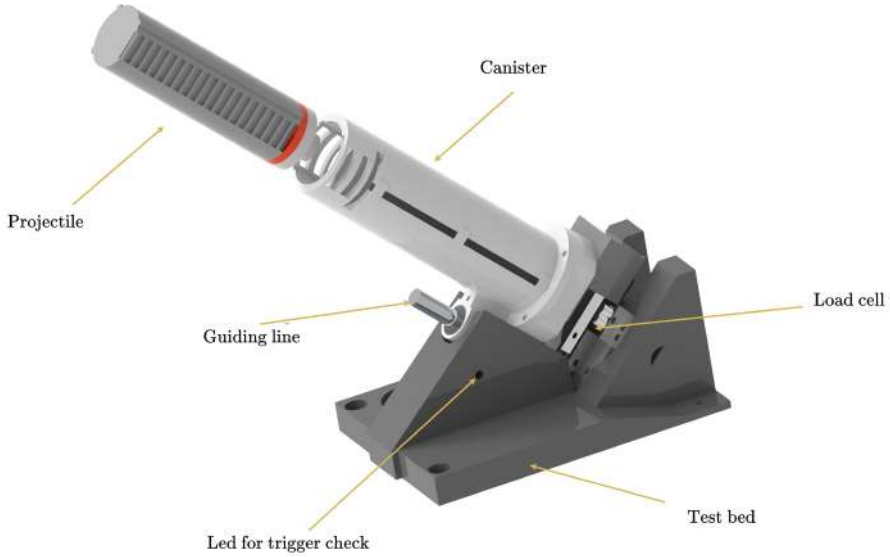

Figure 4.5: Test table render for stage I testing.

Figure 4.5 shows the test table used for Stage I testing. As the reader may notice, there is also a metallic guiding line with an embedded cylindrical bearing that supports the canister at 45°, and allows free displacement of the canister in the axial direction, for the recoil measurements. The high speed camera is placed exactly at 90°, with respect to the projectile symmetry axis, and 90° with respect to the test table lateral

wall. The resolution of the camera is 1024x1024, with $5 \cdot 10^{-4}\ mm/px$. The frame rate is 3000 fps, and the shutter speed is set to $1/20000\ s$. These characteristics are fixed for all tests, except for tests 5 and 6, where 5000 fps are set. The test table and the test setup are shown in Figure 4.6 and Figure 4.7.

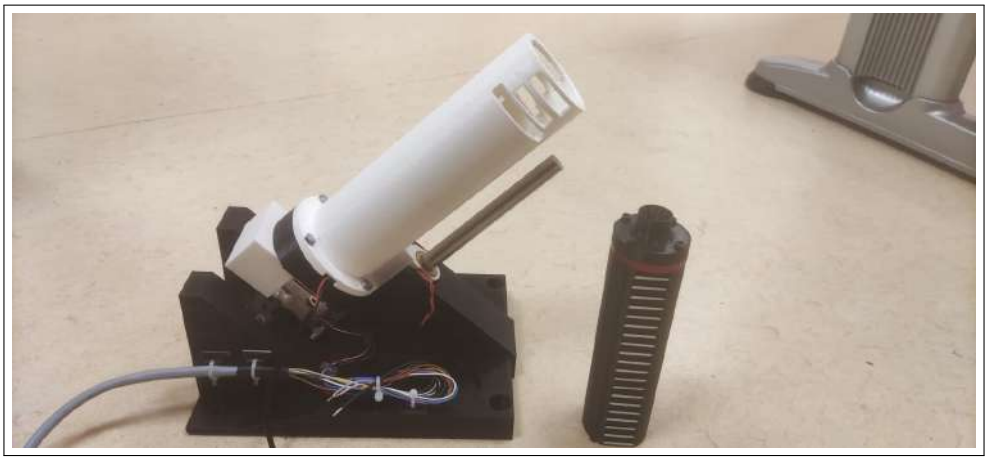

Figure 4.6: Test Table and stage I.

Figure 4.7: Stage I test setup, with high speed camera.

4.2.2 Tests Results

Figure 4.8 shows 4 selected frames of test 6. In particular, Figure 4.8a depicts the test setup, before the trigger is activated. The led is off and the projectile is inside the canister. In Figure 4.8b, the electric match has already ignited the propellant charge, and the pressurized gas is being expelled through the nozzle, moving the projectile forward. The LED is on (the white dot in the lateral wall), showing a response time of 16 ms.

(a) Frame 220

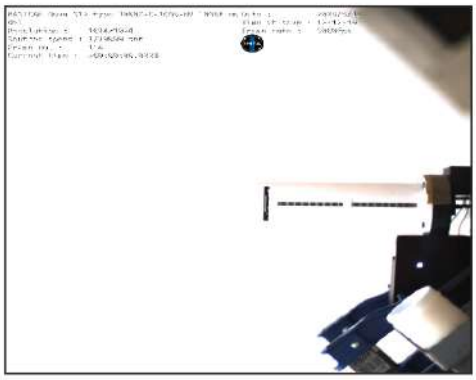

(b) Frame 265

(c) Frame 340.

(d) Frame 460

Figure 4.8: Various selected frames of test 6.

Figure 4.8c shows part of the projectile already outside the canister, while the remaining part is still being accelerated by the gas inside. Figure 4.8d shows the projectile completely deployed. In these last two frames, certain recoil is observed in the canister. This recoil is captured by the Load Cell.

Using the high speed cameras, the displacement of the projectile can be estimated and reconstructed. Such procedure involves an analysis of the number of pixels that the projectile advances per frame. It is also necessary to determine the ratio mm/px, through the calibrated pattern on the lateral of the projectile. Figure 4.9 shows the displacement of the projectile for each test. There is high similarity for the first four tests; both in the slope of the experimental curve and in the displacement reached after 35 ms. For the last two tests, there is a significant difference: test 5 resulted in a noticeable low velocity projectile, while test 6 featured the projectile with the highest speed among all cases. Both tests present a different slope in the experimental curve.

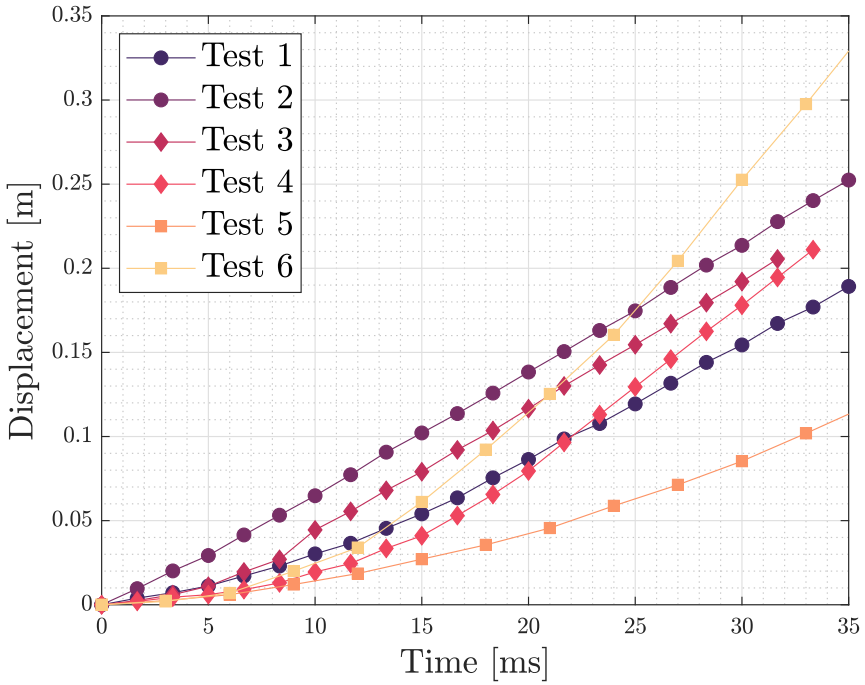

Figure 4.9: Displacements of the projectiles for the six tests.

These two last tests presented an important displacement of the test table as the projectile was launched, due to an incorrect setup. A pivoting motion around the points where the test table was fixed can be appreciated in the high speed videos. This behaviour may have influence the deployment of the projectiles. With respect to test 5, there were some issues in the manufacturing of the nozzle that lead to higher friction between the canister and the projectile. This situation is probably the cause of the low-speed projectile that can be seen in such case.

Once this data is extracted, post-processing to each test is applied. An example is shown in Figure 4.10. The fitting of the experimental displacement is depicted in red, together with the velocity and acceleration curves, in blue and black, respectively.

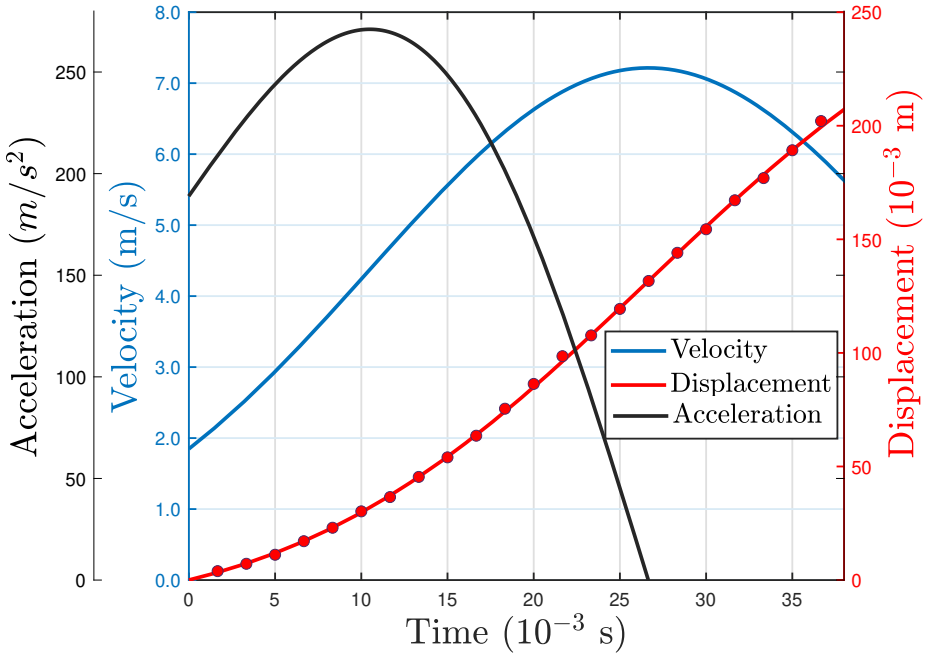

Figure 4.10: Processing of experimental data, velocity and acceleration.

The fitting of the experimental displacements is done using a sigmoid shape, using the error function,

$$y(t) = a + \frac{b}{2} \cdot erf\left(\frac{g \cdot (t-c)}{d}\right) \tag{4.3}$$

where $erf(x)$ is defined as

$$\text{erf}(x) = \frac{2}{\sqrt{\pi}} \int_0^x e^{-t^2} dt \tag{4.4}$$

The inflection point of such curve is the maximum point of the velocity. The same happens between the velocity and the acceleration. These are related, and obtained from the displacement fitting, through

$$v(t) = \frac{\partial y}{\partial t} = \frac{b \cdot g \cdot exp\left(-\frac{g^2(c-t)^2}{d^2}\right) \cdot \Gamma}{d} \tag{4.5}$$

$$a(t) = \frac{\partial v}{\partial t} = \frac{b \cdot g^3 \cdot exp\left(-\frac{g^2(c-t)^2}{d^2}\right) (c-t) \cdot 2\Gamma}{d} \tag{4.6}$$

with $\Gamma \approx 0.5642$.

The point of maximum acceleration takes place, approximately, immediately after the exit of the projectile through the muzzle, once the propulsion by the pressurized gas inside the canister finishes, and the only propulsion source is the remaining gas being expelled through the nozzle. The maximum velocity is reached shortly after that moment, once the mass flow through the nozzle decreases, and the projectile is in free flight, starting to decelerate. This projectile, therefore, behaves as a classic projectile while it is inside the barrel, where the internal ballistics are governed by the pressurized gas pushing it, and as a rocket once it clears the canister and the only source of propulsion is provided by the nozzle accelerating the pressurized gas. Of course, this analysis is valid in the instants immediately after the projectile deployment, and not for the remaining flight of the projectile, where another external ballistics study should be performed. Table 4.2 shows the fitting parameters of all 6 tests.

A summary of test results is displayed in Table 4.3, based on the same analysis previously described. The differences of test 5 and 6 in terms of force and muzzle velocity are noticeable.

Table 4.2: Fitting parameters of all tests.

Test number	a	b	c	d	g
1	0.1316	0.292	0.02665	0.1921	8.413
2	0.3206	1.365	0.0436	0.1362	1.394
3	0.1195	0.297	0.0203	0.0293	1.414
4	0.1403	0.284	0.0261	0.0163	1.051
5	0.1635	0.352	0.0434	0.0285	0.846
6	0.3509	0.7471	0.0362	0.0203	0.807

Table 4.3: Test results.

Test Number	Date	Ambient Temp. $[^{\circ}C]$	Hour	Maximum Force $[N]$	Muzzle Velocity [m/s]
1	01/12/2022	14	9:59	115.80	7.21
2	01/12/2022	14	10:52	25.20	7.82
3	23/03/2023	19	10:57	142.90	8.07
4	23/03/2023	19	11:05	244.18	10.33
5	11/05/2023	23	12:09	64.05	5.49
6	11/05/2023	23	12:12	244.78	16.73

From acceleration, the force curve provided by the projectile is easily estimated. From these force estimations, the total impulse provided by the projectile is computed through

$$I = \int_{t_1}^{t_2} F dt \tag{4.7}$$

where I is the total impulse in $N \cdot s$, F is the force (or thrust) provided by the projectile, in N, and t_1, t_2 are the time limits of integration. Table 4.4 shows the Total Impulse that each projectile provided, during the acceleration phase. Test 6 is noticeably outside the normal range, due to the previously commented error at the test stand. It should be noticed that the total impulse is quite low; while the force developed is considerable. This is due to the very short acceleration time that this technology presents; as it is thought to deploy the missile from the canister.

The energy of the projectile may be estimated, assuming that the air friction is negligible, and placing the reference zero for the potential energy at the test bed, from conservation of mechanical energy[ii]

$$E = \frac{1}{2}mv^2 \tag{4.8}$$

where m is the projectile mass in kg, v is the initial velocity, that it is assumed to be the highest velocity reached after exiting the barrel, in m/s, and E is the total mechanical energy of the projectile, in J. This energy is, therefore, the maximum kinetic energy that the projectile achieves during its motion, which is equal to the total mechanical energy, under the assumption of Conservation of Mechanical Energy. This increase in kinetic energy has an associated work done on the projectile, estimated as

Table 4.4: Total impulse results.

Test N°	Total Impulse [$N \cdot s$]
1	2.49
2	1.20
3	1.77
4	4.43
5	2.75
6	8.94

$$W = \int_{x_1}^{x_2} F dx \tag{4.9}$$

where W is the work done on the projectile, in J, by force F, in N, as it is displaced in x from x_1 to x_2. These two variables should be similar, taking into account that one of them is an overestimation, while the other is obtained from post-processing applied to the experimental data. Figure 4.11 shows these results, for each test. One outlier point corresponding to test 6 is removed from the dataset as its variance with respect to the mean is greater than 3σ, with $\sigma = 13.454J$.

[ii] In the absence of friction or similar effects, the projectile is only affected by conservative forces (i.e, gravity), thus the mechanical energy is conserved. This computation will overestimate the real Mechanical Energy of the object.

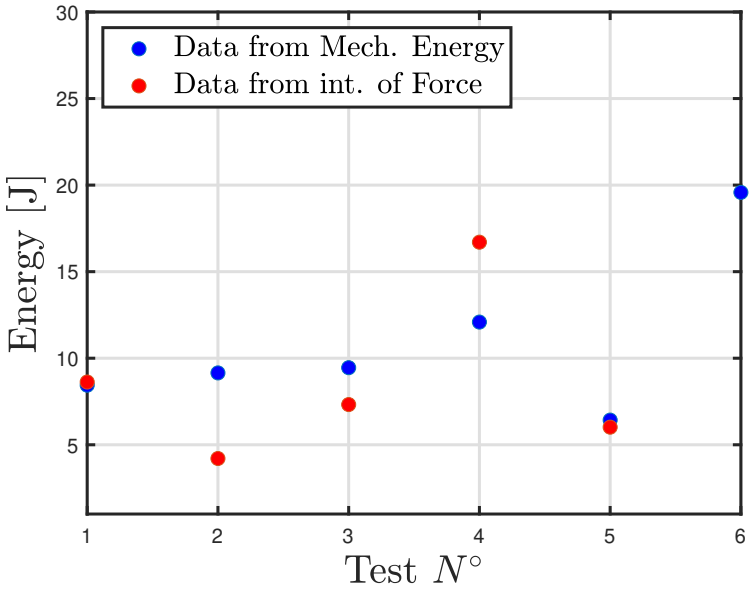

Figure 4.11: Projectile energy estimation by both methods.

Tests 1 and 5 show similar results, while tests 2,3 and 4 exhibit differences between both procedures. In general, the work obtained from the experimental data is lower than the mechanical energy obtained through the kinetic energy due to the previously mentioned overestimation.

Figure 4.12 shows the recoil experienced by the barrel in two of the tests. It is a dynamic and transient scenario characterized by three characteristic events.

- First peak, at $\sim$ 6 ms. This event corresponds to the ignition of the propellant charge. Its combustion gases, after pushing the firing pin upwards, are released through the exhaust channels towards the nozzle. This release generates a recoil which varies for these two tests between $\sim$ 140 N and $\sim$ 270 N.
- Second peak, at $\sim$ 12.5 ms. After combustion of the propellant charge, the firing pin perforates the cartridge seal. The stored gases are violently released through the nozzle, pressurizing the chamber, and moving the projectile forward. This pressurization appears as a sudden peak with a magnitude between $\sim$ 400 and

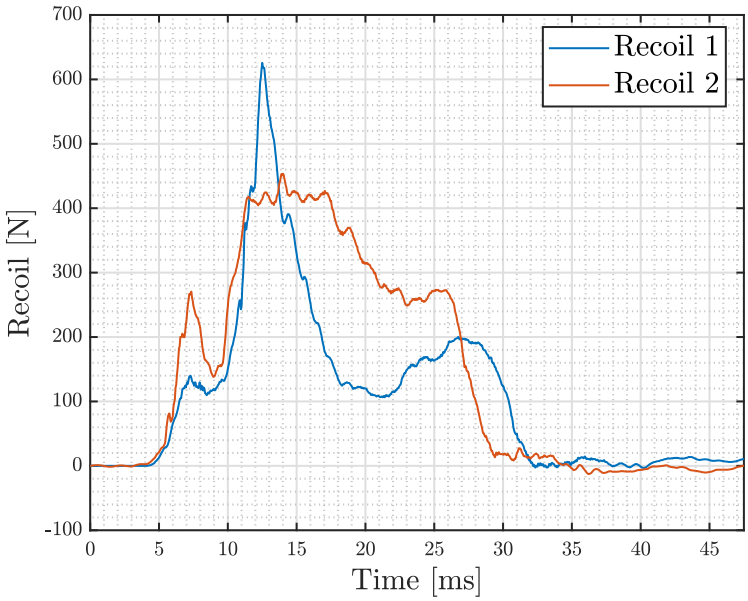

Figure 4.12: Barrel recoil.

$\sim$ 600 N, for the two tests shown. The impact of the firing pin with the cylinder bottom as it travels backwards is probably masked by this event.

- Third peak, at $\sim$ 27 ms. This secondary peak appears in the middle of the chamber depressurization process, as the volume increases when the projectile travels towards the muzzle. Two scenarios are considered as probable cause:

  - Rate of volume increase is faster than rate of gas entrance in the chamber from the projectile. This effect is seen as a transient suction, or deceleration inside the barrel. Once such effect is dissipated, the pressurization effect on recoil raises again.
  - There is intermittent mass flow through the nozzle, due to blockage at the cartridge exit, as a consequence of the gas expansion and freezing. Mass flow reduces and increases alternatively. When mass flow increases, there is a recoil increase.

4.3 Stage II Test Campaign

Stage II Test Campaign involves thrust measurement of a rocket motor, which is expected to be the second stage of a micro-missile. For such purpose, the rocket motor must be placed in a test bed, which features an ignition and acquisition system. This test bed is vertical, and is calibrated before every test. Figure 4.13 shows a typical calibration process, performed on two load cells assembled in series (i.e., they experience the same forces). Before each tests, the load cells are tared, and different weights are applied several times. In particular, the calibration process is also needed to verify that the load cell response does not present excessive overshoot, among other features.

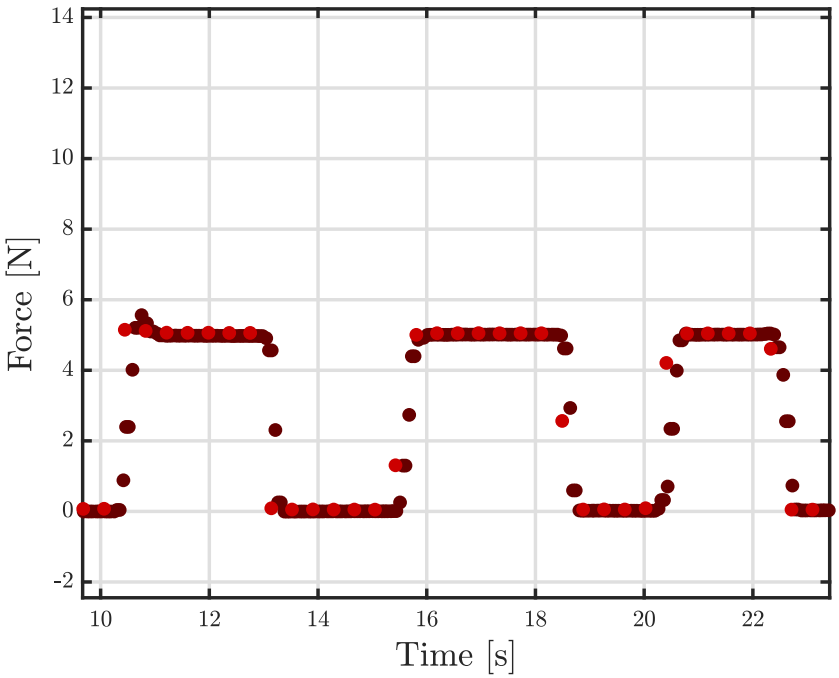

Figure 4.13: Load cells calibration process.

4.3.1 First test

First test is conducted on December, 1^{st}, 2022. Figure 4.14 shows the test setup. The rocket motor is embedded in the test table, over the metallic table, at the right corner. The high speed camera and the thermal camera are in front of the rocket motor, focused at the nozzle exit.

Figure 4.14: Experimental setup for test I, stage II.

The test ended in ignition failure. After the ignition trigger, a slight detonation is heard, which corresponds to the electric match ignition. However, the rocket motor is not correctly ignited, and an abort instruction is sent. Figure 4.15, right picture, shows the infrared image of the test at the moment of ignition trigger, taken by the thermal camera. The ignition wire, through which 1A is sent to the electric match, is heated and clearly visible here. The rocket motor, however, does not ignite.

Wiring and electronics modules were checked after test failure. All security and pre-operation tests were successfully passed. It was found that, probably, the energy release component of the ignition system did not deflagrate, but produced a detonation. Therefore, there was an inefficient energy transmission through the pyrotechnic train,

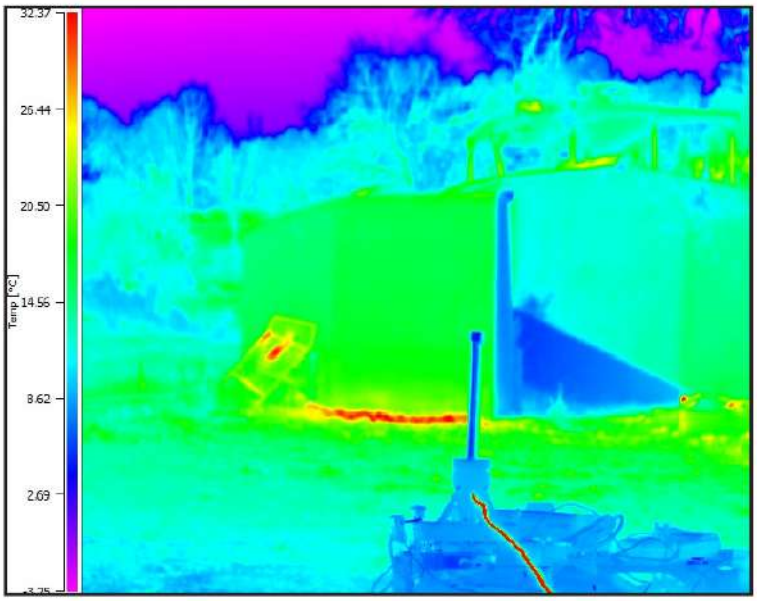

Figure 4.15: Infrared image of test 1, stage II.

which did not allow flame spreading through out the grain port. In fact, no ignition gases were visible at the rocket exhaust during the test, excepting those coming from the ignition system.

4.3.2 Second test

Second test is conducted on 1^{st}, December, 2022. The test setup is exactly the same as in test 1, Figure 4.14, which was aborted. After pre-operation tests, ignition was successfully triggered by the operator, through the wireless electronic modules.

Figure 4.17 reveals different instants of the rocket operation start. In particular, Figure 4.16a shows the ignition gases starting to flow out the nozzle, after deflagration of the electric match. Figure 4.16b exhibits the moment when all these gases leave

(a) Electric Match ignition

(b) Ignition gases exit

(c) Operation Starts

(d) Steady Operation

Figure 4.16: Various selected frames of the operation of Test 2, Stage II

the combustion chamber, immediately followed by grain ignition, as showed by Figure 4.16c, where part of the rocket plume is still composed of dark gases coming from ignition remnants, and part is due to the grain combustion gases. Figure 4.16d shows a fully developed plume at the nozzle exit, characteristic of steady operation. Moreover, certain gases are visible near the bulkhead end of the rocket, due to failure in the insulation of the electric match sealing. This can cause depressurization and reduced performance.

The normal rocket operation is interrupted, as Figure 4.17 shows, by a sudden explo-

(a) Catastrophic Failure at bulkhead

(b) Rocket body ejected upwards

(c) Test Stand displaced by explosion

(d) Capture of the grain covered by the inhibitor

Figure 4.17: Various selected frames of the catastrophic failure of Test 2, Stage II

sion at the bulkhead end. From Figure 4.17a, may the reader notice how, while the rocket is still at steady operation, a sudden explosion at the bulkhead end is originated. Obviously, this catastrophic event results in depressurization of rocket internal port, and combustion stoppage. Figure 4.17b shows how the force generated by the explosion ejects the rocket body upwards. At this moment, the load cell is also deformed and stops the reading.

Finally, Figure 4.17c shows the test stand, completely displaced and destroyed by the explosion, while Figure 4.17d shows the grain, still covered by the inhibitor, which was

not kept fixed to the rocket body, and remained in place during the event.

Figure 4.18: Broken Bulkhead of test 2.

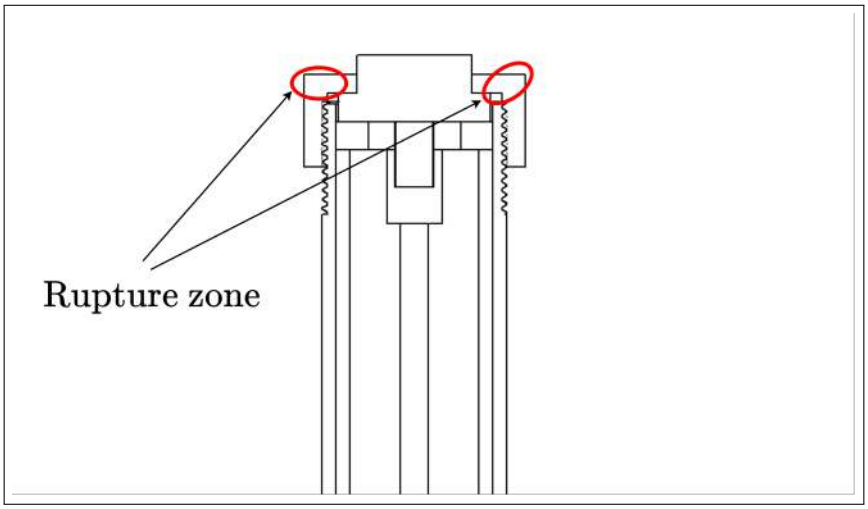

Figure 4.19: Rupture zones during test 2.

An investigation following this accident was conducted. It was found that the failure occurred at the threaded bolt that covered the electric match and sealed the bulkhead end. This part, already broken after being recovered, is shown in Figure 4.18. On the other hand, Figure 4.19 shows, in a motor draft, the rupture zones. Further analysis on the grain revealed that the ignition flame was not completely spread through out the entire port length, as the grain rests that survived the explosion did not show completely burned surfaces along the grain length. The grain was broken at a mid location. It can be seen in Figure 4.20.

The most suitable hypothesis that explains this failure is related to an overpressure at the chamber that exceeded the structural limit at the threaded bolt. Sonic blockage at the beginning of the grain port, where the propellant was broken, was discarded as failure cause, since the grain did not move upwards. That means that the pressure developed at the bulkhead end, and at the nozzle end, was the same (hydrostatic pressure), while sonic blockage at the port entrance would have lead to important pressure differences through out the chamber. In a similar way, sonic blockage at the port end is also discarded since the pressure developed there, near the nozzle, would be higher than that of the bulkhead end. Consequently, despite the fact that this possibility explains why the propellant grain is not driven upwards, it should have provoked failure at the nozzle end, due to the increase in pressure.

Figure 4.20: Propellant rupture

That initial pressure increase that lead to failure may be due to several reasons:

- Initial erosive burning pressure peak was underestimated during the design phase,

as a consequence of an insufficient implementation in the numerical model. Such peak may have lead to structural failure.

- The burning flame encounters a void or crack at the propellant surface, that leads to uncontrolled burning, area increase, and overpressure.

- Initial pressurization provided by the ignition system exceeds the casing structural limits.

Typically, double base propellants show high structural integrity. Therefore, the probable origin of the failure is, either an incorrect estimation of the initial erosive burning peak, or an overpressure coming from the ignition system. Consequently, the most suitable failure cause is an incorrect sizing of that bulkhead component, that did not support the developed chamber pressure.

4.3.3 Third Test

Third test is conducted on June, 5^{th}, 2023. Figure 4.21 shows the test apparatus. The rocket motor is placed, vertically, in the middle of the test bed, which holds it. Internal aluminum threaded rods are used to join the bulkhead and nozzle ends, reinforcing the structure in case of stresses induced by internal pressure in those areas. The load cell is below the rocket motor. A PLA component is placed on top of the test bed, surrounding the nozzle, to place the calibrated weights used during the load cells calibration process.

Figure 4.21: Test setup, test 3.

On the other hand, the bulkhead end, cause of failure in the previous test, was reinforced: its thickness was increased, and it was embedded in a metallic block. Figure 4.22 shows two views of the new bulkhead end design, with an internal o-ring. The ignition system should be located on the center of the component, embedded in the reinforced structure.

Figure 4.22: New bulkhead end

The test resulted in successful ignition. The whole propellant charge was burned. Figure 4.23 shows the nozzle after test, with minor damage and erosion, and the motor casing, with the inhibitor still joined to the internal wall, but without any propellant remnant or sliver.

Figure 4.23: Nozzle and casing after test 3.

Test results are shown in Figure 4.25, already post-processed and filtered. It can be seen that motor combustion, although successful, did not comply with the design point reference. There are three regions that can be identified:

- Motor start by ignition system: until 5 s, the igniter raises pressure in the combustion chamber due to the generated gases. There are three peaks during that period, that correspond to, firstly, the initial igniter deflagration, and secondly, to partial burns of the propellant and subsequent pressure increases. This event was identified during the test as three sudden gas exits through the nozzle.

- Ignition delay: between seconds 5 and 20, despite ignition system initiation, the propellant is not successful ignited. The operation enters in idle-regime, where part of the propellant is burning, but at an insufficient rate to sustain stable combustion and thrust generation. Propellant burns, without being able to rise pressure to enter in full-thrust regime, which requires chamber pressurization. Combustion gases simply exit the chamber.

- Full-thrust regime: pressure build-up is achieved when a sufficient burning area generates gases that pressurize the combustion chamber, inducing an appropiate burning rate, and a pressure rise. This operation is established between seconds 20 and 35, meaning that the motor experiences an abnormally high burning time: due to the previous propellant combustion (i.e., during phase II), and the higher free volume available, the remaining propellant is, probably, not able to perform at design point, and the chamber is not optimally pressurized.

Selected frames showing different instants of the rocket operation are shown in Figure 4.24.

(a) Ignition gases and particles.

(b) Third thrust peak during phase I.

(c) Idle regime.

(d) Full thrust regime.

Figure 4.24: Various selected frames of test 3.

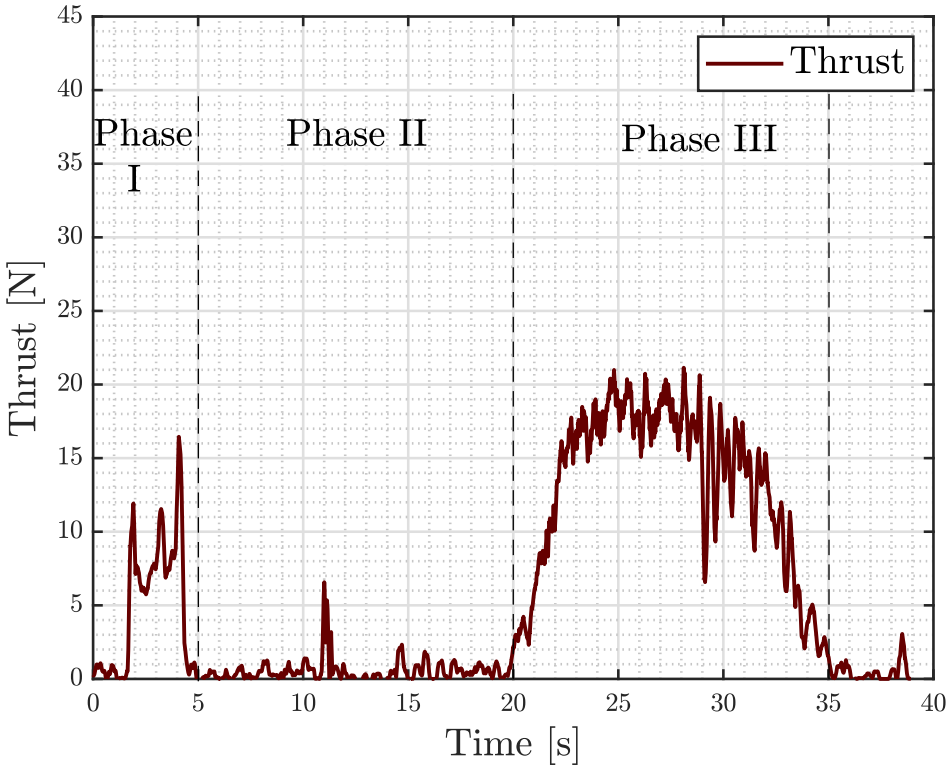

Figure 4.25: Motor operation, test 3.

This thrust spectra is the consequence, therefore, of unsuccessful ignition. The ignition system was not capable of raising the chamber pressure to a level where the propellant burning rate is sufficient to induce a consequent pressure increase that allows entering in full-thrust regime. Recalling that the pressure build-up is the convolution of the pressure waves from the ignition system, and the pressure generated by the combustion gases from the propellant, it can be hypothesize that the second contribution was not enough during a few seconds, until the burning area was high enough to pressurize the combustion chamber. Moreover, the erosive burning influence does not appear, as the motor, when entering into full-thrust operation, does not present a high L/d_0 ratio (i.e., consequence of the previous propellant waste).

Figure 4.26 shows a detail of phase III. There is a first pressure build-up, followed by the full-thrust regime which lasts, approximately, 5 seconds. Finally, there is a tail-off

process characterized by high pressure oscillations, consequence of the burning of unburned slivers and propellant remnants that remain inside the motor casing. This

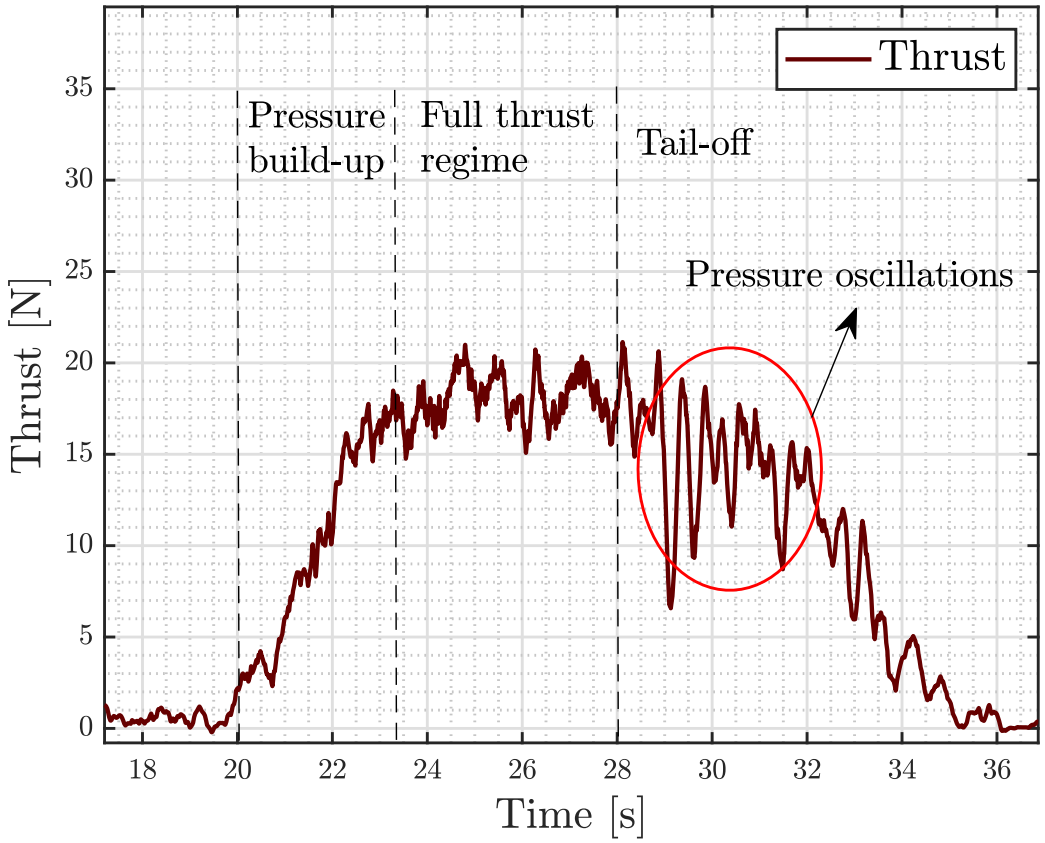

Figure 4.26: Detail of motor operation during full-thrust regime.

abnormal operation may be fixed by introducing a pressure burst at the nozzle throat. This device blocks the exit of gases from the combustion chamber, until the inner pressure reaches the desired condition. At that point, the pressure burst, which is calibrated, breaks, and the motor enters into normal operating regime. This facilitates the pressure build-up, ensuring a proper burning rate through out the entire grain port.

5

Conclusions, final remarks & Socio-Economic impact

5.1 Conclusions and Final Remarks

The propulsion technologies developed in this work have been tested, after design and prototyping, in an experimental campaign.

The feasibility of ACUS first stage propulsion, based on projectiles propelled by pressurized gas thrusters, has been successfully validated and tested through six different tests, without deployment failure. Moreover, a cheap and reliable projectile has been design, employing additive manufacturing and cost-effective solutions.

ACUS second stage propulsion, based on a classical SRM, has been tested in 3 different tests. 2 of them resulted in test failure, due to ignition and structural issues. The third test lead to a partial validation of the technology, as it demonstrated ignition and thrust capability. Complete stage validation still pends for future works.

Moreover, a numerical performance code based on a quasi-steady one dimensional model that estimates the internal ballistics and general performance figures of SRM has been implemented and validated, creating a tool that may be used in the future for preliminary rocket motor design and sizing.

Consequently, ACUS' first stage propulsion technology is validated. Such milestone is, after this project conclusion, still partially pending for the second stage.

5.2 Future Works

Future works should be mainly directed towards two directions:

- Continue with the first stage development, refining the repeatability of the external ballistics performance (muzzle velocity, force, acceleration, etc).
- Achieve a complete and stable operation in the second stage, and perform various firings without failure, by introducing changes in the proposed model, such as pressure bursts at the nozzle throat, or igniter design changes.

Apart from these steps, which are focused on the propulsion of the stages, more milestones should be reached, towards ACUS project completion. Recalling that this project is focused on the individual validation of each stage propulsion, future works should also study the following points:

- Study interface and structural integration between stages.
- Refinement of the propulsion proposal: weight and nozzle optimization, cartridge mass change, etc.
- Aerodynamic study of the stages, and consequent design changes.

5.3 Project Budget

Project's budget is broken down into the following:

- The mean gross salary of a *Científico Superior de la Defensa* INTA is around 3300 euros per month. Considering 160 working hours per month, the salary per hour is 20.6 euros approximately. The total number of hours employed in this project is 545 hours, divided, approximately, into the following parts:

  - 60 hours for literature and bibliography review.
  - 50 hours for preparation of the experimental campaign.
  - 20 hours for the tests of the experimental campaign.
  - 15 hours for assembly of prototypes.
  - 100 hours for the performance model development and validation.
  - 50 hours for data analysis and processing.
  - 250 hours for results interpretation and memory writing.

  Then, the total labor cost scales up to 11227 euros.

- During the project, the software used is MATLAB, employed for numerical computations and data treatment, among multiple applications. The annual basic license for the main program costs 800 euros. The toolbox *Curve Fitting Toolbox*, which is also used, costs 400 euros per year. The present work is typeset using LaTeX, a software system for document preparation, with the cloud-based editor Overleaf, using the free license.

  The equipment employed is an MSI Prestige computer laptop, which costs 1100 euros, and a computer and monitor at the laboratory, with a total cost of 800 euros. Depreciation of these goods is negligible.

- The electric matches bought have a cost of 30 euros. Electronic modules used for the ignition system and trigger of launch have a cost of 100 euros.

- The total PLA used for the manufacturing of the first stage raises up to 4 kg (including prototyping and design iterations). With an average cost of 35 euros/kg,

the total cost of PLA is 80 euros.

- High speed and thermal cameras, acquisition systems, and facilities used during the experimental campaign, are facilitated by INTA. The average cost of per day of experimental campaign is estimated to be 100 euros. Considering 15 days of use, total cost of cameras is 1500 euros.
- The gases used for the Crawford Burner Tests have a cost of 100 euros.
- Propellants used for first stage ignition are part of batches bought by the Spanish Ministry of Defence on a mass scale. Quantities used for project's experimental campaign have an insignificant cost.
- Burning Rate experimental measurements are done by the Chemical Propulsion Area of INTA. The cost of this experimental campaign is 3500 euros.
- Manufacturing cost of second stage (i.e., aluminum, machining operations, graphite, etc) is 300 euros.

Then, the total cost of the project rises to **19937 euros.**

5.4 Socio-Economic Impact

The socio-economic impact can be divided into two main sections:

- **Economic benefits:** The cost of the first stage (i.e., if used stand-alone as countermeasure), in terms of manufacturing, is around 5 euros (PLA, propellant charge, electric match and spring). This low value, even with the additional cost of integrating a flare architecture, highlights the enormous reduction in cost that this option presents against classic countermeasure decoy flares, such as the common M206 flare, which costs close to 35$ per unit [90].

- **Operational and security benefits:** The Spanish fleet of autonomous aerospace vehicles now has, available (upon certification and future design milestones), a new technology that can solve the absence of countermeasure and strike capabilities. This advancement constitutes a key asset that enhances security and operational flexibility against future conflicts. Recent military disputes (i.e., Ukraine - Russia War), have highlighted the necessity of flexibility against threads that can compromise defence in countries where counter-drone capabilities are limited. This new proposal tries to cover that limitation by the development of the described modules.

6

Appendix

6.1 Rocket motor casing drawing plans

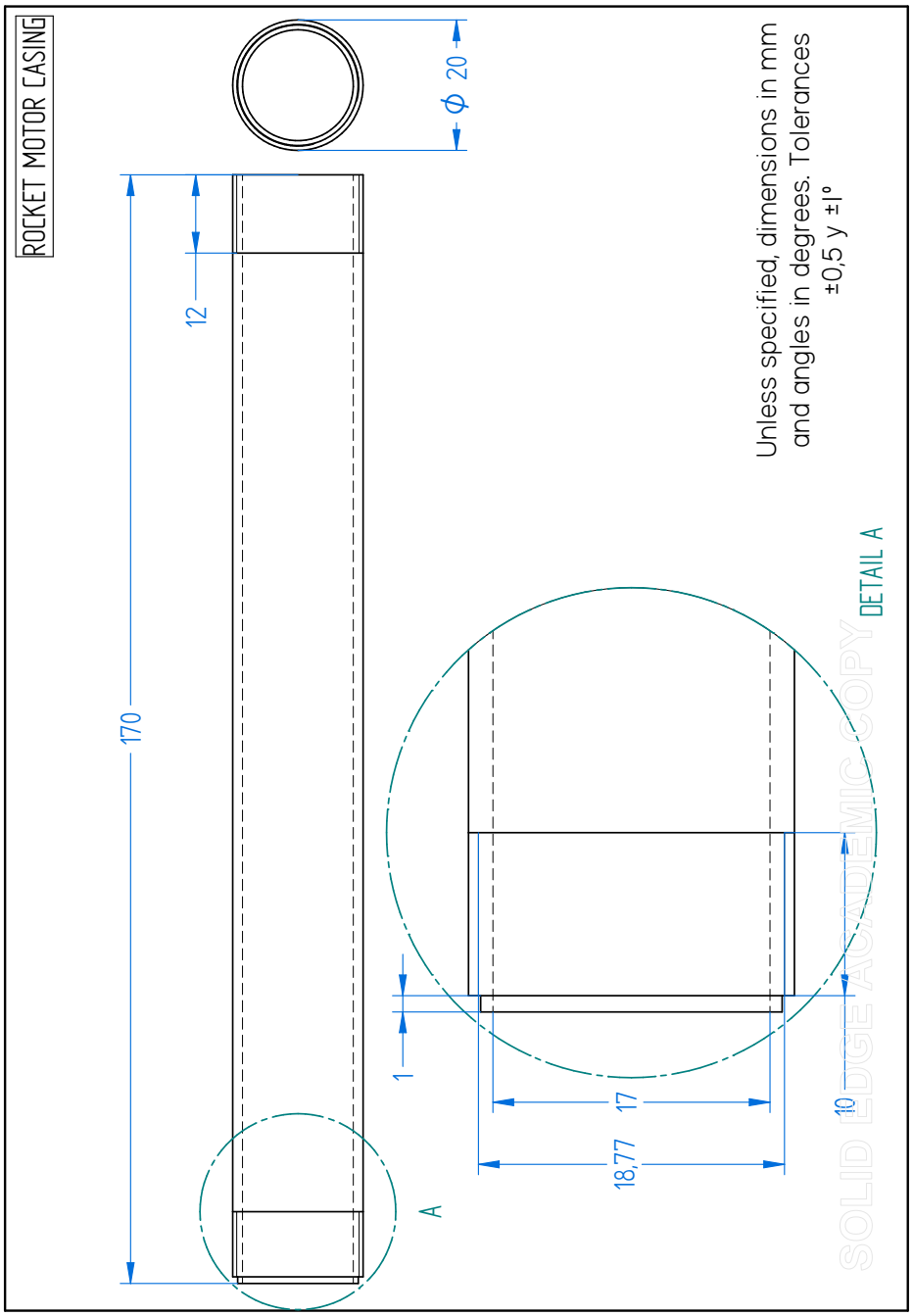

6.2 Rocket nozzle drawing plan.

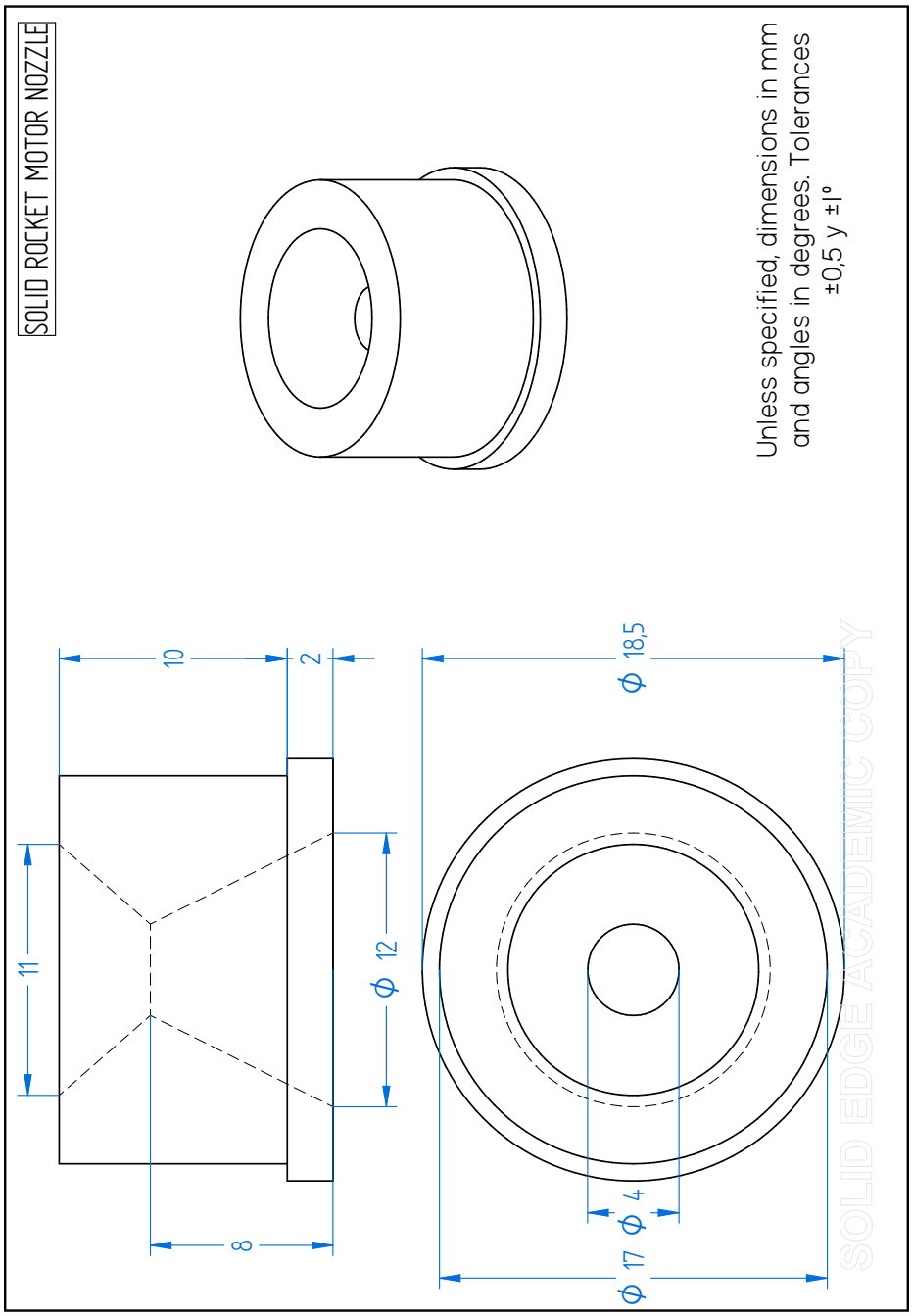

6.3 Bulkhead end drawing plan.

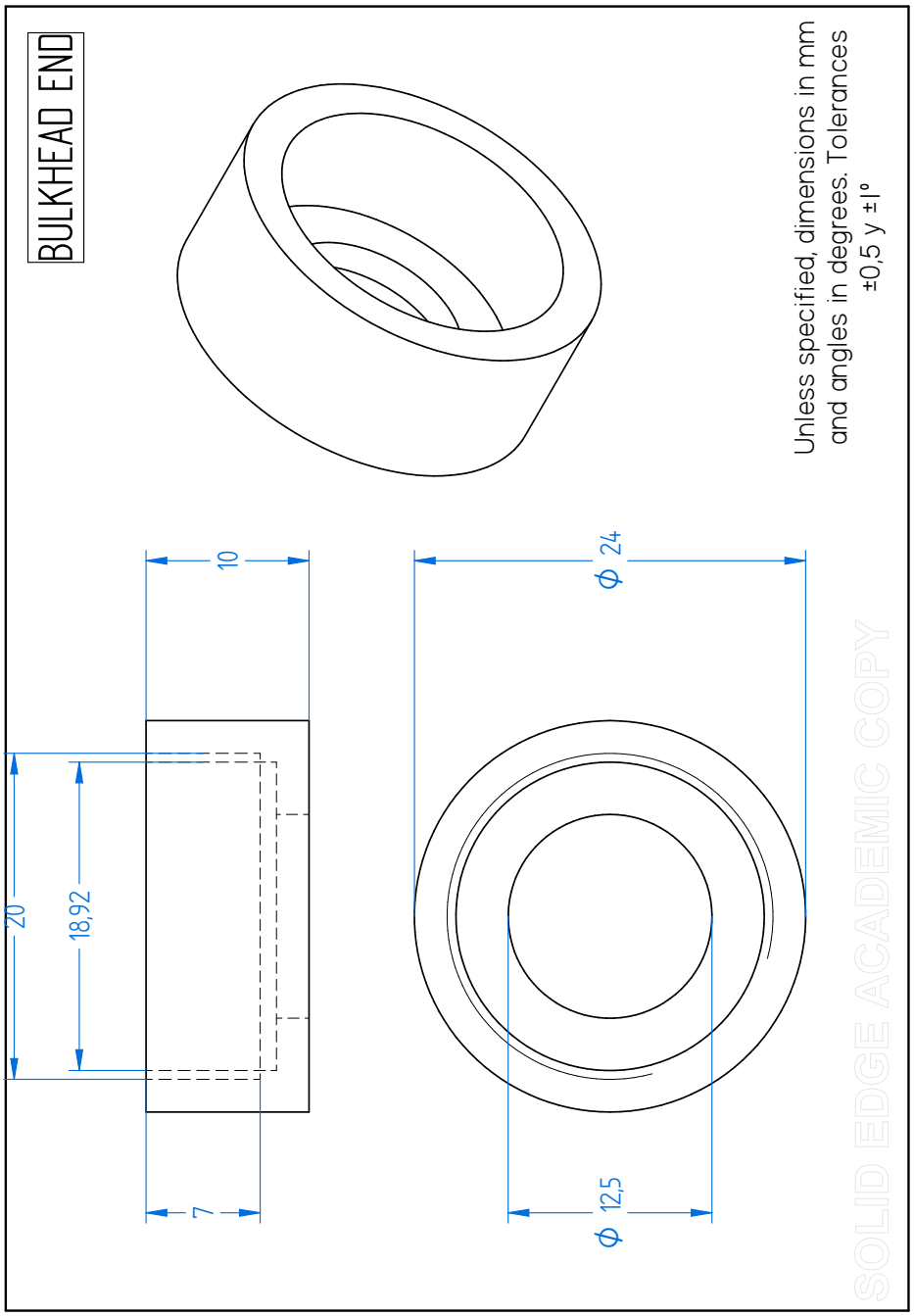

6.4 Nozzle end drawing plan.

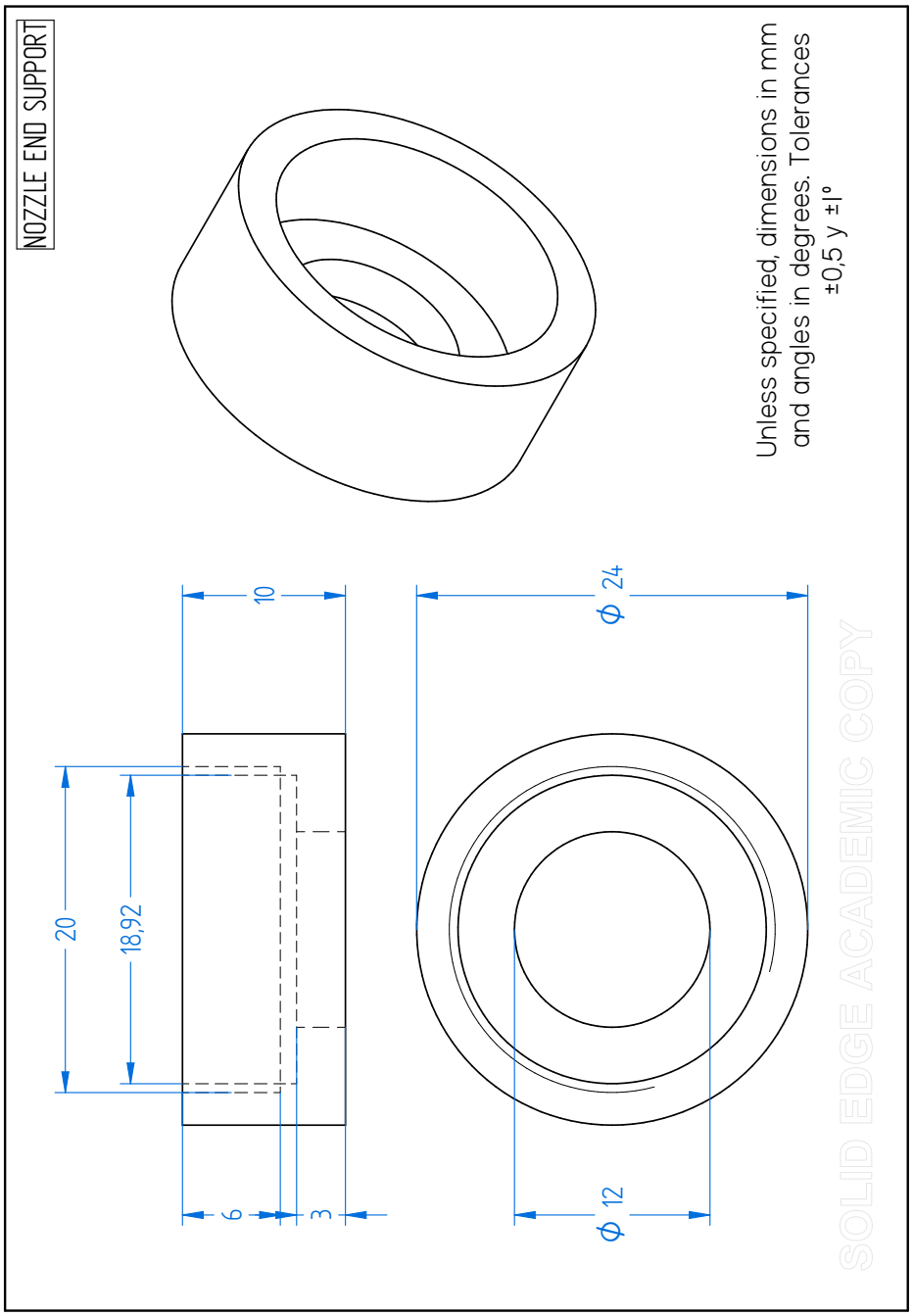

6.5 Spacer drawing plan.

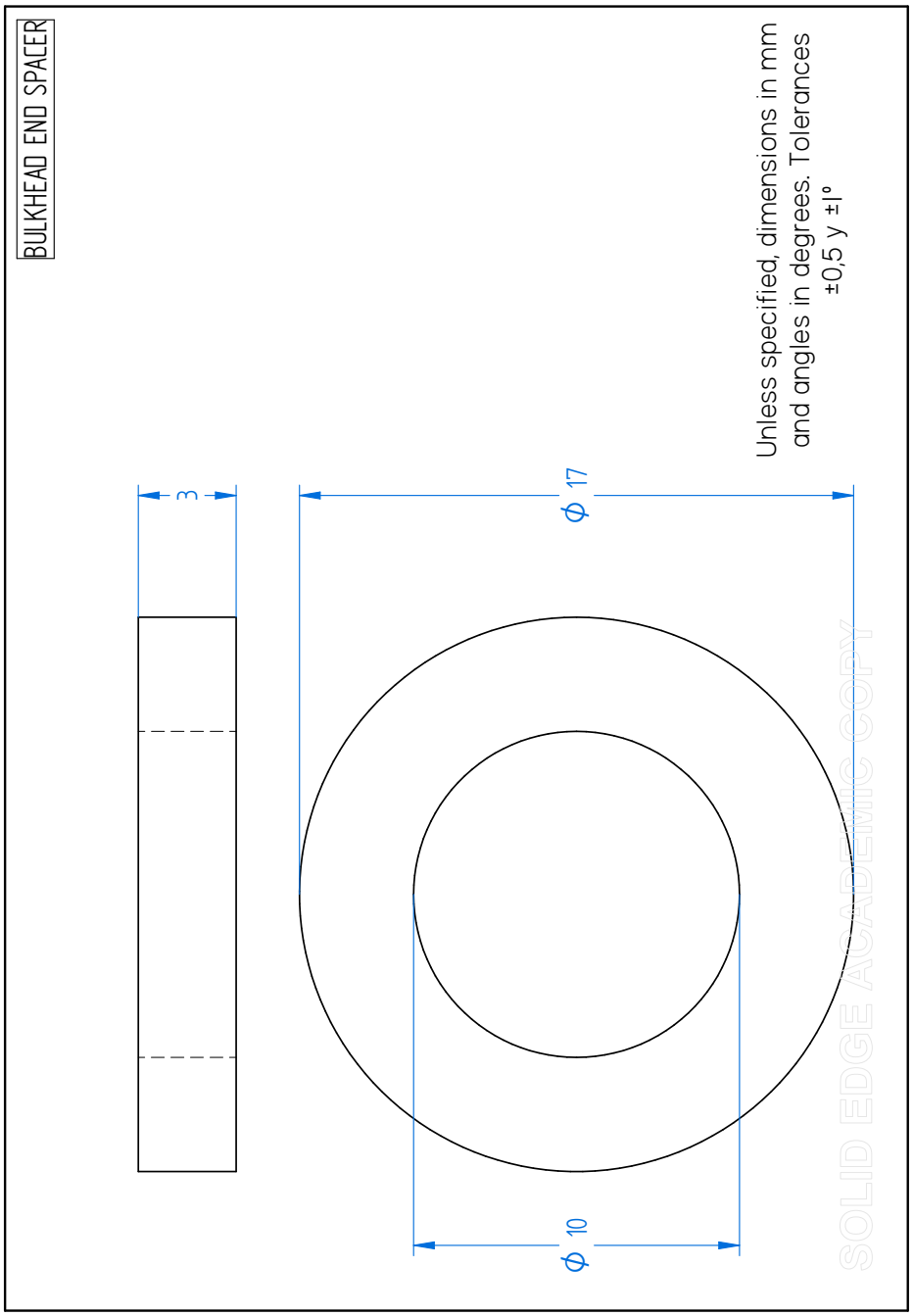

6.6 Gas generator cylinder drawing plans.

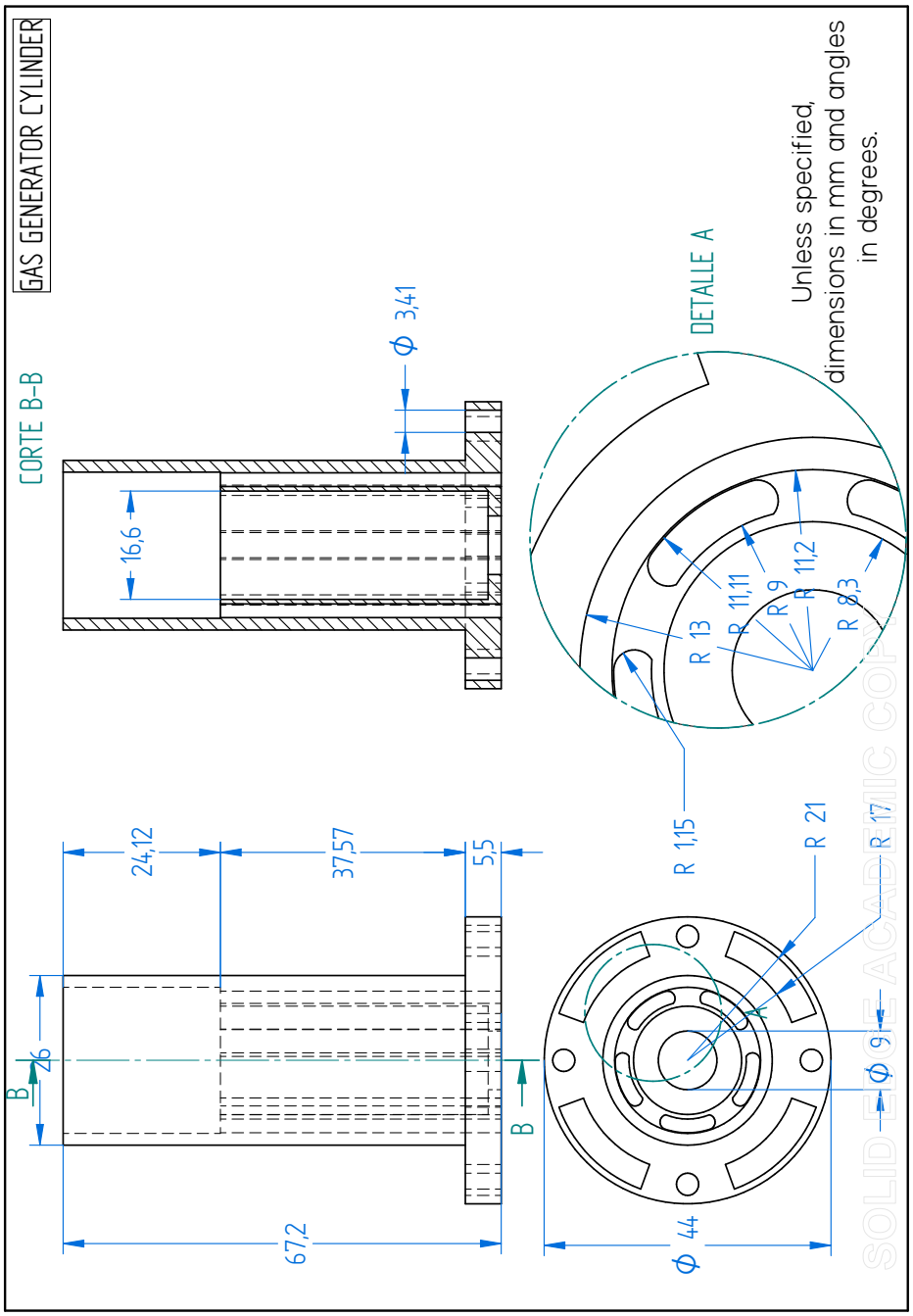

6.7 First stage nozzle drawing plan.

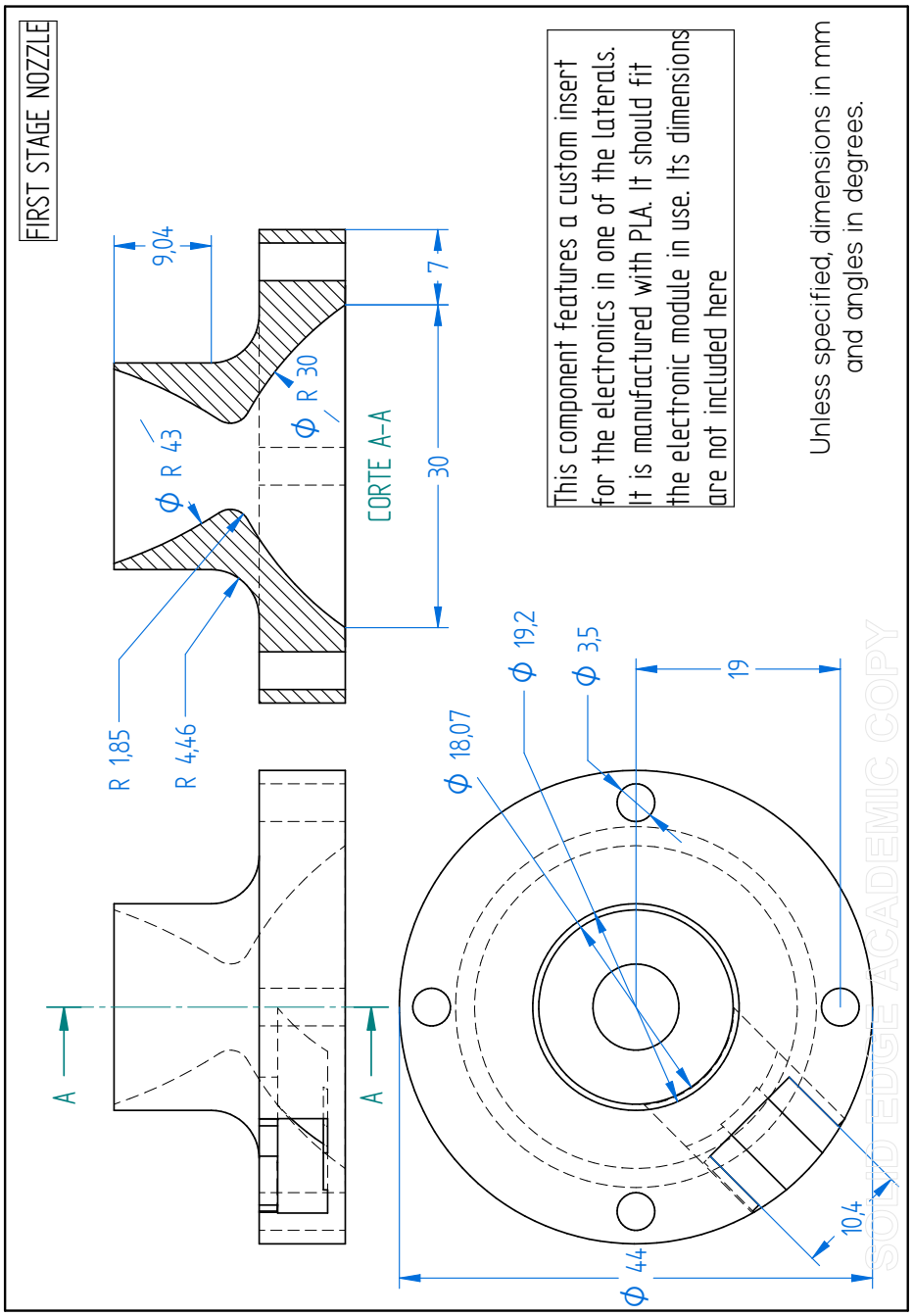

6.8 Propellant capsule drawing plan.

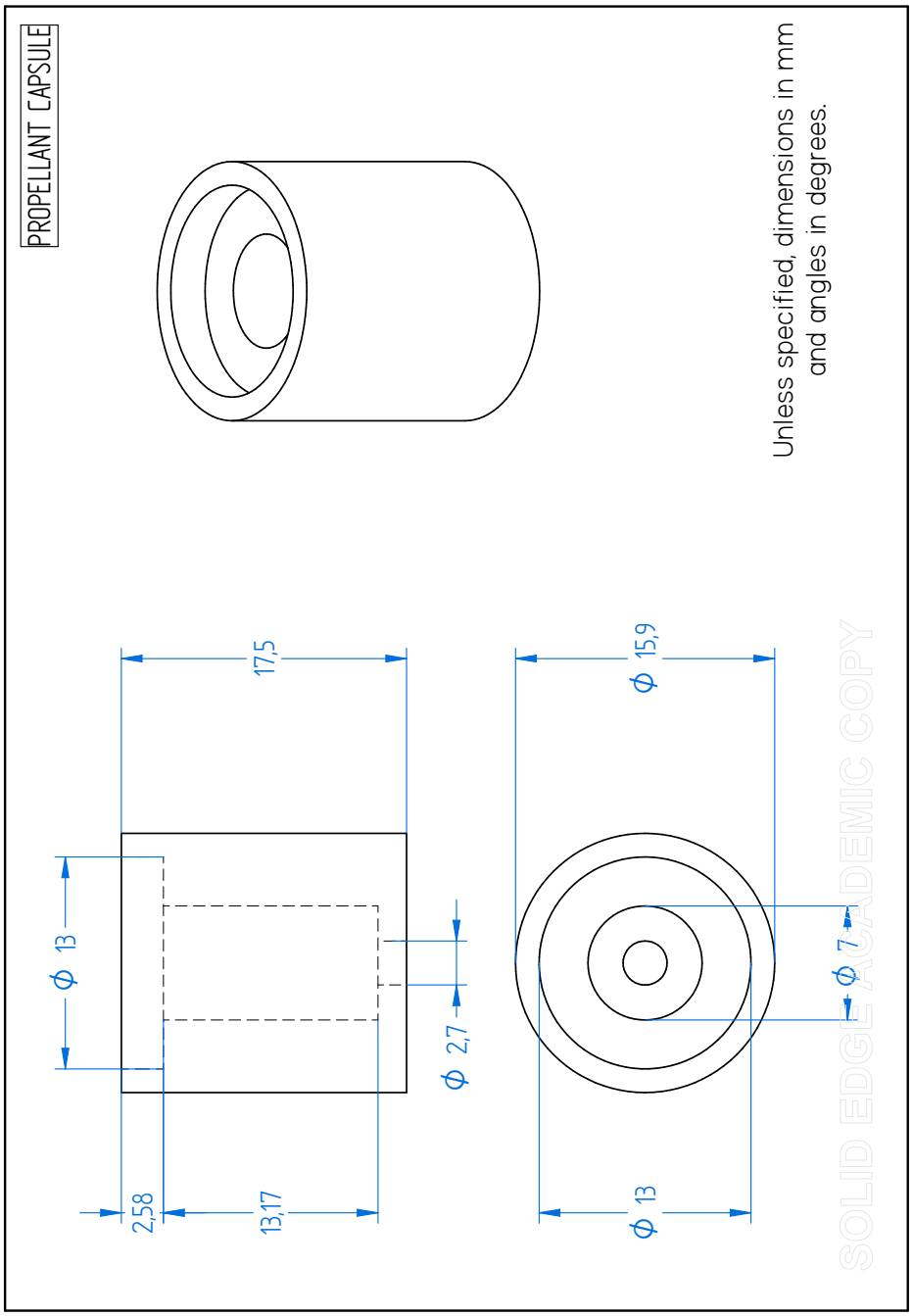

6.9 Firing pin drawing plan.

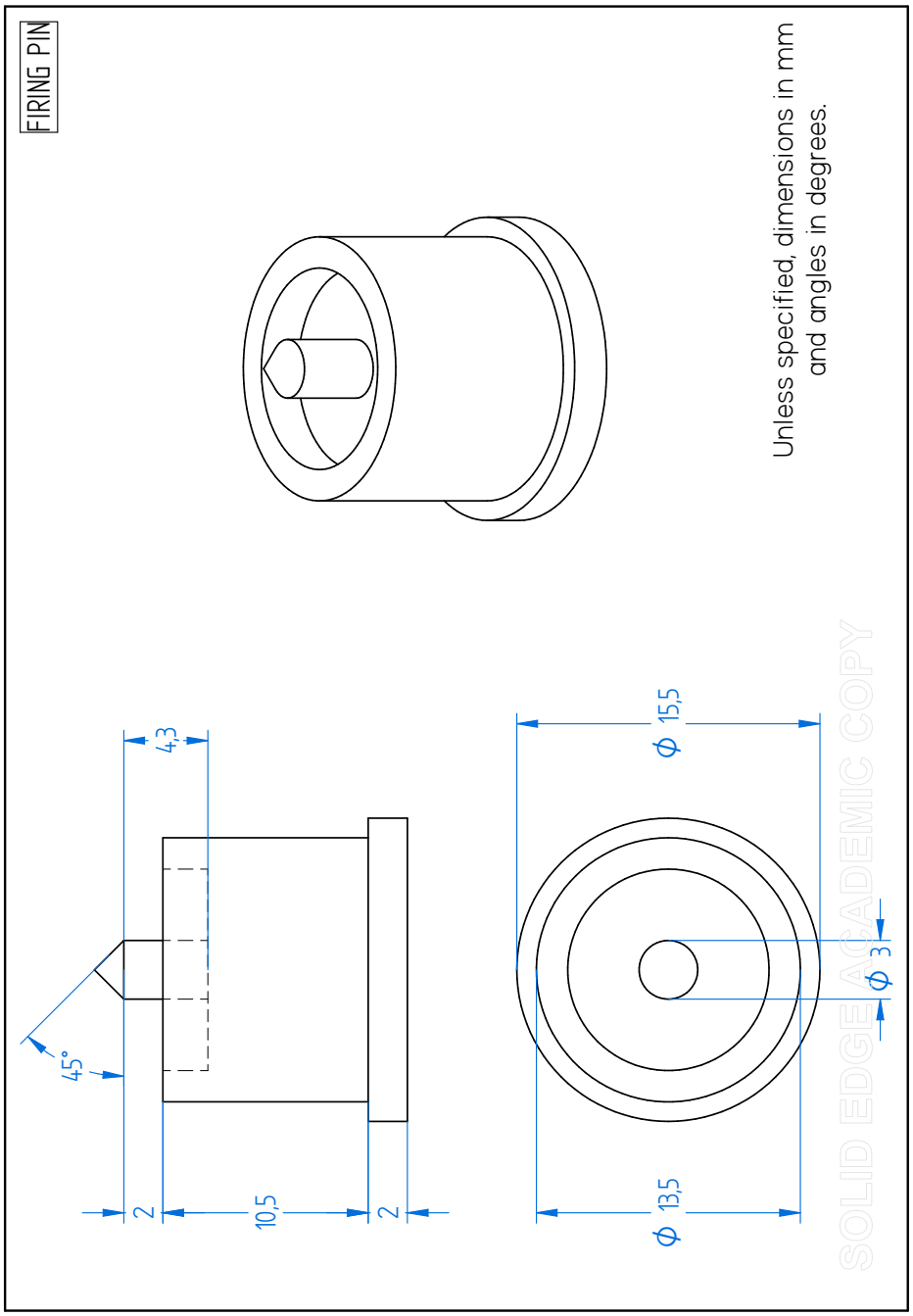

6.10 Gas cartridge adapter drawing plan.

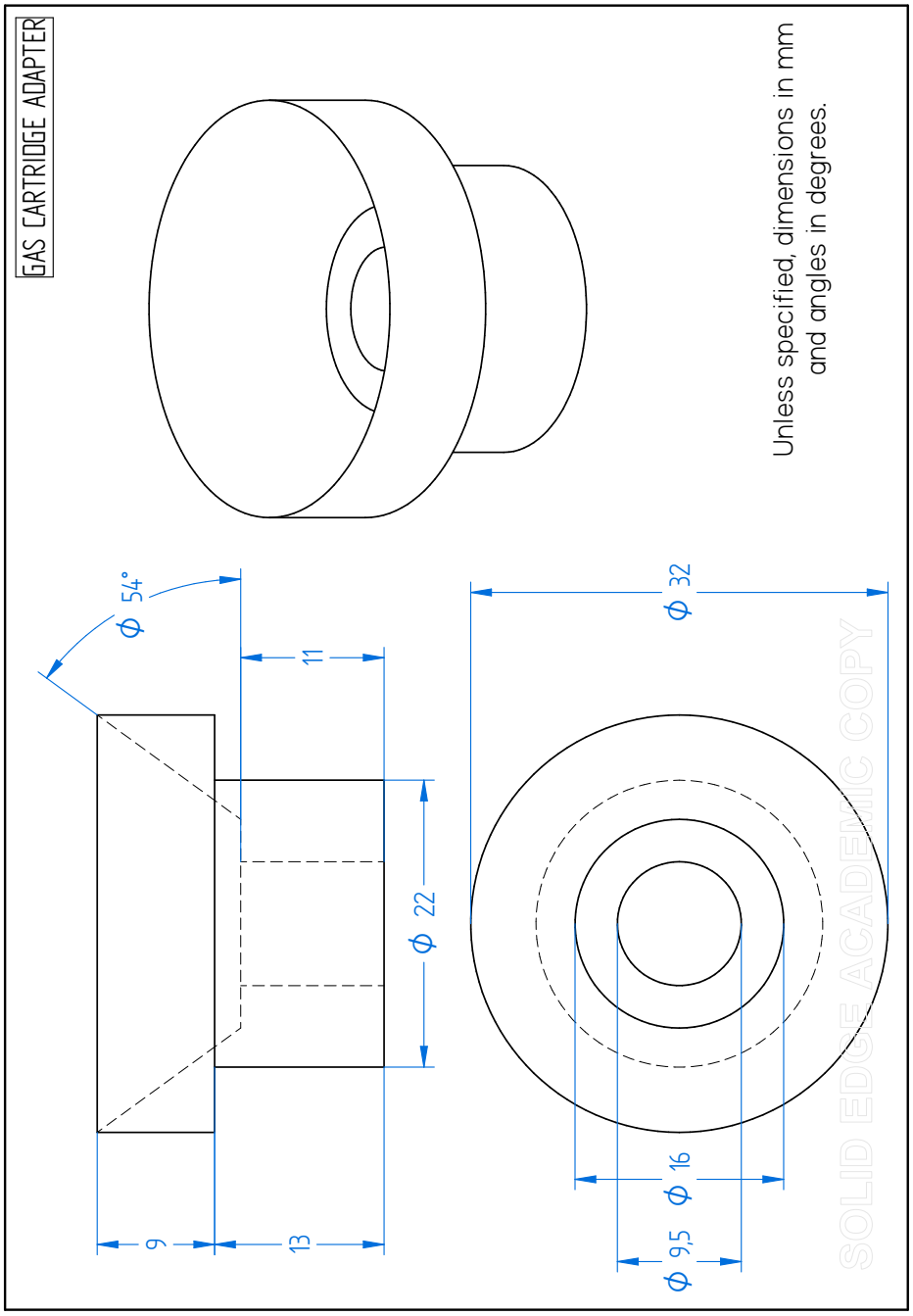

Bibliography

[1] L. Cary and J. Coyne, “ICAO Unmanned Aircraft Systems (UAS),” Tech. Rep. Circular 328, International Civil Aviation Organization, 2012.

[2] “’Eyes of the Army’ U.S army Roadmap for Unmanned Aircraft Systems,” tech. rep., U.S Army UAS Center of Excellence, Fort Rucker, Alabama, 2010.

[3] “Plan Estratégico para el desarrollo del sector civil de los Drones en España 2018-2021,” tech. rep., Ministerio de Fomento, 2020.

[4] “2009-2034 Unmanned Systems Integrated Roadmap,” tech. rep., U.S Department of Defense, 2009.

[5] J. Hu, P. Bhowmick, I. Jang, F. Arvin, and A. Lanzon, “A Decentralized Cluster Formation Containment Framework for Multirobot Systems,” *IEEE Transactions on Robotics*, vol. 37, pp. 1936–1955, December 2021.

[6] S. Hayat, E. Yanmaz, and R. Muzaffar, “Survey on Unmanned Aerial Vehicle Networks for Civil Applications: a Communications Viewpoint,” *IEEE Communications Surveys and Tutorials*, vol. 18, pp. 2624–2661, 2016.

[7] V. U. Castrillo, A. Manco, D. Pascarella, and G. Gigante, “A Review of Counter-UAS Technologies for Cooperative Defensive Teams of Drones,” *Drones*, vol. 6, no. 3, 2022.

[8] A. Tahir, J. Böling, M.-H. Haghbayan, H. T. Toivonen, and J. Plosila, “Swarms of Unmanned Aerial Vehicles — A Survey,” *Journal of Industrial Information Integration*, vol. 16, p. 100106, 2019.

[9] “Defence Against Terrorism Review,” tech. rep., Centre of Excellence Defence Against Terrorism, Turkey, 2020.

[10] T. M. Faure, “The quest of vertical flight: the development of helicopter,” December 2015.

[11] M. E. Rosheim, *Leonardo’s Lost Robots*. Springer, 2006.

[12] C. A. Kozera, “Military Use of Unmanned Aerial Vehicles – A Historical Study,” *Safety Defense*, vol. 4, no. 1, pp. 17–21, 2018.

[13] V. Prisacariu, “The History and the Evolution of UAVs from the beginning till the 70s,” *Journal of Defense Resources Management*, vol. 8, no. 14, pp. 181–189, 2017.

[14] David Daly, “A Not-So-Short History of Unmanned Aerial Vehicles (UAV).” https://consortiq.com/uas-resources/short-history-unmanned-aerial-vehicles-uavs. Accessed: 2022-10-11.

[15] “Arquimea Loitering System Q-SLAM-40.” https://www.arquimea.com/aerospace-and-defence/q-slam-40-loitering-system. Accessed: 2022-10-17.

[16] P. Valpolini, “European Defence Review. Arquimea Aerospace Defence unveils its QLM-40 loitering munition.” https://www.edrmagazine.eu/arquimea-aerospace-defence-unveils-its-qlm-40-loitering-munition. Accessed: 2022-10-17.

[17] C. G.-M. Siljeström, “Sistema integrado en un UAV para el reconocimiento técnico de ingenieros,” Master’s thesis, Centro Universitario de la Defensa - Academia General Militar, Zaragoza, 2020.

[18] “Ejército del Aire. MQ-9 Predator B.” https://ejercitodelaire.defensa.gob.es/EA/ejercitodelaire/es/aeronaves/avion/MQ-9-Predator-B/. Accessed: 2022-10-17.

[19] “Israel Aerospace Industries. Searcher Mk III Tactical UAS.” https://www.iai.co.il/p/searcher-mk-iii. Accessed: 2022-10-17.

[20] R. Nichols, J. Ryan, H. Mumm, W. Lonstein, C. Carter, and J. Hood, “Chapter 11: UAS Weapons,” in *Unmanned Aircraft Systems in the Cyber Domain*, Manhattan, Kansas: New Prairie Press, 2018.

[21] J. R. Hoehn and P. K. Kerr, “Unmanned Aircraft Systems: Current and Potential Programs, CRS Report.,” Tech. Rep. R47067, Congressional Research Service, Library of Congress, 2022.

[22] J. R. Hoehn, “Precision-Guided Munitions: Background and Issues for Congress,” Tech. Rep. R45996, Congressional Research Service, Library of Congress, 2021.

[23] Tamir Eshel, “Atk Offers Miniature Precision Guided Weapon for Unmanned Aerial Systems.” https://defense-update.com/20101029_atk_mgw.html. Accessed: 2022-01-12.

[24] Northrop Grumman, "Guided Projectiles and Precision Weapons." https://www.northropgrumman.com/what-we-do/advanced-weapons/guided-projectiles-and-precision-weapons/. Accessed: 2022-01-12.

[25] Stacey Carswell , "Munitions, Axing the Competition. Wright-Patterson AFB.." https://www.wpafb.af.mil/News/Article-Display/Article/400149/axing-the-competition/. Accessed: 2022-01-12.

[26] N. Du, W. Xiong, T. Wang, X. feng Zhang, H. hua Chen, and M. ting Tan, "Study on Energy Release Characteristics of Reactive Material Casings under Explosive Loading," *Defence Technology*, vol. 17, no. 5, pp. 1791–1803, 2021.

[27] J. Chen, Y. J. Chen, X. Li, Z. F. Liang, T. Zhou, and C. Xiao, "Metallic Reactive Materials Application in Fragmentation Warhead," *Journal of Physics: Conference Series*, vol. 1507, p. 062004, apr 2020.

[28] V. Duro de la Merced, *Study of New Technology for Nitrocellulose Propellants Stability Test*. Bachelor Thesis, Universidad Carlos III de Madrid, Escuela Politécnica Superior, 2021.

[29] V. Duro, R. López, Y. A. del Águila, R. Pardo, and L. M. Debán, "Nitrocellulose Propellants Standard Stability Tests Enhancement Employing Semiconductor Sensors," *Propellants, Explosives, Pyrotechnics*, vol. 48, no. 2, p. e202200086.

[30] P. Rivette and E. Besser, "Mil-HDBK-1211 Missile Fligt Simulation Part One, Surface-to-air missiles," Tech. Rep. 1211, U.S. Army Missile Command, Redstone Arsenal, July 1995.

[31] *Norma Militar Española NM-I-2264 EA, Instrucciones básicas para la recepción de pólvoras, explosivos, artificios ymaterial pirotécnico*. Ministerio de Defensa, 1984.

[32] *Norma Militar Española NM-P-2442 EMAG 1ªEda, Pólvoras. Condiciones técnicas de carácter general para la definición, inspección y recepción de cualquier tipo de pólvora y de las cargas confeccionadascon ellas.* Ministerio de Defensa, 1997.

[33] *Norma Militar Española NM-C-2443 EMA, Cargas propulsoras para cohetes y misiles. Condiciones técnicas de carácter general para su definición, inspección y recepción.* Ministerio de Defensa, 1987.

[34] *Norma Militar Española NME 2379 (2ªR). Pólvoras, explosivos, artificios pirotécnicos y municiones que los contienen. Vida probable*. Ministerio de Defensa, 2013.

[35] *Manual of NATO safety principles for the storage of military ammunition and explosives*. Allied ammunition storage and transport Publication, May 2010.

[36] *A Guide to Ammunition Storage, First Edition*. GICHD, first ed., November 2008.

[37] *OSCE Document on Stockpiles of Conventional Ammunition*. OSCE, November 2003.

[38] *Electro-explosive devices, assessment and test methods for characterization - AOP-43, Edition 3*. NATO Standardization Agency, March 2011.

[39] "Launching Systems," in *Fundamentals of Naval Weapons Systems* (Weapons and S. E. Deptartment, eds.), ch. 17, 121 Blake Road, Annapolis, MD 21402: United States Naval Academy.

[40] "Stinger Weapon System, Low Altitude Air Defense (LAAD) Gunner's Handbook," Tech. Rep. 287, US Marine Corps, 2011.

[41] W. Shim, I. Kim, S. Oh, J. Ha, and J. Kim, "Missile ejection system and Launching Canister Thereof," 2009. US Patent 7484.449 B2.

[42] M. A. Bohn, "Principles of ageing of double-base propellants and its assessment by several methods following propellant properties," in *NATO STO (Science Technology Organization) Applied Vehicle Technology Panel (AVT) Collaboration Support Office, AVT-268 RSM-046 (Research Specialists' Meeting) on Advances in Munition Health Management Technologies and Implementation,*, (Utrecht, The Netherlands), 2017.

[43] H. Austruy, "Double base Propellants," in *Solid Rocket Propulsion Technology* (A. Davenas, ed.), ch. 9, pp. 369–413, Amsterdam: Pergamon, 1993.

[44] D. Mishra, "Elements of Rocket Propulsion," in *Fundamentals of Rocket Propulsion*, pp. 77–79, Taylor and Francis, 2017.

[45] G. Genta, "Propulsion for Interstellar Space Exploration," in *The Outer Heliosphere: The Next Frontiers* (K. Scherer, H. Fichtner, H. J. Fahr, and E. Marsch, eds.), vol. 11 of *COSPAR Colloquia Series*, pp. 421–430, Pergamon, 2001.

[46] Y. Fabignon, J. Anthoine, D. Davidenko, R. Devillers, J. Dupays, D. Gueyffier, J. Hijlkema, N. Lupoglazoff, J.-M. Lamet, L. Tessé, A. Guy, and C. Erades, "Recent Advances in Research on Solid Rocket Propulsion," *ONERA Aerospace Lab*, January 2016.

[47] J. M. Tizón, "Burnback Analysis of Solid Propellant Rocket Motors," 2023.

[48] H. Yang, J. West, and R. Harris, "Coupled Fluid–Structure Interaction Analysis of Solid Rocket Motor with Flexible Inhibitors," *Journal of Spacecraft and Rockets*, vol. 55, pp. 1–12, 11 2017.

[49] S. P. Crusells, *Estudio de Propulsores Sólidos para Cohetes*. Academia de Artillería, Segovia, 1970.

[50] H. W. Douglass, J. H. Collins, and D. H. Barret, "Solid Rocket Motor Igniters," Tech. Rep. NASA Space Vehicle Design Criteria, NASA SP-8051, National Aeronautics and Space Administration, 1971.

[51] O. Orlandi, F. Fourmeaux, and J. Dupays, "Ignition Study at Small-Scale Solid Rocket Motor," in *EUCASS 2019*, (MADRID, Spain), July 2019.

[52] E. Cavallini, B. Favini, M. Castelli, and A. Neri, "VEGA Launch Vehicle Dynamic Loads due to Solid Propulsion Ignition Transients and Pressure Oscillations," in *52nd AIAA/SAE/ASEE Joint Propulsion Conference*, Jul 2016.

[53] G. Sutton and O. Biblarz, "Definitions and Fundamentals," in *Rocket Propulsion Elements*, ch. 2, p. 46, John Wiley & Sons, 7 ed., 2010.

[54] B. Kahraman, H. Karakas, B. N. Eren, and A. Karabeyoglu, "Erosion Rate Investigation of Various Nozzle Materials in Hybrid Rocket Motors," in *AIAA Propulsion and Energy 2020 Forum*, August 2020.

[55] L. Kamps, Y. Saito, R. Kawabata, M. Wakita, T. Totani, Y. Takahashi, and H. Nagata, "Method for Determining Nozzle-Throat-Erosion History in Hybrid Rockets," *Journal of Propulsion and Power*, vol. 33, no. 6, pp. 1369–1377, 2017.

[56] D. Bianchi and F. Nasuti, "Numerical Analysis of Nozzle Material Thermochemical Erosion in Hybrid Rocket Engines," *Journal of Propulsion and Power*, vol. 29, pp. 547–558, 05 2013.

[57] G. P. Sutton and O. Biblarz, “Solid Propellant Rocket Fundamentals,” in *Rocket Propulsion Elements, Eighth Edition*, pp. 435–492, Wiley, 2010.

[58] N. Kubota and A. Ishihara, “Analysis of the Temperature Sensitivity of Double Base Propellants,” in *Twentieth Symposium (International) on Combustion/The Combustion Institute*, pp. 2035–2041, 1984.

[59] Naminosuke Kubota, “The Mechanism of Super-Rate Burning of Catalyzed Double Base Propellants, Report AMS 1087,” tech. rep., Department of Aerospace and Mechanical Sciences, Princeton University, 1973.

[60] G. Lengellé, A. Bizot, J. Duterque, and J. F. Trubert, “Steady-State Burning of Homogeneous Propellants,” in *Fundamentals of Solid-Propellant Combustion*, ch. 7, pp. 361–407.

[61] N. Kubota, T. J. Ohlemiller, L. H. Caveny, and M. Summerfield, “Site and Mode of Action of Platonizers in Double Base Propellants,” *AIAA Journal*, vol. 12, no. 12, pp. 1709–1714, 1974.

[62] N. Kubota, “Survey of Rocket Propellants and Their Combustion Characteristics,” in *Fundamentals of Solid Propellant Combustion*, vol. 90, ch. 1, pp. 1–52, American Institute of Aeronautics and Astronautics.

[63] C. R. Rogers and N. P. Suh, “Ignition and Surface Temperatures of Double Base Propellants at Low Pressures. II - Comparison of Optical and Thermocouple Techniques,” *AIAA Journal*, vol. 8, no. 8, pp. 1501–1506, 1970.

[64] N. P. Suh, C. L. Tsai, C. L. Thompson, and J. S. Moore, “Ignition and Surface Temperatures of Double Base Propellants at Low Pressure. I - Thermocouple Measurements,” *AIAA Journal*, vol. 8, no. 7, pp. 1314–1321, 1970.

[65] M. Yanjie, B. Futing, S. Lin, L. Yang, and H. Weihua, “A New Erosive Burning Model of Solid Propellant Based on Heat Transfer Equilibrium at Propellant Surface,” *International Journal of Aerospace Engineering*, vol. 2020, 2020.

[66] B. Ropia, J. Upadhyay, R. Kalal, H. Shekhar, and D. G. Thakur, “Study of Maximum Pressure Rise with Erosive Burning in Multi-Grain Tubular Solid Propellant,” *Propellants, Explosives, Pyrotechnics*, vol. 45, no. 9, pp. 1398–1406, 2020.

[67] H. Mukunda and P. Paul, “Universal Behaviour in Erosive Burning of Solid Propellants,” *Combustion and Flame*, vol. 109, no. 1, pp. 224–236, 1997.

[68] M. K. Razdan and K. K. Kuo, “Erosive Burning of Solid Propellants,” in *Fundamentals of Solid-Propellant Propulsion*, vol. 90, ch. 10, Broadway, New York: American Institute of Aeronautics and Astronautics, 1984.

[69] J. M. Lenoir and G. Robillard, “A Mathematical Method to predict the Effects of Erosive Burning in Solid Propellant Rocket,” in *Sixth Symposium on Combustion*, pp. 663–667, 1957.

[70] S. G. M. Stekhareh, A. Mostofizadeh, N. Fouladi, and A. Soleymani, “One Dimensional Internal Ballistics Simulation of Solid Rocket Motor,” *Iranian Journal of Mechanical Engineering*, vol. 14, no. 1, pp. 5–16, 2013.

[71] R. Irisarri Muelas, *Internal Ballistics of Solid Rocket Motor*. Bachelor Thesis, Universidad Politécnica de Madrid, Escuela Técnica Superior de Ingeniería Aeronáutica y del Espacio, 2021.

[72] M. A. Willcox, M. Q. Brewster, K. C. Tang, D. S. Stewart, and I. Kuznetsov, “Solid Rocket Motor Internal Ballistics Simulation Using Three-Dimensional Grain Burnback,” *Journal of Propulsion and Power*, vol. 23, no. 3, pp. 575–584, 2007.

[73] F. S. Blomshield, J. E. Crump, H. B. Mathes, and R. A. Stalnaker, “Stability Testing of Full-Scale Tactical Motors,” *Journal of Propulsion and Power*, vol. 13, no. 3, pp. 349–355, 1997.

[74] K. Tand and M. Brewster, “Dynamic Combustion of AP Composite Propellants: Ignition Pressure Spike,” in *37th AIAA/ASME/SAE/ASEE Joint Propulsion Conference and Exhibit* (A. I. of Aeronautics and Astronautics, eds.).

[75] E. Cavallini, *Modelling and Numerical Simulation of Solid Rocket Motors Internal Ballistics*. PhD thesis, Sapienza Università de Rima, 2009.

[76] D. R. Greatrix, “Scale Effects on Quasi-Steady Solid Rocket Internal Ballistic Behaviour,” *Energies*, vol. 3, no. 11, pp. 1790–1804, 2010.

[77] K. Tang and M. Brewster, “Dynamic Combustion of AP Composite Propellants - Ignition Pressure Spike,” in *37th Joint Propulsion Conference and Exhibit*.

[78] K. C. Tang and M. Q. Brewster, “Nonlinear Dynamic Combustion in Solid Rockets: L* Effects,” *Journal of Propulsion and Power*, vol. 17, no. 4, pp. 909–918, 2001.

[79] M. D. Giacinto, “Numerical Simulation of Solid Motor Ignition Transient,” *International Journal of Energetic Materials and Chemical Propulsion*, vol. 5, no. 1-6, pp. 673–688, 2002.

[80] S. Krishnan and R. Ramakrishnan, “Effect of motor length and propellant formulation on nozzleless solid rocket performance,” *Proceedings of the Institution of Mechanical Engineers, Part G: Journal of Aerospace Engineering*, vol. 213, no. 1, pp. 35–44, 1999.

[81] G. Lengellé, J. Duterque, and J. Trubert, “Combustion of solid propellants,” in *RTO-EN-023, Special Course on Internal Aerodynamics in Solid Rocket Propulsion*, (Rhode-Saint-Genèse, Belgium,), 2002.

[82] M. Goeing, “Nozzle design Optimization by Method-of-Characteristics,” in *26th Joint Propulsion Conference*, 1990.

[83] M. Murnaghan, “Study of minimum length, supersonic nozzle design using the method of characteristics,” Master’s thesis, Universidad Politécnica de Cataluña, Terrassa, 2019.

[84] M. A. Khan, S. K. Sardiwal, M. S. Sharath, and D. H. Chowdary, “Design of a Supersonic Nozzle using Method of Characteristics,” *International Journal of Engineering Research and Technology*, vol. 2, no. 11, pp. 19–24, 2013.

[85] G. J. Bryan, J. Enig, and E. E. Kilmer, “Ignition of Propellants by Hot Gases Part III. Ignition Energy Requirements and Heat Transfer under transient conditions,” Tech. Rep. NAVORD Report 3818, US Naval Ordnance Laboratory, 1955.

[86] P. Titi, T. Tiganescu, O. Iorga, R. Ginghina, and O. Grigoroiu, “Experimental and Theoretical Study on Three Combustion Models for the Determination of the Performance Parameters of Nitrocellulose - Based Propellants,” *Revista de Chimie*, vol. 71, pp. 87–97, 10 2020.

[87] J. P. Agrawal, “Propellants,” in *High Energy Materials. Propellants, Explosives and Pyrotechnics*, ch. 4, pp. 209–316.

[88] J. R. Ward and R. W. Geene, “Erosivity of Nitramine Propellant with a Flame Temperature comparable to M30 Propellant,” Tech. Rep. Memorandum Report ARBRL-MR-02926, US Army Armament Research and Development Command, Ballistic Research Laboratory, 1979.

[89] L. R. Warren, Z. Wang, C. R. Pulham, and C. A. Morrison, “A Review of the Catalytic Effects of Lead-Based Ballistic Modifiers on the Combustion Chemistry of Double Base Propellants,” *Propellants, Explosives, Pyrotechnics*, vol. 46, no. 1, pp. 13–25, 2021.

[90] Tyler Rogoway, “Here Is How Much Those Decoy Flares Cost That Military Aircraft Fire off All The Time.” https://www.thedrive.com/the-war-zone/31556/here-is-how-much-those-decoy-flares-cost-that-military-aircraft-fire-off-all-the-time. Accessed: 2023-05-06.